IMPERIAL COLLEGE LONDON

Integrated Ultrasonic Imaging for Inspection of Near-Surface Defects in Safety-Critical Components

by

Chao Zhang

A thesis submitted to Imperial College London for the degree of

Doctor of Philosophy

Department of Mechanical Engineering

Imperial College London

London SW7 2AZ

June 2018

Declaration of Originality

The content of thesis is my own work, produced under the supervision of Dr. Peter Huthwaite and Professor Michael Lowe. Where I have built on the work of others, I have fully acknowledged this, providing appropriate references.



5th September 2018

Copyright

The copyright of this thesis rests with the author and is made available under a Creative Commons Attribution Non-Commercial No Derivatives licence. Researchers are free to copy, distribute or transmit the thesis on the condition that they attribute it, that they do not use it for commercial purposes and that they do not alter, transform or build upon it. For any reuse or redistribution, researchers must make clear to others the licence terms of this work.

Abstract

A common location for defects to appear is at the surface of a component. While at the near surface, many non-destructive evaluation (NDE) techniques are available to inspect for these, at the far surface this is much more challenging. Ultrasonic array imaging is proposed to enable far surface defect detection, location and characterisation. In this thesis, array imaging is explored for the practical application of subsurface imaging and characterisation of the near backwall defects, especially surface-breaking cracks. In this application, the component has two parallel surfaces, the crack is initiated from the far side and the phased array is attached on the near side.

One specific challenge here is the presence of a strong reflection from the backwall, which can often mask the relatively small response from a defect. Ideally, a pure scattered field from a defect is needed for the correct estimation of the scatterer through the imaging algorithm, thus, the presence of the backwall will result in strong effects in the resulting image. Several post-processing methods, which have to be used together with specific imaging algorithms, are developed in this thesis to eliminate the strong effects introduced by the presence of the backwall. The effectiveness of these proposed methods are validated in both simulations and experiments.

In this thesis, the Factorization Method (FM) is explored for the application of subsurface imaging and characterisation of the surface-breaking cracks. The performance of the FM algorithm and relevant backwall effects eliminating methods were tested with the simulated and experimental data. The experimental results showed a good consistency with the simulated results. It is shown that the FM algorithm can generate high quality images to provide a good detection of the crack and an accurate sizing of the crack length.

The quality of the array imaging highly depends on the imaging algorithm used. One way

to make array imaging more applicable is to extend the library of the imaging algorithms. Based on this aim we study the application of two innovative imaging algorithms, i.e. the Direst Sampling Method and the Fast Topological Imaging, in ultrasonic array imaging. Firstly, these imaging algorithms are tested with numerical simulations to image different type of defect. After that, several experiments are performed to assess their performance in practice.

The development of the backwall effect eliminating methods is based on the assumption that the backwall is perfectly smooth. However, for real components experiencing harsh environments, the surfaces are rarely perfectly smooth. Therefore, the developed backwall eliminating methods are also validated on components with a rough backwall to check the tolerance to the roughness.

Acknowledgements

First of all, I must thank my supervisors Dr. Peter Huthwaite and Professor Mike Lowe for their continued encouragement and infinite patience. Without their professional guidance and supervision, all the work in this thesis would have been impossible. It's my great honour to be their student.

Furthermore, I would like to extend my thanks to all the members of the NDE lab for creating a enjoyable and productive work environment. Especially to Jack and Fan for guiding me with the experimental array system and discussions about array imaging, and to the cruncher team for working with me to keep the high performance computers work well.

I would also like to thank the RCNDE and EPSRC for funding this project. I am very grateful to the suggestions and experimental samples from Amec Foster Wheeler UK and the NDE Research team at Rolls-Royce Submarines.

I would like express my gratitude to my family for their encouragement and support. Most importantly, I want to give my deep appreciation and love to my dear wife Xue Zheng (Michelle) who has been doing her utmost to support me in the past three years.

Contents

1 Introduction **20**

1.1 Motivations 20

1.2 Outline of Thesis 29

2 Background theory **32**

2.1 Introduction 32

2.2 Governing Equation 33

2.3 Forward scattering 35

2.4 Spaces and operators 39

2.5 Inverse scattering 42

2.6 Beamforming imaging methods 43

2.6.1 Born approximation 43

2.6.2 Total Focusing Method 46

2.6.3 Half-Skip Total Focusing Method 48

2.7 Super resolution methods 50

2.7.1 Multiple scattering 51

2.7.2 Linear Sampling Method 53

2.7.3 Factorization Method 55

3 Eliminating backwall effects for near backwall defect imaging **58**

3.1 Introduction 58

3.2 Imaging setup 60

3.3 Eliminating backwall effects 61
3.3.1 Signal overlap problem 61
3.3.2 Backwall subtraction method 63
3.3.3 Weighting function method for HSTFM 68
3.3.4 Truncation method for FM 71
3.4 Experimental validation 76
3.5 Conclusions 79

4 Accurate depth measurement of surface-breaking notches using the Factorization Method 82
4.1 Introduction 82
4.2 FE model description 84
4.3 FM vs TFM 85
4.3.1 The effect of the FMC subtraction 90
4.3.2 The effect of the truncation method 97
4.4 Experiment results 99
4.5 Conclusions 103

5 Novel imaging algorithms for imaging near backwall defects using FMC data 105
5.1 Introduction 105
5.2 Background theory of the imaging algorithms 106
5.2.1 Direct Sampling Method 106
5.2.2 Time Domain Sampling Method 108
5.2.3 Fast topological imaging 109
5.3 Numerical simulation 113
5.3.1 Reconstruction of point scatterers 114
5.3.2 Reconstruction of crack-like scatterers 119
5.3.3 Noise robustness 121

5.4 Application in NDE for imaging near backwall defects 124
5.4.1 Near backwall side-drilled holes 124
5.4.2 Surface-breaking notch 127
5.5 Conclusions 130

6 Array imaging of defects near a rough backwall 131
6.1 Introduction 131
6.2 Numerical generation of rough surfaces 132
6.3 Numerical results and discussions 136
6.3.1 Imaging results 136
6.3.2 Sizing results 144
6.4 Conclusions 145

7 Conclusions 147
7.1 Thesis review 147
7.2 Main achievements 149
7.3 Potential future work 153

References 156

List of Publications 170

List of Figures

1.1 Schematic of the principle of ultrasonic testing. 21

1.2 Diagrams of the concepts showing (a) B-scan and (b) C-scan. 21

1.3 Diagrams show the delay laws of (a) a plane beam and (b) a focused beam. 23

1.4 Common array definitions: (a) 1-D linear array, (b) 2-D array, (c) annular array. 23

1.5 Transmitting and receiving procedure of the Full Matrix Capture. 25

1.6 (a) A TFM image of two poorly resolved point scatterers, which are separated by 0.4λ; (b) A TFM image of three side-drilled holes in a 304L steel block; (c) TFM images of surface-breaking notches with different tilt angles. Note that the red dotted lines in the images were used to indicate the location of backwalls. 28

2.1 Schematic of the 2D scattering problem. The bounded Dirichlet obstacle D is illuminated from the incident field excited on surface Γ_i and the produced scattered field is measured on the surface Γ_m. Ω is the sampling domain where the obstacle D lies. 36

2.2 Schematic of the far-field scattering problem. (a) The object is illuminated from the far-field; (b) The scattered field is measured in the far-field. . . . 39

2.3 Schematic of the far-field scattering problem. (a) The object is illuminated from the far-field; (b) The scattered field is measured in the far-field. . . . 41

2.4 The operator, M, maps the object function to scattering amplitude. Note that $\mathcal{O}(\boldsymbol{R}) :== \mathcal{F}[O](\boldsymbol{r})$, where $\mathcal{F}$ means the Fourier transform and R is the spatial frequency. 42

2.5 The Ewald limiting circle of radius $2k$. The spatial frequencies of the scatterer outside the Ewald limiting circle cannot be measured under Born approximation. 45

2.6 Schematic of the working process of the Total Focusing Method. 46

2.7 Schematic of the configuration of the Total Focusing Method. 48

2.8 (a) Example of the direct ray path considered in TFM, (b) Example of the 'half-skip' ray path considered in HSTFM, (c) Equivalent ray path of the ray path considered in (b). 49

2.9 Simple case of two scatterers to show the scattered fields with or without multiple scattering. (a) Path of scattering field under Born approximation; there is no interactions between the scattered fields and the targets, (b) Path of scattering field considering multiple scattering; there are interactions between the scattered fields and the targets. 51

2.10 The LSM and the FM are based on the fact that the scattered field can only be generated at the boundary of the scatterer but cannot have originated at any point outside the scatterer. 54

3.1 (a) Schematic showing the inspection of a component containing a surface-breaking crack. (b) Schematic showing the difference in angle of view between two different imaging setups. (c) Schematic showing the ray paths of different signal components when the defect is located directly beneath the array; note that the red ray path represents the backwall reflection, the blue ray path represents the 'half-skip' reflection and the green ray path represents the tip diffraction. 60

3.2 Snapshot of the FE model used for simulation in Abaqus (Dassault Systemes Simulia Corp., Providence, RI). The length of the notch is 2λ, the thickness of the component is 20λ and the distance between two transceivers of the array is 0.5λ. Frequency is 2MHz, giving a wavelength (λ) of 3mm. 62

3.3 The time traces of three different elements based on simulated FMC data; note that the element 1 is used as the transmitter while all the elements used as receivers. 63

3.4 Results from setup shown in Fig. 3.2. (a) HSTFM and (b) FM images based on the overall signal. The red 'X' symbols at the top of the images represent the location of the transceivers and the amplitude is normalized to the maximum value in each image. The results here are from simulated data. 64

3.5 (a) Schematic showing the components of a received signal; (b) The time traces of different transmitter-receiver pairs with same $|i - j|$ based on simulated array data for the configuration in Fig. 3.1 when h=60mm, d=6mm and $\theta_{test} = 0°$. 66

3.6 Results from setup shown in Fig. 3.2. (a) HSTFM and (b) FM images, all based on the original signal. (c) HSTFM and (d) FM images, all based on the signal after FMC subtraction. The images are normalized to the maximum value in each image. Note that the red dotted lines in the images are used to represent the location of backwall. The results here are from simulated data. 67

3.7 (a) Equivalent ray path of the backwall reflection considered in the HSTFM, (b) Equivalent ray path of the 'half-skip' reflection considered in the HSTFM. 70

3.8 Results from setup shown in Fig. 3.2. (a) Conventional HSTFM image based on the overall signal, (b) Conventional HSTFM with the weighting function image based on the overall signal. The images were normalized to the maximum value in each image. The results here were from simulated data. 71

3.9 Singular values spectrum for the simulated FMC data at 2MHz. 72

3.10 Results from setup shown in Fig. 3.2. (a) FM image using the 80% criterion, (b) FM image using the 10% criterion, (c) FM image using the 1% criterion. The images were normalized to the maximum value in each image. The results here are from simulated data. 72

3.11 Two related models: (a) The configuration of imaging the near surface notch using an array placed on the remote surface, (b) The related two array configuration with the notch located in the middle of the material. The depth of the notch in (b) is twice the depth of the notch in (a). . . . 74

3.12 Results from setup shown in Fig. 3.2. (a) FM image using the the truncation method to eliminate the backwall effects, (b) FM image using the the truncation method to eliminate the backwall effects and the mirror enhancement to improve the image quality. The images were normalized to the maximum value in each image. The results here were from simulated data. 76

3.13 (a) The picture of the sample and the crack opening. (b) Schematic showing the experimental setup. 77

3.14 (a) HSTFM and (b) FM images based on the FMC data after FMC subtraction, (c) HSTFM with the weighting function image based on the original FMC data, (d) FM with the truncation method and the mirror enhancement image based on the original FMC data. The images are normalized to the maximum value in each image. The results here are from experimental data. 78

4.1 Schematic of the FE model (not to scale). 86

4.2 (a) TFM image of a 4λ deep notch. (b) FM image of a 4λ deep notch. (c) Notch sizing method for the TFM image. (d) Notch sizing method for the FM image. Note that the red lines in the images were used to indicate the location and length of the notch in models and the amplitude is on dB scale, normalized to the maximum value in each image. The results here were from simulated data. 87

4.3 Schematic of the wave undergoing the half-skip reflection, which causes mirror effect in the FM images. 88

4.4 The imaging results of the TFM and the FM with various noise levels and notch depths. The TFM results only contain two noise levels as TFM is not sensitive to the noise. Note the images were normalized to the maximum value in each image. The results here were from simulated data. 91

4.5 The sizing results of the TFM and the FM with different notch depths and noise levels: (a) The sizing results when SNR=50dB; (b) The sizing results when SNR=5dB. The -6dB and -12dB correspond to the amplitudes relative to the peak at which the end of the notch is considered to end, providing a sizing estimate. 92

4.6 Plots of the pure backwall reflections used in the baseline subtraction (blue) and the FMC subtraction (red). Note that array element 1 is used as the transmitter while all the elements used as receivers. 93

4.7 The TFM images of a 2λ notch when $SNR = 5dB$: (a) Without removing the backwall reflection; (b) The backwall reflection was removed by baseline subtraction; (c) The backwall reflection was removed by FMC subtraction. Note that the images were normalized to the maximum value in each image. The results here were from simulated data. 94

4.8 The FM images of a 2λ notch: (a) Without removing the backwall reflection at $SNR = 50dB$; (b) Without removing the backwall reflection at $SNR = 5dB$; (c) The backwall reflection was removed by baseline subtraction at $SNR = 50dB$; (d) The backwall reflection was removed by baseline subtraction at $SNR = 5dB$; (e) The backwall reflection was removed by FMC subtraction at $SNR = 50dB$; (f) The backwall reflection was removed by FMC subtraction at $SNR = 5dB$. Note that the images were normalized to the maximum value in each image. The results here were from simulated data. 96

4.9 The sizing results of the FM images and the TFM images using different methods to remove the backwall reflection: (a) The sizing results when SNR=50dB; (b) The sizing results when SNR=5dB. 97

4.10 The imaging results of the FM with various noise levels and notch depths based on the original FMC data. The truncation method (80% threshold) together with the mirror enhancement were used to eliminate the backwall effects. Note the images were normalized to the maximum value in each image. The results here are from simulated data. 98

4.11 The sizing results of the FM images when the truncation method is used to eliminate the backwall effects: (a) The sizing results when SNR=50dB; (b) The sizing results when SNR=5dB. 99

4.12 The imaging results of the TFM and the FM based on the experiment data acquired by two different array probes: (a) FM image with a 1MHz centre frequency; (b) FM image with a 5MHz centre frequency; (c) TFM image with a 1MHz centre frequency; (d) TFM image with a 5MHz centre frequency. Note that the EDM notch is labelled in the images. The FMC subtraction was used to remove backwall reflections The results here were from experimental data. 101

4.13 The imaging results of the FM based on the experimental data acquired by two different array probes: (a) FM image with a 1MHz centre frequency; (b) FM image with a 5MHz centre frequency. Note that the EDM notch is labelled in the images. The truncation method together with the mirror enhancement were used to eliminate the backwall effects. 102

5.1 Decay patterns of $C\Im(G(\boldsymbol{r_p}, k; \boldsymbol{r_j}))$ as $r = |\boldsymbol{r_p} - \boldsymbol{r_j}|$ when $k = 2\pi$. 108

5.2 The imaging schema of the Fast Topological Imaging. Note that the signals are plotted in the time domain for clarity. 111

5.3 (a) Schematic of the FE model containing two well-resolved point scatterers (not to scale). (b) DSM image of two well-resolved point scatterers at the central frequency 2MHz, (c) MDSM image of two well-resolved point scatterers using 10 uniformly distributed frequencies between 1.5MHz and 2.5MHz, (d) TDSM image of two well-resolved point scatterers using time domain data, (e) FTIM image of two well-resolved point scatterers using a 35kHz frequency step between 1.5MHz and 2.5MHz. Note that the red circles in the images are used to represent the true location and shape of point scatterers. The imaging results here are from simulated data. 116

5.4 (a) Schematic of the FE model containing two poorly-resolved point scatterers (not to scale). (b) DSM image of two poorly-resolved point scatterers at the central frequency 2MHz, (c) MDSM image of two poorly-resolved point scatterers using 10 uniformly distributed frequencies between 1.5MHz and 2.5MHz, (d) TDSM image of two poorly-resolved point scatterers using time domain data, (e) FTIM image of two poorly-resolved point scatterers using a 35kHz frequency step between 1.5MHz and 2.5MHz. Note that the red circles in the images are used to represent the true location and shape of point scatterers. The imaging results here are from simulated data. . . . 118

5.5 (a) Schematic of the FE model containing an embedded notch with zero tilt angle (not to scale). (b) DSM image of a notch with zero tilt angle, (c) MDSM image of a notch with zero tilt angle using 10 uniformly distributed frequencies between 1.5MHz and 2.5MHz, (d) TDSM image of a notch with zero tilt angle using time domain data, (e) FTIM image of a notch with zero tilt angle using a 35kHz frequency step between 1.5MHz and 2.5MHz. Note that the red line in the images is used to represent the true location and shape of the notch. The imaging results here are from simulated data. 120

5.6 All plots as in Fig. 5.5, except for a tilt angle of 15°. 122

5.7 All plots as in Fig. 5.5, except for a tilt angle of 20°. 123

5.8 DSM images of an embedded notch under different noise levels: (a) $SNR = 20dB$; (b) $SNR = 5dB$. MDSM images of an embedded notch under different noise levels: (c) $SNR = 20dB$; (d) $SNR = 5dB$. TDSM images of an embedded notch under different noise levels: (e) $SNR = 20dB$; (f) $SNR = 5dB$. FTIM images of an embedded notch under different noise levels: (g) $SNR = 20dB$; (h) $SNR = 5dB$. Note that the red line in the images is used to represent the true location and shape of the notch. The imaging results here are from simulated data. 125

5.9 Picture of the experiment sample that contains three side-drilled holes. . . 126

5.10 The (a) DSM, (b) MDSM, (c) TDSM and (d) FTIM imaging results based on the experimental data. The DSM was calculated at 2.5MHz, the MDSM was calculated using 10 uniformly distributed frequencies between 2.0MHz and 3.0MHz, the TDSM was calculated using the time domain data and the FTIM was calculated using a 70kHz frequency step between 2.0MHz and 3.0MHz. Note that the side-drilled holes are labelled in the images and the images were normalized to the maximum value in each image. . . 127

5.11 Picture of the experiment sample that contains a surface-breaking notch. . 128

5.12 The (a) DSM, (b) MDSM, (c) TDSM and (d) FTIM imaging results based on the experimental data. The DSM was calculated at 2.5MHz, the MDSM was calculated using 10 uniformly distributed frequencies between 2.0MHz and 3.0MHz, the TDSM was calculated using the time domain data and the FTIM was calculated using a 70kHz frequency step between 2.0MHz and 3.0MHz. Note that the EDM notch is labelled in the images the images were normalized to the maximum value in each image. 129

6.1 RMS intensities of scattering amplitude distribution averaged over 20 realizations for an incident angle of 30° from surfaces with different roughness: (a) a smooth surface, (b) a slightly rough surface and (c) a very rough surface. 132

6.2 Sketch of the scattering on an infinitely long rough surface with stress free boundary condition 133

6.3 Realizations of 2D isotropic Gaussian rough surface profiles: (a) $\delta = 1mm$ and $\lambda_x = 9mm$; (b) $\delta = 1mm$ and $\lambda_x = 18mm$; (c) $\delta = 0.5mm$ and $\lambda_x = 9mm$. 135

6.4 Sketch of FE model which contains a Gaussian rough backwall (not to scale).136

6.5 (a) The plot of the height data of the Gaussian rough backwall ($\delta = \lambda_0/12$ and $\lambda_x = 12\lambda_0$) used in the FE model that provided FMC data. (b) HSTFM and (c) FM images based on the FMC data after FMC subtraction; (d) HSTFM with the weighting function image based on the original FMC data; (e) FM with the truncation method and the mirror enhancement image based on the original FMC data; (f) HSTFM with the weighting function image based on the FMC data after FMC subtraction. 137

6.6 As Fig. 6.5, except with a perfectly smooth backwall. 137

6.7 As Fig. 6.5, except with roughness parameters of $\delta = \lambda_0/12$ and $\lambda_x = 6\lambda_0$. 139

6.8 As Fig. 6.5, except with roughness parameters of $\delta = \lambda_0/12$ and $\lambda_x = 3\lambda_0$. 140

6.9 As Fig. 6.5, except with roughness parameters of $\delta = \lambda_0/6$ and $\lambda_x = 12\lambda_0$. 140

6.10 As Fig. 6.5, except with roughness parameters of $\delta = \lambda_0/6$ and $\lambda_x = 6\lambda_0$. . 141

6.11 As Fig. 6.5, except with roughness parameters of $\delta = \lambda_0/6$ and $\lambda_x = 3\lambda_0$. . 141

6.12 As Fig. 6.5, except with roughness parameters of $\delta = \lambda_0/3$ and $\lambda_x = 12\lambda_0$. 142

6.13 As Fig. 6.5, except with roughness parameters of $\delta = \lambda_0/3$ and $\lambda_x = 6\lambda_0$. . 142

6.14 As Fig. 6.5, except with roughness parameters of $\delta = \lambda_0/3$ and $\lambda_x = 3\lambda_0$. . 143

7.1 Schemes of the different wave propagation modes: a) direct, b) half-skip, c) full-skip 154

List of Tables

3.1 Specification of the array transducer used in experimental measurements. . 76

4.1 Array parameters 100

4.2 FM and TFM sizing results based on the FMC subtraction - the true notch size is 11mm 101

4.3 FM sizing results based on the truncation method - the true notch size is 11mm 103

5.1 Specifications of the ultrasonic array used in experiments. 126

6.1 Sizing results of a 6mm surface-breaking notch originated from a rough backwall 145

Chapter 1

Introduction

1.1 Motivations

Non-Destructive Evaluation (NDE) has been used for decades in industry. The purpose of NDE is to evaluate the properties and characteristics of material without causing any change or damage to the material. NDE can also be used to inspect a component with any configuration to detect internal discontinuities, such as cracks. The properties could include dimension, size, interior structure and grain size [1]. As a technique, NDE has experienced significant innovations and received developments in the last 30 years, which results in a wide range of types of methods and implementations of this technique.

NDE methods can vary depending on the type of emitter and penetrating medium, and among all the NDE methods, the most frequently performed methods are electromagnetic testing, ultrasonic testing, visual testing, guided wave testing, radiographic testing and magnetic particle testing [1]. As one of the most commonly used NDE methods, ultrasonic testing utilizes high frequency sound waves to interrogate the component to enable information such as measurements of dimensions or properties, or the detection of defects to be performed [2].

In general, typical ultrasonic testing equipment should include an emitter or transducer, a receiver and other relating functional parts, such as a display board. As shown in Fig. 1.1, the transducer is attached to the component being inspected in order to emit high frequency sound energy into the component. Then, the sound energy propagates through

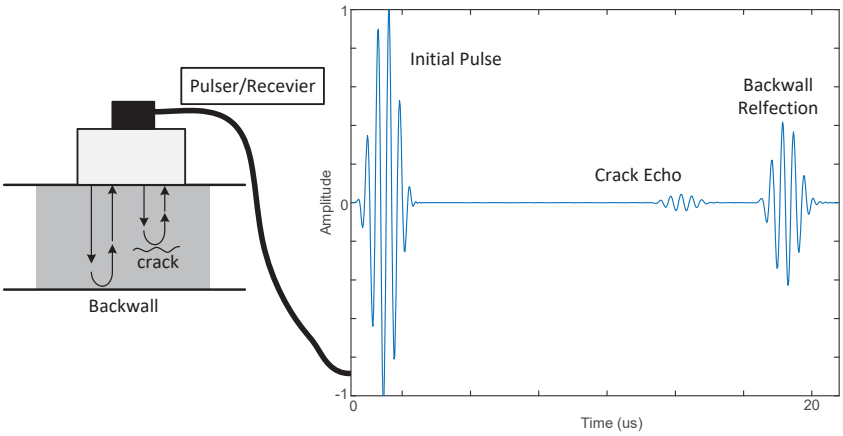


Figure 1.1: Schematic of the principle of ultrasonic testing.

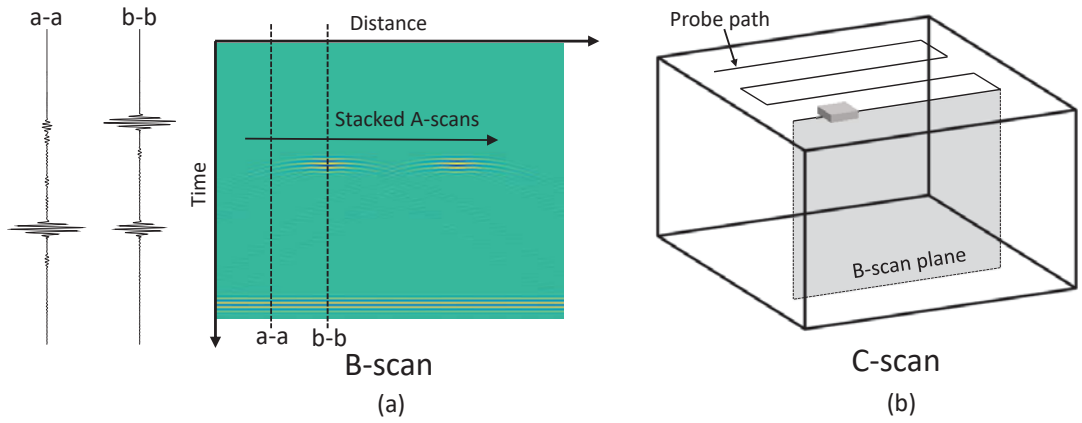


Figure 1.2: Diagrams of the concepts showing (a) B-scan and (b) C-scan.

the component. Because of the presence of a discontinuity, waves are reflected back and captured by the receiver [3]. Through this method, information about the features of the discontinuity is encoded into a record of values, typically voltage corresponding to the compression of a piezoelectric crystal and can be displayed as a time domain oscillogram (A-scan).

As shown in Fig. 1.2(a), by combining the A-scans produced at successive locations using a single transducer, it is possible to build an ultrasonic image, which is referred to as a B-scan [4]. The advantage of B-scan presentation is that the B-scan provides a cross-sectional view of the component under inspection, which allows the estimation of the approximate size and depth of the reflector. As the B-scan is produced based on A-scans, one limitation of this display technique is that some reflectors may be masked by larger reflectors located above them. The approach of producing a B-scan can also be extended

to C-scan [5] where the probe is swept in a line-by-line manner (Fig. 1.2(b)), known as raster scanning [6]. This is typically presented as a 2D image by taking a single parameter, e.g. travel time or peak amplitude, from each signal. As the ultrasonic wave is often able to penetrate deeply into the material, ultrasonic testing (UT) has advantages of large penetration depth and high sensitivity in the detection of flaws compared to most other NDE methods [3]. By analysing the arrival time and the attenuation of the transmitted and reflected signals, it is possible to determine the positions of the discontinuities in the material. With the help of imaging techniques, the UT can reconstruct detailed images to estimate the shape, size and even mechanical properties of the discontinuity. Ultrasonic imaging is therefore very valuable to aid the evaluation of damage such as cracks and corrosion. Due to its low cost and great testing coverage, UT is now frequently performed in industry.

The ultrasonic phased array technique is an advanced ultrasonic testing technique which has been developed rapidly in recent years. Unlike conventional ultrasonic testing equipment, the transducer of a phased array consists of many individual elements which can work separately and simultaneously. Because of this feature, the phased array has flexibility to steer sound beams to focus energy at a point, improving sensitivity. This is achieved by introducing a time delay when firing each element [7]; Fig. 1.3 illustrates the delay laws of a plane beam and a focused beam using a phased array, respectively.

Currently, the most common geometry of ultrasonic array is 1-D linear array, and there are also several popular geometries, such as 2-D array and annular array, which are shown in Fig. 1.4. The different geometries determine the area of locations which would be focused on, for example, the 1-D linear array allows the focusing and imaging in a plane [8]. The 1-D linear array is the most commonly used for non-destructive evaluation (NDE) and is also very commonly used in the medical field, especially medical imaging [9, 10].

A phased array system is able to use electronic scanning along the length of the linear array to conveniently create a B-scan from a single position [11]. This can be achieved by firstly choosing an aperture that is smaller than the size of the phased array to generate a beam and then selectively exciting elements corresponding to this aperture as it scans along the array [12]. Similarly, a C-scan can also be created by a phased array by physically moving the array along a single axis while the array is conducting the electronic scanning

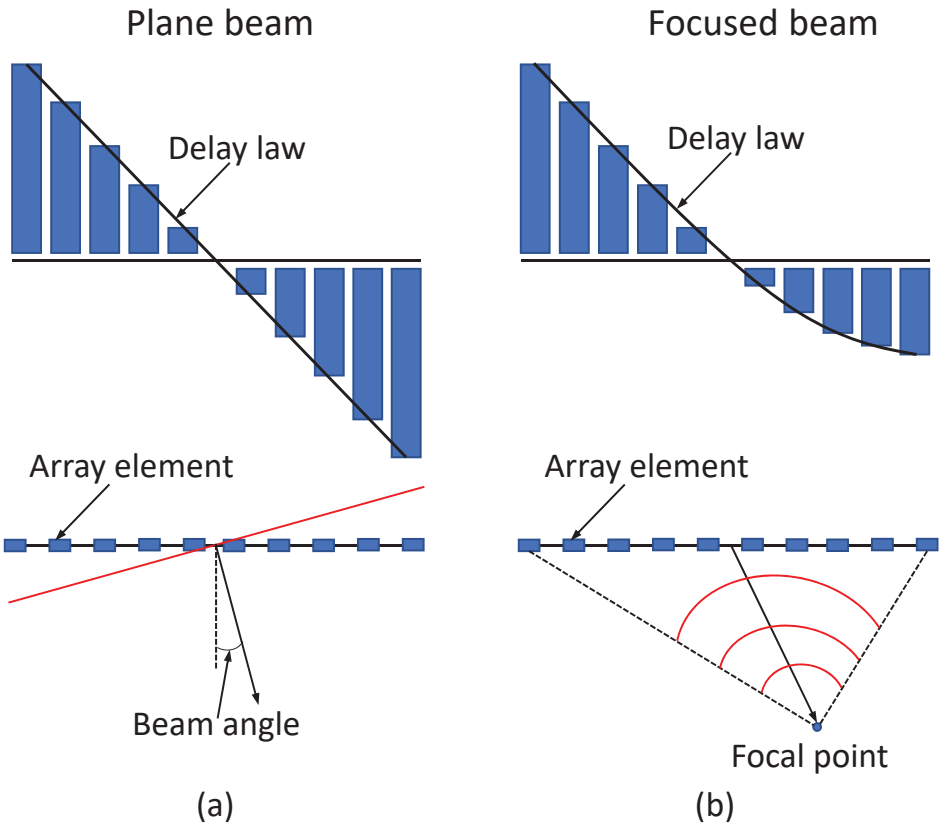


Figure 1.3: Diagrams show the delay laws of (a) a plane beam and (b) a focused beam.

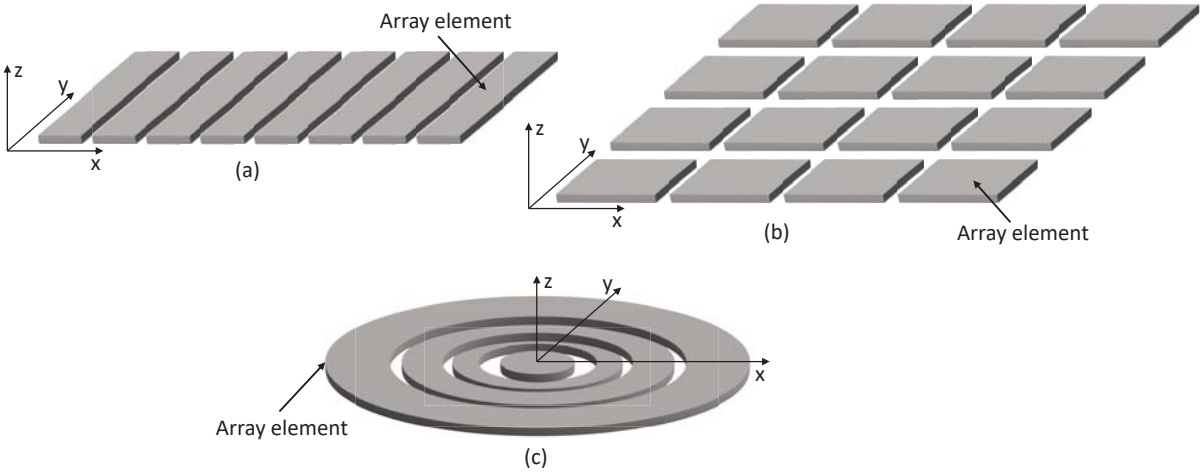


Figure 1.4: Common array definitions: (a) 1-D linear array, (b) 2-D array, (c) annular array.

along the array [12]. Furthermore, a phased array can also be used to create a sectional scan (S-scan) that represents a two dimensional cross-sectional view built from a series of stacked A-scans which have been created successively with respect to a number of beam angles with a fixed angle step [13], generated by adjusting the delay laws to excite in different directions. Moreover, the beams used to create the S-scan cannot only be plane beams but also be beams focused at a defined depth. The S-scan is nowadays the most common display mode of the phased array in industrial images or medical sonograms.

The focusing feature of phased arrays has also led to the development of the Beamforming (BF) [14, 15] imaging technique, a robust and efficient imaging technology which allows the reconstruction of the subsurface of the specimen under inspection. The intensity in a Beamforming image is obtained by steering a focused beam along a chosen planar section of the specimen under inspection, measuring the total backscattered energy from each focal point and plotting the amplitude as an image [15]. Beam steering can be achieved by transmitting with all the elements of an array simultaneously, with phasing, or by a post-processing technique once measurements from all the different send-receive combinations in the array have been acquired, an approach called Full Matrix Capture (FMC) [15–17]. Full Matrix Capture is a unique data acquisition technique developed for phased array. To complete the FMC process, each element in the array will be successively used as transmitter while all the other elements will be used as receivers and this process will repeat until all the elements have been fired [18], as shown in Fig. 1.5.

If we consider a phased array with N transducers, a symmetric matrix with $N \times N$ signals, which contains the maximum information for one scattering experiment, would be obtained after FMC. Much of the work done on the post-processing of FMC data has led to notable improvements in the BF imaging algorithms. Typical BF algorithms include the Total Focusing Method (TFM) [15], the Synthetic Aperture Focusing technique (SAFT) [19] and the wavenumber algorithm [20]. In particular, as TFM is able to provide a higher detection sensitivity and resolution [17] when compared to common beam-forming algorithms, TFM is now described as the 'gold standard' in some literature [21] and has already been widely applied in the NDE field [17, 22]. The mathematical basis and formulations of the TFM will be introduced in detail in Chapter 2. In recent years, the TFM has attracted the attention of a number of researchers and many variants of the

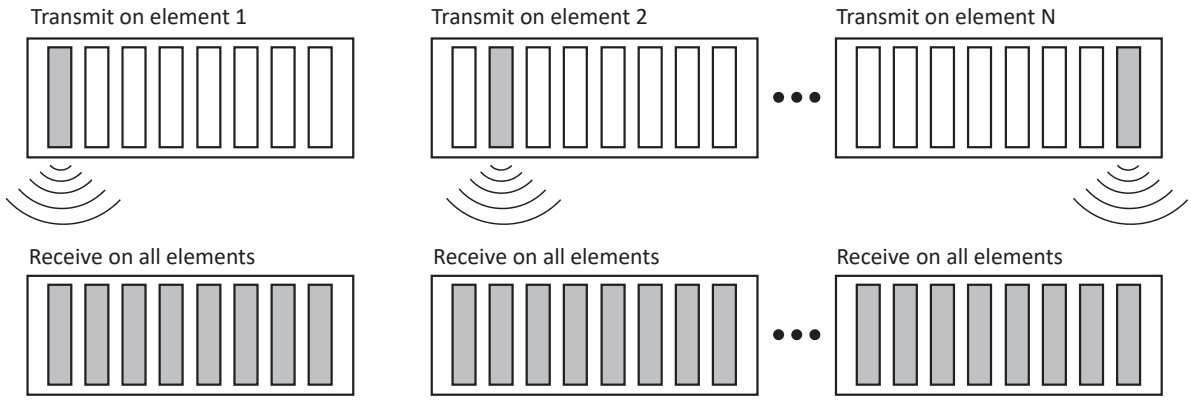


Figure 1.5: Transmitting and receiving procedure of the Full Matrix Capture.

TFM have been developed, such as the Almost Total Focusing Method (ATFM) [23], the Vector Total Focusing Method (VTFM) [24] and the Diffraction Total Focusing Method (DTFM) [25].

Recently, the demand for more cost-efficient modes of operation in some complex engineering systems, such as power plants, has driven the need to extend the life of components beyond their initial design life. This is achieved by replacing the components only when the existing defects have grown to a critical size, minimising conservatism. Thus, NDE, especially ultrasonic testing, is needed to inspect the components regularly. With the purpose of minimising the safety risk, the requirements of defect inspection and assessment are stringent for the crucial structural components during both manufacturing and service for power plants, especially for nuclear ones [26], which means more accurate and sensitive ultrasonic testing techniques are required. Furthermore, NDE is also essential to ensure that there are no significant defects in new components, and to find defects during service that could go on to grow to a critical size [27]. Thus, it is of great importance to extend current ultrasonic testing techniques to meet the requirements of localising and characterising small defects in high performance materials of safety-critical power plant components. Additionally, these structural components are designed to work in aggressive conditions, such as high temperature and high pressure, thus, the harsh operating conditions can result in fatigue cracks or stress corrosion cracks and these defects are commonly located near the backwall [28]. As pressure-containing pipes or vessels often do not allow access inside, the array should be placed on the front wall to conduct through-wall detection

of near backwall defects. In this situation, the existence of the planar backwall will dramatically affect the imaging result of the near backwall defect, and this phenomenon will be discussed in detail in Chapter 3. Another problem is that the material which suits the extreme working conditions, particularly for high temperature, often has large grains. Common examples of large grain materials are austenitic stainless steel welds and castings. In order to improve efficiency and reduce environmental impact, power plants are tending to increase operating temperature, which results in a rapid increase in the use of large grain material. The large grains of the material cause scattering of sound waves, which adds coherent noise to the signals and so makes ultrasonic testing more difficult to conduct.

However, the commonly used FMC and TFM technique is sometimes not effective enough to meet the above requirements. Firstly, the resolution of Beamforming algorithms are diffraction limited [29], where the diffraction limit refers to the theoretical 0.5 wavelength resolution limit [30]. That means the point scatterers which are separated by a distance smaller than 0.5 wavelength cannot be resolved through the TFM, as shown in Fig. 1.6(a). Besides, the material of the substance (typically air) within the defect is always considered impenetrable, that means the TFM can only reconstruct the top surfaces but not the whole shape of the defect. Fig. 1.6(b) shows an example of this, in which only the top surfaces of the side-drilled holes can be seen and the side-drilled holes also produce shadows that obscure parts of the backwall. Besides, TFM also shows limited ability to characterise surface-breaking notches. Several TFM imaging examples of surface-breaking notches are shown in Fig. 1.6(c). From these results, it is clear that TFM cannot reconstruct the whole shape of the surface-breaking notch and can only reconstruct a weak tip of the notch and a strong backwall. As the TFM image cannot directly reflect the real shape of the notch and the weak tip will be easily masked by noise, especially in large grain material, thus, the characterization (size and tilt angle) of the notch based on the TFM image will be difficult. Although Felice [31] has used the location difference between the indication of the notch tip and the indication of the backwall to accurately measure the notch size, this method is not able to size a notch whose size is smaller than two wavelengths and has not shown a good robustness to scattering noise in large grain material. According to the above limitations of the TFM, it demonstrates that the current Beamforming imaging

technique is not sufficient for the application if the requirement is to identify small near backwall defects in safety-critical components (large grain material), as for the detection of small cracks, it is necessary to guarantee high resolution and minimise artefacts to avoid false calls.

Another commonly used technique for through-wall defect sizing is the Time-Of-Flight Diffraction (TOFD) [32]. The essential idea of TOFD is to measure the flight time of the diffracted echoes from the two tips of the crack and calculate the crack depth with the knowledge of the geometry of the component. In [33], Baby et al. has evaluated the depths of the surface-breaking notches on the far surface using TOFD. The surface-breaking notches have a width of 0.5mm and their depths varying from 0.91mm to 30mm. They found the smallest notch that can be determined by TOFD when using a 4MHz probe has a depth of 1.82mm. The main limitation of TOFD is that TOFD has two dead zones, one is at top surface and another one is at bottom surface [34]. Although surface-breaking cracks can be detected by TOFD, defects close to the surface are typically not detectable because of the presence of dead zones [34]. The depth of these two dead zones depends on the probe frequency, transducer damping and TOFD configuration [35]. Lower frequencies and less transducer damping will increase dead zones, while higher frequencies and increased damping will result in smaller dead zones [35]. Typically, when using a 7.5MHz probe for sizing, the backwall dead zone is around 1mm [34]. Also, since TOFD relies on the tip diffracted signals, which are typically weak compared to a specular reflection from the crack or the back wall, it is not well suited when there is significant noise present. Based on the above facts, TOFD technique is not sensitive enough to size small near backwall defects.

Overcoming the limitations of current Beamforming technique means that more advanced techniques should be developed. Inverse methods [36–38] are one approach aimed at maximising the amount of information extracted from the measured data. In these approaches, a solution is sought where the scatterer produces a scattered field which matches what has been measured. Unlike Beamforming, inverse scattering tries to reconstruct the spatial distribution of material properties, which can also be referred as the object function. Having studied the interaction between the ultrasonic wave and the object, inverse scattering extracts the information which is encoded into measurements and provides a detailed im-

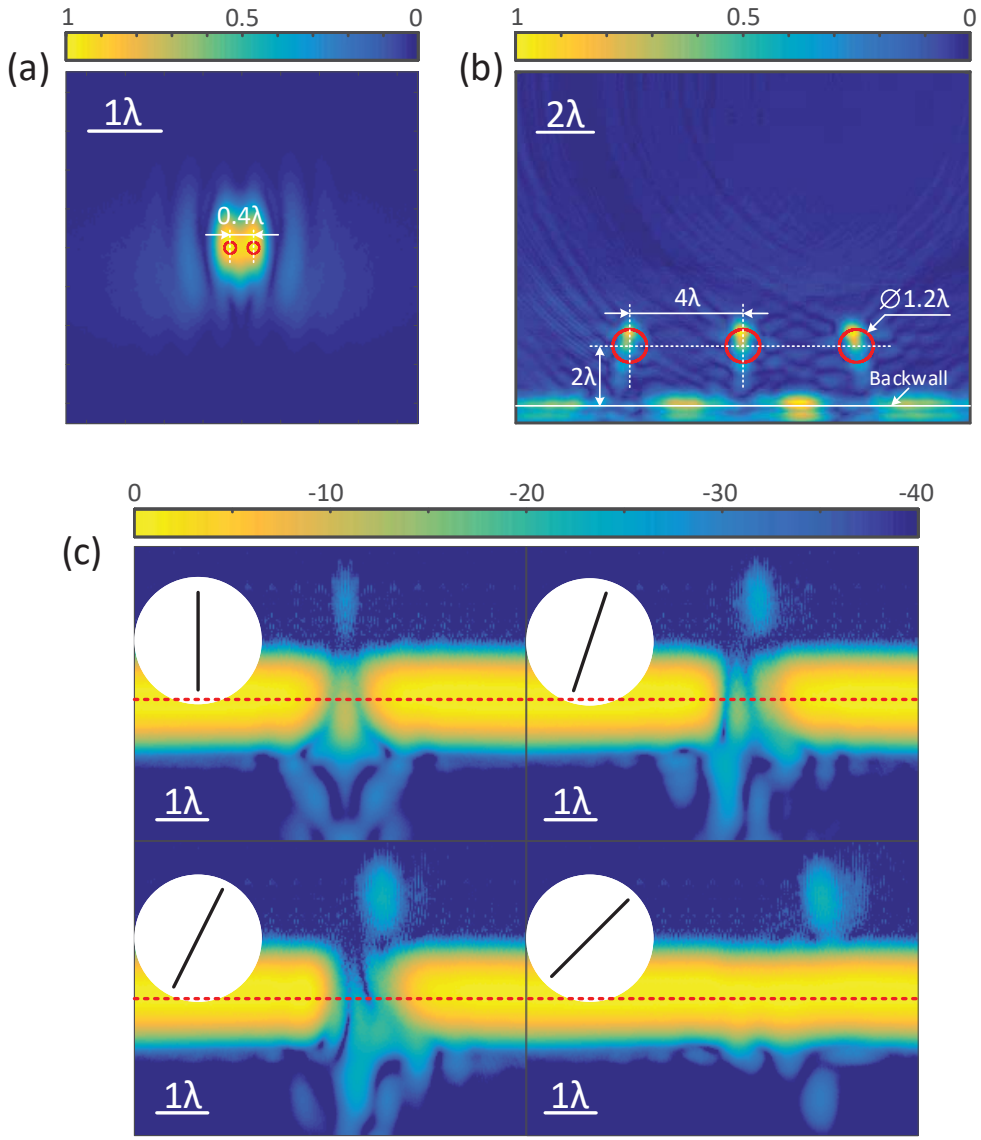


Figure 1.6: (a) A TFM image of two poorly resolved point scatterers, which are separated by 0.4λ; (b) A TFM image of three side-drilled holes in a 304L steel block; (c) TFM images of surface-breaking notches with different tilt angles. Note that the red dotted lines in the images were used to indicate the location of backwalls.

age of the features inside the specimen. The study of the concept of inverse scattering has led to super resolution imaging technologies which make achieving the resolution beyond the Rayleigh limit possible. For example, Dr. Francesco Simonetti has demonstrated that super resolution imaging can be achieved by considering the effect of multiple scattering [39, 40]. Although the potential of the inverse scattering approach is apparent, the practical implementation of this technique is much more challenging. The fundamental reason of this is that the inverse scattering suffers from the so called ill-posedness [38]. In an ill-posed problem, the true solution can be very sensitive to small changes in the data. As a result, the present super resolution imaging technologies are sensitive to noise and other uncertainties. In practice, only limited measurements can be obtained due to the limited number of array elements and limited locations for access of the ultrasonic array, thus the inverse scattering problem in the NDE field is actually a limited aperture problem. This will cause inverse scattering to be more ill-posed [41].

The aim of my project is to develop an integrated ultrasonic imaging technology for inspection of near backwall defects. The imaging technology would integrate novel approaches to post-process the matrix of signals obtained from the FMC measurements, imaging algorithms to reconstruct defect images and specific sizing methods to accurately characterise the defects from the reconstructed images, with the purpose to introduce a step change in the sensitivity of ultrasonic array imaging in the application of detecting near backwall defects, beyond what is possible by the capabilities of Beamforming.

1.2 Outline of Thesis

In this thesis, the imaging and characterization of near backwall defects using ultrasonic arrays is investigated.

In Chapter 2, the forward and inverse scattering theories are introduced. In order to help the reader understand these two problems successfully, a brief derivation of the governing equation of wave propagation is also included. The forward problem aims to find the corresponding scattered field given the incident field and the properties of the scatterer, while the inverse scattering problem aims to reconstruct the scatterer from a given incident field and measured scattered field. Different from the forward problem which is well-posed,

the inverse scattering problem is ill-posed. These problems are discussed under the Born approximation and when the effects of the multiple scattering is considered, respectively. In order to facilitate the discussion of subsequent chapters, the mathematical formulations of several imaging algorithms, including the Beamforming methods and super resolution methods, are also provided in this chapter.

A practical consideration of using ultrasonic arrays to detect and size near backwall defects is that the backwall will introduce strong effects that will dramatically influence imaging results. In Chapter 3, three methods, the FMC subtraction, the weighting function method and the truncation method, are developed as the response to the challenge of eliminating backwall effects for array imaging of near backwall defects. These three methods are based on different mathematical principles and have different application ranges. To validate the performance of these methods on representative array imaging data, an experiment is also included in this chapter.

In Chapter 4, the Factorization Method is applied to image and size surface-breaking notches. Furthermore, the effects of the FMC subtraction and the truncation method are also studied in detail. The work in this chapter includes both numerical simulations and experimental validations. The results show that if the backwall effects have already been eliminated by proper methods, the FM is able to accurately reconstruct and size a 1 wavelength notch which is hard to be characterized through the conventional Beamforming algorithms (i.e. the Total Focusing Method or the Half-Skip Total Focusing Method).

The development in the scattering theory and computing technology has led to the development of several novel imaging techniques, such as the Direct Sampling Method (DSM) and Fast Topological Imaging (FTIM). In Chapter 5, the Direct Sampling Method and Fast Topological Imaging are firstly applied to the inverse scattering problems of imaging near backwall defects by the Full Matrix Capture data. Brief introductions of the formulations and the mathematical basis of these methods are also included in this chapter in order to provide a general overview of these two methods. The DSM and the FTIM are used to image the side-drilled holes and different notches based on the FMC data in this chapter, and through the imaging experiments, we can conclude that the DSM and the FTIM can be effective alternatives to the Beamforming methods for ultrasonic array imaging.

All the backwall effects eliminating methods developed in Chapter 3 have considered a perfect smooth backwall, where the ultrasound wave from the backwall will undergo the specular reflection. In many cases, especially for the components working in harsh environments (e.g. high pressure and temperature), it is not possible for the component to have perfect smooth surfaces. Thus, in order to test the applicability of the developed backwall effects eliminating methods, these methods have been applied to image surface-breaking notches originated from backwalls with various roughnesses in Chapter 6 to find out the limit roughness of each method developed. This procedure has been completed through the numerical simulation in Chapter 6. Additionally, the theory about the scattered pattern from a rough surface and the numerical method used to construct a rough surface are briefly introduced in this chapter.

The main conclusions and contributions of this thesis are summarized in Chapter 7, and the potential areas of future work relating to the work in this thesis are also discussed in this chapter.

Chapter 2

Background theory

2.1 Introduction

This chapter introduces the underlying theory and formulation of the time harmonic obstacle scattering problem, which is necessary for understanding the theoretical and mathematical basis of the imaging algorithms studied in this thesis. The scattering theory considers the physical interaction between the sound wave and scatterers and describes how the information of properties of scatterers is encoded into the radiated wave field.

The forward scattering maps the properties of scatterers into the total wave field. It is a well-posed problem and can be solved by several numerical methods [42]. Inverse scattering predicts the properties of the scatterers based on the scattered wave field [38]. Inverse scattering is a non-linear problem, which means that, for inverse scattering, most imaging algorithms can only achieve approximate solution by assuming linearity [39]. It is also an ill-posed problem and regularization methods may be needed to deal with the ill-posedeness of it [38]. Regularization is the process by which unstable problems can be stabilized [43] and one commonly used regularization method is called Tikhonov regularization which tackles the non-linear problem by minimizing a Tikhonov function with a suitably chosen regularization term [44].

The introduction of the theoretical and mathematical basis of several imaging methods is also included in this chapter. The underlying approximation and theory of the Beamforming algorithm is described in this chapter, and also the resolution limit of the Beamforming

algorithm is introduced in detail. The concepts of a super resolution algorithm which can break the resolution limit is also described in this chapter. The formulation and mathematical basis of the different algorithms are provided as a tool to analyse the operating principles and resolution limits of these algorithms and also provided as the foundation for the following chapters where the described imaging algorithms will be investigated and applied to specific problems.

2.2 Governing Equation

Firstly, before discussing the scattering problem, it is necessary to start from the derivation of the wave equation. Although the scattering problem in the fields of non-destructive evaluation (NDE), medical imaging or geophysics is actually the scattering problem with elastic waves, the scattering problem in NDE is usually analysed using acoustic waves for simplicity as the inverse scattering with elastic waves is significantly more difficult than with acoustic waves and the acoustic wave itself is actually a type of longitudinal wave.

Consider an acoustic wave propagating through a medium, such as fluid, in free space. If there is no exterior force applying to the medium, the movement of the particles are governed by the following equations [38]:

$$\frac{\partial v}{\partial t} + (v \cdot \nabla)v + \frac{1}{\rho}\nabla\rho = 0 \ \texttt{(Euler's equation)}, \tag{2.1}$$

$$\frac{\partial \rho}{\partial t} + div(\rho v) = 0 \ \texttt{(Continuity equation)}, \tag{2.2}$$

$$f(\rho, S) = p \ \texttt{(Equation of state)}, \tag{2.3}$$

$$\frac{\partial S}{\partial t} + v \cdot \nabla S = 0 \ \texttt{(Adiabatic hypothesis)}, \tag{2.4}$$

where v(x,t), p(x,t), ρ(x,t), S(x,t) denote the velocity, pressure, density and specific entropy of a particle at $x \in \mathbb{R}^3$, respectively; ∇ represents the gradient, f is a function which depends on the fluid and div represents the divergence. Let assume that v, p, ρ and S are small perturbations of the static state $v_0 = 0$, $p_0 = constant$, $\rho_0 = constant$ and $S_0 = constant$. Then, according to [37], after the linearisation of above equations,

Eqs. (2.1-2.3) become

$$\frac{\partial v}{\partial t} + \frac{1}{\rho_0}\nabla p = 0, \tag{2.5}$$

$$\frac{\partial \rho}{\partial t} + \rho_0 div(v) = 0, \tag{2.6}$$

$$\frac{\partial p}{\partial t} - \frac{\partial f}{\partial \rho}(\rho_0, S_0)\frac{\partial \rho}{\partial t} = 0. \tag{2.7}$$

From these, the wave equation is obtained, which is given by

$$\frac{1}{c^2}\frac{\partial^2 p}{\partial t^2} = \Delta p, \tag{2.8}$$

where Δ is the Laplace operator and c represents sound speed and is defined as:

$$c^2 = \frac{\partial f}{\partial \rho}(\rho_0, S_0). \tag{2.9}$$

From Eq. (2.5), it is observed in [36] that there exists a velocity potential $U = U(x,t)$ which satisfies

$$v = \frac{1}{\rho_0}\nabla U,$$

and

$$p = -\frac{\partial U}{\partial t}. \tag{2.10}$$

It is clear that the velocity potential U also satisfies the wave equation

$$\frac{1}{c^2}\frac{\partial^2 U}{\partial t^2} = \Delta U. \tag{2.11}$$

For time-harmonic acoustic waves, U can be treated as the real part of a complex u:

$$U(x,t) = Re\{u(x)e^{-iwt}\}, \tag{2.12}$$

where the frequency $w > 0$. Using Eq. (2.11) and Eq. (2.12), the Helmholtz equation in

free space can be obtained:

$$\Delta u + k^2 u = 0, \tag{2.13}$$

where the k is the wavenumber and is given by $k = w/c$. According to the scattering theory [38], u is the sum of an incident field u_i and a scattered field u_s. The incident field is a solution to the Helmholtz equation in free space (Eq. 2.19), however, for the scattered field, the inhomogeneous medium should be compensated for. This situation is called scattering by an inhomogeneous medium. If an object D is impenetrable to the wave field, the obstacle scattering occurs and a boundary condition such as Dirichlet or Neumann is enforced on the boundary of the object [37]. In the Dirichlet case, $u = 0$ on the boundary ∂D of the object D while in the Neumann case, $\partial u/\partial \nu = 0$ on ∂D where ν is the unit outward normal vector to ∂D. For penetrable objects, the impedance boundary condition should be applied, which is formulated as $\partial u/\partial \nu + \Lambda u = 0$ on ∂D with some impedance Λ [37].

2.3 Forward scattering

As mentioned before, the purpose of the forward scattering is to calculate the scattered field given an incident field and the physical properties of the scatterers. The discussion here is restricted to the 2D acoustic obstacle and medium scattering problem [45] of acoustic waves in an unbounded homogeneous space $\mathbb{R}^2$ that contains inhomogeneity or obstacles in a domain $D \subset \mathbb{R}^2$. In order to characterize the inhomogeneity or the obstacles supported in the domain D, an object function $O(\boldsymbol{r})$is defined as

$$O(\boldsymbol{r}) = (n(\boldsymbol{r})^2 - 1)k^2 \quad x \in \mathbb{R}^2 \tag{2.14}$$

where $n(\boldsymbol{r})$ is the refractive index at a point $\boldsymbol{r}$ and is related to density and compressibility in acoustic cases. The expression of the refractive index is

$$n(\boldsymbol{r}) = \frac{c_0}{c(\boldsymbol{r})}, \tag{2.15}$$

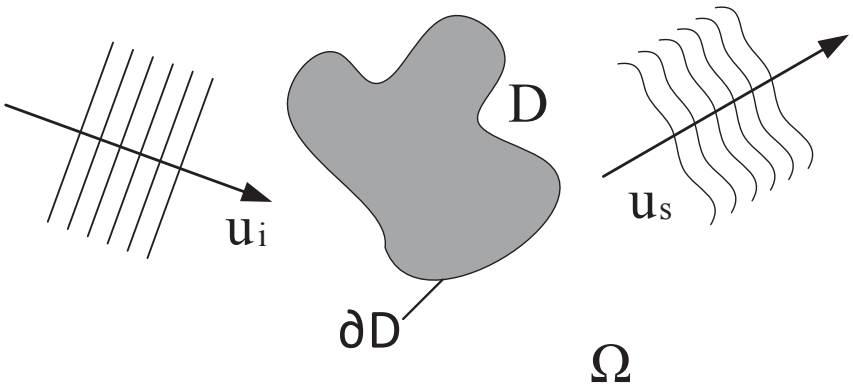


Figure 2.1: Schematic of the 2D scattering problem. The bounded Dirichlet obstacle D is illuminated from the incident field excited on surface Γ_i and the produced scattered field is measured on the surface Γ_m. Ω is the sampling domain where the obstacle D lies.

where c_0 is the sound speed of the background medium, and ρ and κ are the density and compressibility, respectively. Also, the refractive index n can be expressed by complex expansion

$$n(\boldsymbol{r}) = n_1(\boldsymbol{r}) + in_2(\boldsymbol{r}), \tag{2.16}$$

where $n_1(\boldsymbol{r})$ represents the real part and $n_2(\boldsymbol{r})$ represents the imaginary part. Consider the scattering problem set in Fig. 2.1. We define $\bar{D} \subset \mathbb{R}^2$ as the support of the object function, and $\bar{D}$ has a smooth boundary ∂D. We consider a planar incident wave with an incident direction $\hat{\boldsymbol{r}}_0$

$$u_i(\boldsymbol{r}, k; \hat{\boldsymbol{r}}_0) = e^{ik\hat{\boldsymbol{r}}_0 \cdot \boldsymbol{r}}, \tag{2.17}$$

where $k > 0$ is the wave number of the incident wave, $\hat{\boldsymbol{r}}_0 \in \mathbb{S}^1$ and $\mathbb{S}^1$ denotes a unit circle in $\mathbb{O}^2$. This denotes a planar wave field at point $\boldsymbol{r}$ due to an illumination from the direction $\boldsymbol{r_0}$. Also, let u_s be the scattered field, then the total field u can be expressed by

$$u = u_i + u_s, \tag{2.18}$$

According to [45], the propagation of the total field u is governed by the Helmholtz equation

$$\Delta u + k^2 n^2(\boldsymbol{r}) u = 0 \quad \text{in } \mathbb{R}^2 \setminus \overline{D}, \tag{2.19}$$

The above model is usually used to describe the inhomogeneous medium scattering problem, however, the acoustic Dirichlet obstacle can be treated as a limiting case of Eq. (2.19) as $n_2 \to \infty$ in Eq. (2.16). Considering Eq. (2.14), Eq. (2.19) becomes

$$(\Delta + k^2)u = -O(\boldsymbol{r})u, \tag{2.20}$$

For the scattered field, the Sommerfeld radiation condition should be satisfied to ensure all energy is radiated outwards towards infinity

$$\lim_{r\to\infty} \sqrt{r}(\frac{\partial u_s}{\partial r} - iku_s) = 0 \quad \text{for } r = |\boldsymbol{r}|. \tag{2.21}$$

Also, the Sommerfeld radiation condition must be understood to hold uniformly in all directions. It has been proven in [46] that solving the Eqs. (2.19)-(2.20) is a well-posed problem. As a result of the Sommerfeld radiation condition, for large $|\boldsymbol{r}|$, the scattered field u_s can be asymptotically formed in the expansion

$$u_s(\boldsymbol{r}, k; \hat{\boldsymbol{r}}_0) = \frac{e^{ikr}}{\sqrt{r}} u_\infty(\hat{\boldsymbol{r}}, k; \hat{\boldsymbol{r}}_0) + \mathcal{O}(\boldsymbol{r}^{-\frac{3}{2}}), \tag{2.22}$$

where $\hat{\boldsymbol{r}} := \boldsymbol{r}/|\boldsymbol{r}|$ and u_∞ is actually the far-field pattern of the scattered field u_s. In order to solve Eq. (2.20), the Green's function is introduced. The Green's function is the solution to

$$(\Delta + {k_0}^2)G(\boldsymbol{r}, k; \boldsymbol{r}') = \delta(|\boldsymbol{r} - \boldsymbol{r}'|), \tag{2.23}$$

where δ is the Dirac delta function. According to [29], the analytical solution of Eq. (2.23) is

$$G(\boldsymbol{r}, k; \boldsymbol{r}') = \begin{cases} -\frac{i}{4} H_0{}^{(1)}(kR) & \text{in 2D;} \\ \frac{exp(ikR)}{4\pi R} & \text{in 3D} \end{cases} \tag{2.24}$$

where $R = |\boldsymbol{r} - \boldsymbol{r}'|$ is the distance between the measurement point and the exciting point and $H_0{}^{(1)}$ is a zero order Hankel function of the first kind. As $|\boldsymbol{r} - \boldsymbol{r}'| \to \infty$, $G(\boldsymbol{r}, k; \boldsymbol{r}')$ has the asymptotic form in 2D

$$G_\infty(\hat{\boldsymbol{r}}, k; \boldsymbol{r}') = -\frac{e^{i(\frac{\pi}{4}+kr)}}{\sqrt{8\pi kr}} e^{-ik\hat{\boldsymbol{r}}\cdot\boldsymbol{r}'} \quad \text{for } r = |\boldsymbol{r}|. \tag{2.25}$$

By using the Green's function, the solution of Eq. (2.20) can be derived as

$$u(\boldsymbol{r}, k; \hat{\boldsymbol{r}}_0) = e^{ik\hat{\boldsymbol{r}}_0\cdot\boldsymbol{r}} - k^2 \int_D O(\boldsymbol{r}') u(\boldsymbol{r}', k; \hat{\boldsymbol{r}}_0) G(\boldsymbol{r}, k; \boldsymbol{r}') d\boldsymbol{r}'. \tag{2.26}$$

This is the Lippmann Schwinger equation which indicates the dependence of the total field on the incident field and its own value within D. The integration of the total field in Eq. (2.26) makes the forward scattering problem to be non-linear. For the far field ($r \to \infty$), Eq. (2.26) can be written as

$$u(\boldsymbol{r}, k; \hat{\boldsymbol{r}}_0) = e^{ik\hat{\boldsymbol{r}}_0\cdot\boldsymbol{r}} + k^2 \frac{e^{i\pi/4}}{\sqrt{8\pi k}} f(\hat{\boldsymbol{r}}, k; \hat{\boldsymbol{r}}_0) \frac{e^{ikr}}{\sqrt{r}} \quad \text{for } r = |\boldsymbol{r}|. \tag{2.27}$$

where

$$f(\hat{\boldsymbol{r}}, k; \hat{\boldsymbol{r}}_0) = \int_D O(\boldsymbol{r}') u(\boldsymbol{r}', k; \hat{\boldsymbol{r}}_0) e^{-ik\hat{\boldsymbol{r}}\cdot\boldsymbol{r}'} d\boldsymbol{r}'. \tag{2.28}$$

The term $f(\hat{\boldsymbol{r}}, \hat{\boldsymbol{r}}_0)$ refers to the scattering amplitude in some of the literature [39]. Eqs (2.18), (2.24-2.26) leads to

$$u_s(\boldsymbol{r}, k; \hat{\boldsymbol{r}}_0) = -k^2 \int_D O(\boldsymbol{r}') u(\boldsymbol{r}', k; \hat{\boldsymbol{r}}_0) G(\boldsymbol{r}, k; \boldsymbol{r}') d\boldsymbol{r}', \tag{2.29}$$

$$u_\infty(\hat{\boldsymbol{r}}, k; \hat{\boldsymbol{r}}_0) = -k^2 \int_D O(\boldsymbol{r}') u(\boldsymbol{r}', k; \hat{\boldsymbol{r}}_0) G_\infty(\hat{\boldsymbol{r}}, k; \boldsymbol{r}') d\boldsymbol{r}'. \tag{2.30}$$

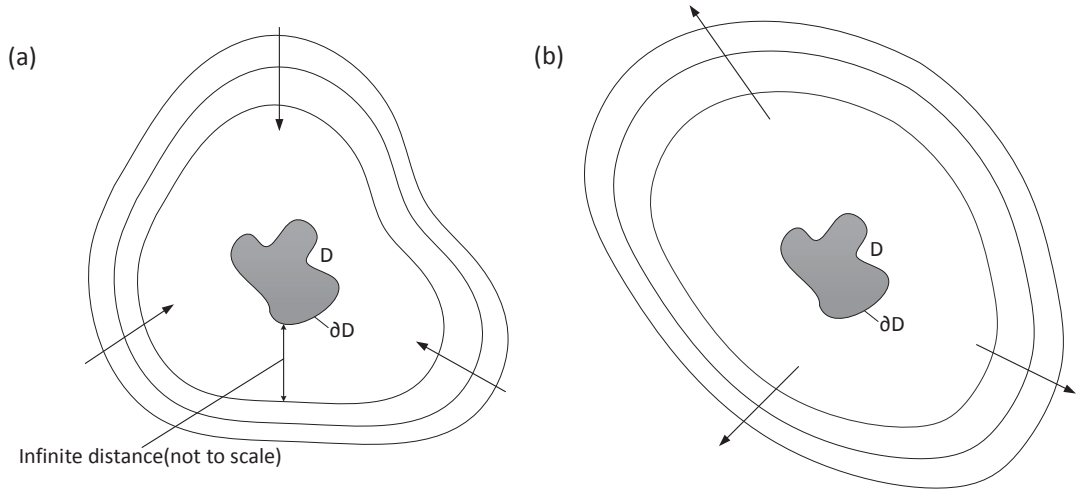


Figure 2.2: Schematic of the far-field scattering problem. (a) The object is illuminated from the far-field; (b) The scattered field is measured in the far-field.

Eq. (2.29) implies that the ideal imaging of the scatterers needs the knowledge of the pure scattered field from the scatterers, rather than the total field. However, in real inspections, it is the total field, which contains the incident field, the scattered components from the defect and from the structural features, that will be recorded by the phased array. In response, we proposed a method to extract the scattered field from the total field in Chapter 3 for the phased array subsurface imaging.

Solving Eqs. (2.18)-(2.21) is a well-posed problem [47] and several corresponding numerical methods for solving the forward problem can be found in [42, 48].

2.4 Spaces and operators

In real situations, it is impossible to excite and measure wave fields at every point; both the excitation and measurement must be taken at a set of discrete positions in the far field, as shown in Fig. 2.2. According to [49], the far-field scattering problem can be decomposed into three aspects: 1) the propagation of the incident field from the far-field to the object; 2) the interaction between the incident field and the object which produces a local perturbation to the incident field; 3) the radiation of the perturbation from the object to the far-field. Each of the three aspects can be described by a suitable mathematical operator.

To start the derivation, we shall first introduce an incident field v_g, which is defined as

$$v_g(\boldsymbol{r}) = \int_{\mathbb{S}^2} e^{ik\boldsymbol{r}\cdot\hat{\boldsymbol{r}}_0} g(\hat{\boldsymbol{r}}_0) ds(\hat{\boldsymbol{r}}_0), \tag{2.31}$$

where g is called the Herglotz density, physically corresponding to the amplitude of plane waves in each direction $\boldsymbol{r}_0$ which are superposed to form the incident field, r is a point in space illuminated by the incident wave, and v_g is also called the Herglotz wavefunction. Here, $\mathbb{S}^2$ denotes the unit sphere in $\mathbb{R}^3$. Eq. (2.31) also leads to the definition of the Herglotz operator $H : L^2(\mathbb{S}^2) \to L^2(\partial D)$, given by

$$(Hg)(\boldsymbol{r}) = \int_{\mathbb{S}^2} e^{ik\boldsymbol{r}\cdot\hat{\boldsymbol{r}}_0} g(\hat{\boldsymbol{r}}_0) ds(\hat{\boldsymbol{r}}_0). \tag{2.32}$$

The Herglotz operator actually maps the illumination functions g to the actual incident wave v_g on the boundary of the object. Then, in order to transform the incident field inside the object into a source distribution ψ that characterizes the perturbation to the incident field, the interaction operator $S : L^2(\partial D) \to L^2(\partial D)$ is introduced, which is given by

$$\psi(\boldsymbol{r}) = (Sv_g(\boldsymbol{r})) = O(\boldsymbol{r}) v_g(\boldsymbol{r}). \tag{2.33}$$

Similarly, it is also possible to define a radiation operator $H^* : L^2(\partial D) \to L^2(\mathbb{S}^2)$ that maps a continuous distribution of point sources in ∂D with strength defined by the continuous function ψ into the far-field pattern of the scattered field, u_s^∞, i.e.

$$u_s^\infty(\boldsymbol{r}) = (H^*\psi)(\boldsymbol{r}) = \int_{\partial D} e^{-ik\hat{\boldsymbol{r}}_0\cdot\boldsymbol{r}} \psi(\hat{\boldsymbol{r}}_0) d(\hat{\boldsymbol{r}}_0). \tag{2.34}$$

where H^* is also the adjoint operator of H. Finally, according to [37], the far-field operator $F : L^2(\mathbb{S}^2) \to L^2(\mathbb{S}^2)$ can be built from the scattering amplitude $f(\hat{\boldsymbol{r}}, k; \hat{\boldsymbol{r}}_0)$, so that

$$(Fg)(\hat{\boldsymbol{r}}) = \int_{\mathbb{S}^2} f(\hat{\boldsymbol{r}}, k; \hat{\boldsymbol{r}}_0) g(\hat{\boldsymbol{r}}_0) ds(\hat{\boldsymbol{r}}_0). \tag{2.35}$$

This compact operator F is of great importance as it forms the basis of the Linear

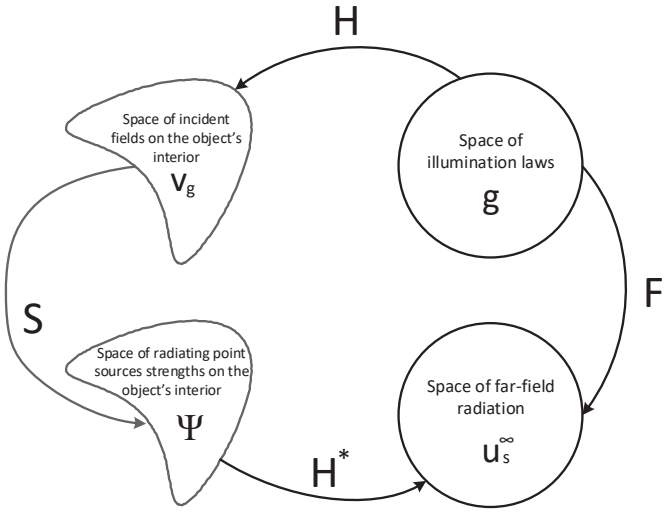


Figure 2.3: Schematic of the far-field scattering problem. (a) The object is illuminated from the far-field; (b) The scattered field is measured in the far-field.

Sampling Method (LSM) and the Factorization Method (FM). The left hand term, Fg, is actually equivalent to the far-field pattern of the scattered field, i.e. u_s^∞, created by the incident field v_g defined in Eq. (2.31). Because of this, it is possible to decompose the far-field operator into the three main aspects of the scattering process, as shown in Fig. 2.3. Based on this decomposition, it is easy to have

$$u_s^\infty = Fg = H^* S H g, \tag{2.36}$$

which then leads to the factorization of the far-field operator

$$F = H^* S H, \tag{2.37}$$

This factorization is the basis of the Factorization Method and is responsible for its name. Eq. (2.35) indicates that the scattering amplitude uniquely defines the far field operator. Although this factorization is derived in the frequency domain in this thesis, it is valid in both time and frequency domain. By using the far-field operator F, it is possible to calculate the scattered field with any input incident field. The scattering amplitude can be measured experimentally by illuminating with planar waves from all the possible directions, and recording the scattered field in each case. After obtaining the scattering

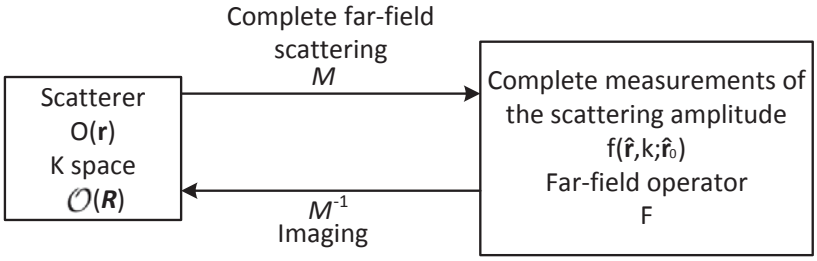


Figure 2.4: The operator, M, maps the object function to scattering amplitude. Note that $\mathcal{O}(\boldsymbol{R}) :== \mathcal{F}[O](\boldsymbol{r})$, where $\mathcal{F}$ means the Fourier transform and R is the spatial frequency.

amplitude, the far field operator F can be calculated.

For a single scattering experiment, the scattering amplitude only depends on the object function $O(\boldsymbol{r})$. Thus, we can define another operator M which maps the object function to the scattering amplitude:

$$f(\hat{\boldsymbol{r}}, k; \hat{\boldsymbol{r}}_0) = MO(\boldsymbol{r}) \tag{2.38}$$

where M is called the complete far field scattering operator, and its inverse M^{-1} is the imaging operator. The mapping of M is shown in Fig. 2.4

2.5 Inverse scattering

The inverse scattering problem, which is also called the imaging problem, aims to reconstruct the object function given the far field measurements of the scattered field. Referring to Fig. 2.4, the imaging problem needs to discover an explicit form of the imaging operator M^{-1} which allows the calculation of the object function $O(\boldsymbol{r})$ when the scattering amplitude $f(k\hat{\boldsymbol{r}}, k\hat{\boldsymbol{r}}_0)$ is given. As it is impossible to measure the wave fields at every point, the knowledge of the scattering amplitude $f(k\hat{\boldsymbol{r}}, k\hat{\boldsymbol{r}}_0)$ is not complete and only contains a sub-set of the whole information. Additionally, the imaging operator M^{-1} is non-linear, and the determining of M^{-1} is ill-posed [50]. As a result, in almost all cases it is impossible for us to calculate a complete and exact form of M^{-1}, and therefore, an exact reconstruction of $O(\boldsymbol{r})$ is impossible in general. A more serious problem is that a small amount of noise due to the inaccuracies of sensors and measurements could lead to artefacts on the reconstruction of $O(\boldsymbol{r})$ because of the ill-posedness of determining M^{-1}.

Although the non-linearity and ill-posedeness of the imaging operator makes it impossible to calculate an explicit form of M^{-1}, an iterative optimisation method can be used to calculate a simple implicit form of M^{-1}. An estimation $\hat{O}(\boldsymbol{r})$ of the object function can be found by minimizing:

$$\hat{O}(\boldsymbol{r}) = argmin_{\hat{O}(\boldsymbol{r})}||M(\hat{O}(\boldsymbol{r})) - f(\hat{\boldsymbol{r}}, k; \hat{\boldsymbol{r}}_0)|| \tag{2.39}$$

By simplifying M and using suitable searching techniques, the estimation of $O(\boldsymbol{r})$ can have a high accuracy. However, the problems of this method are that the iteration process is often time consuming and the space being searched could contain many local minima. Because of these problems, in order to achieve a rapid estimation of $O(\boldsymbol{r})$, many imaging methods have been developed to construct a linearised estimation of M^{-1}.

2.6 Beamforming imaging methods

With the development and application of inverse scattering theory and computing technology, the imaging algorithms developed for phased array imaging have advanced significantly in recent years. Among all the existing imaging algorithms, the Beamforming methods are most common and are able to provide a direct image of the shape of the defect under detection. Typical examples include the Total Focusing Method (TFM) [15], the Synthetic Aperture Focusing Technique (SAFT) [19] and the inverse wave-field extrapolation [51]. These algorithms have been proved to provide reliable imaging of the defect but their resolution is diffraction limited, i.e. the highest resolution is half a wavelength which can only be achieved with full view.

2.6.1 Born approximation

The Born approximation is a linear scattering approximation which aims to simplify the scattering problem and make non-iterative imaging possible. It can be used directly for Diffraction Tomography (DT), and is also implied in other algorithms, such as the Beamforming Methods. The Born approximation is valid when the medium is weakly scattering, i.e. the contrast between the background, and the inhomogeneities is small

and the size of the object is small relative to the wavelength. Generally, the condition to ensure the validity of the Born approximation is:

$$\sup_{r<\varrho} |O(\boldsymbol{r})| < C\frac{\lambda}{\varrho} \tag{2.40}$$

where ϱ refers to the characteristic size of the object and C is a constant with several proposed values [39]. If the Born approximation is valid, we can assume:

$$u_s \ll u_i \tag{2.41}$$

Then, after replacing the total field with the incident field, the far-field pattern of the scattered field becomes:

$$u_\infty(\hat{\boldsymbol{r}}, k; \hat{\boldsymbol{r}}_0) = -k^2 \int_D O(\boldsymbol{r'}) u_i(\boldsymbol{r'}, k; \hat{\boldsymbol{r}}_0) G_\infty(\hat{\boldsymbol{r}}, k; \boldsymbol{r'}) d\boldsymbol{r'} \tag{2.42}$$

Eq. (2.42) provides a linear relationship between the scattered field and the object function. Under the Born approximation, M_{Born}, i.e. the approximation of M, is well-defined and linear, and it also allows the non-iterative construction of a linear and well-defined M_{Born}^{-1}. As these two operators are explicit and simple, they allow a fast calculation of an approximation of the object function, which results in several classical imaging algorithms, such as Beamforming and Diffraction Tomography.

Using the Born approximation is fast and robust for imaging problems, but it also brings a resolution limit. This can be seen by observing that the Born approximation allows a direct mapping from the scattering amplitude to the spatial frequencies of the object function. The spatial frequencies of the object function are also called the K space which is defined as:

$$\hat{O}(\boldsymbol{R}) = \mathcal{F}[O](\boldsymbol{r}) \tag{2.43}$$

where $\mathcal{F}$ means the Fourier transform and $\boldsymbol{R}$ is the spatial frequency. For a planar incident

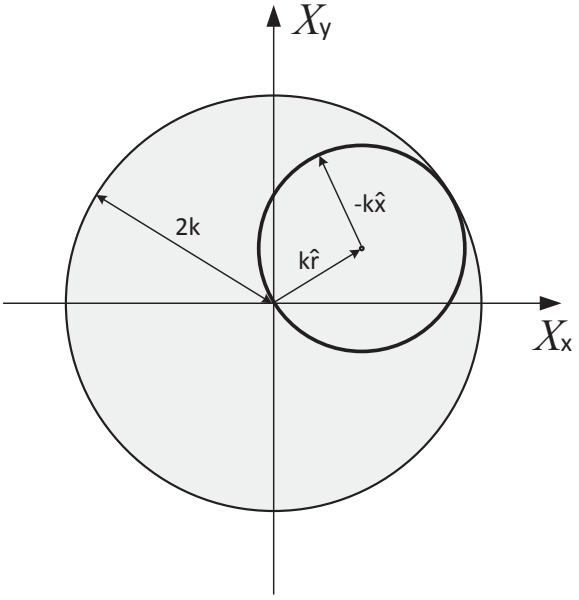


Figure 2.5: The Ewald limiting circle of radius $2k$. The spatial frequencies of the scatterer outside the Ewald limiting circle cannot be measured under Born approximation.

wave, the scattering amplitude will become:

$$f(\hat{\boldsymbol{r}}, k; \hat{\boldsymbol{r}}_0) = \int_D O(\boldsymbol{r'}) e^{ik(\hat{\boldsymbol{r}}_0 - \hat{\boldsymbol{r}}) \cdot \boldsymbol{r'}} dr' \tag{2.44}$$

Eq. (2.44) provides a direct mapping from the scattering amplitude to the spatial Fourier transform of the object function:

$$f(\hat{\boldsymbol{r}}, k; \hat{\boldsymbol{r}}_0) \propto \hat{O}(k(\hat{\boldsymbol{r}}_0 - \hat{\boldsymbol{r}})) \tag{2.45}$$

It can be seen that by varying $\hat{\boldsymbol{r}}$ and $\hat{\boldsymbol{r}}_0$ around all the possible angles, the value of every spatial frequency in the Ewald disk [39] can be measured. However, the spatial frequency outside the circle (greater than $2k$) cannot be measured, as shown in Fig. 2.5; thus, the highest resolution that the imaging methods based on the Born approximation can achieve is $\lambda/2$.

The Born approximation essentially neglects the effects of multiple scattering between features of the object by assuming a simplified scattered field inside the object. Thus, under Born approximation, if an object consists of several features, the scattering field generated by the whole object is actually the superposition of the independent scatter-

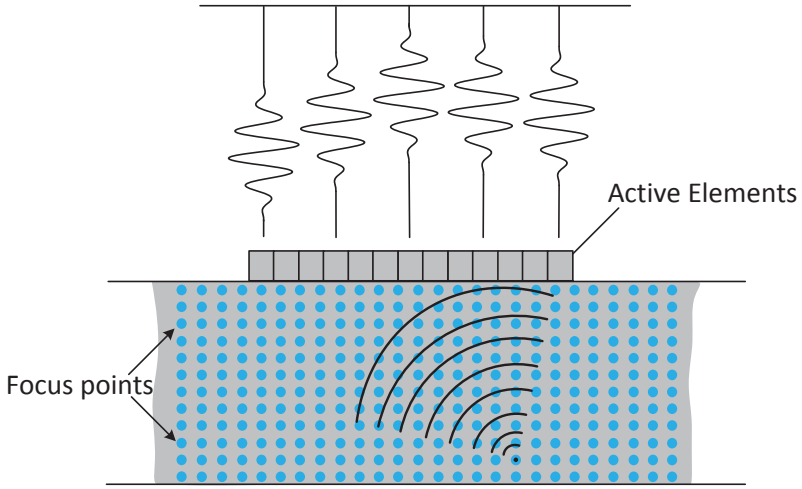


Figure 2.6: Schematic of the working process of the Total Focusing Method.

ing field generated by each feature of the object separately. The effects of the multiple scattering are discussed in Section 2.7.1.

2.6.2 Total Focusing Method

The Total Focusing Method (TFM), which is also known as a version of Beamforming (BF), is one of the most widely used imaging methods to determine the locations of point scatterers [15]. It is implemented by focusing a sound beam to each point in the interested region and recording the reflections from these points. The schematic of the working process of the Total Focusing Method is shown in Fig. 2.6. Recalling Eq. (2.42) and simply replacing the incident field by the equivalent Green's function, we can obtain

$$u_\infty(\hat{\boldsymbol{r}}, k; \hat{\boldsymbol{r}}_0) = -k^2 \int_D O(\boldsymbol{r'}) G(\boldsymbol{r'}, k; \hat{\boldsymbol{r}}_0) G(\hat{\boldsymbol{r}}, k; \boldsymbol{r'}) d\boldsymbol{r'}. \tag{2.46}$$

This equation can further be simplified if we consider a situation of a single point scatter. Then, the integration in Eq. (2.46) becomes

$$u_\infty(\hat{\boldsymbol{r}}, k; \hat{\boldsymbol{r}}_0) = G(\boldsymbol{r'}, k; \hat{\boldsymbol{r}}_0) Q G(\hat{\boldsymbol{r}}, k; \boldsymbol{r'}), \tag{2.47}$$

where Q refers to the scattering potential at $\boldsymbol{r'}$. Eq. (2.47) can be rearranged to calculate the potential for a single point scatterer if the location of the point scatterer and the

measurements of the scattering are known as

$$Q = \frac{u_\infty(\hat{\boldsymbol{r}}, k; \hat{\boldsymbol{r}}_0)}{G(\boldsymbol{r'}, k; \hat{\boldsymbol{r}}_0) G(\hat{\boldsymbol{r}}, k; \boldsymbol{r'})}. \tag{2.48}$$

The factor $1/G$ corrects the scattered field by accounting for the phase shifts and the changes in amplitude due to wave propagation. Conventionally, instead of the Green's function, the steering function is used in the TFM as only the phase shifts need to be considered. However, this could be important in quantitative imaging. In real applications, there are always several pairs of transmitters and receivers. By taking all of the transducers into the calculation, the intensity at a point $\boldsymbol{z}$ is

$$I^{BF}(\boldsymbol{z}) = \int_\Gamma \int_\Gamma \frac{u_\infty(\hat{\boldsymbol{r}}, k; \hat{\boldsymbol{r}}_0)}{exp(-ik\hat{\boldsymbol{r}} \cdot \boldsymbol{z}) exp(-ik\hat{\boldsymbol{r}}_0 \cdot \boldsymbol{z})} d\hat{\boldsymbol{r}}_0 d\hat{\boldsymbol{r}}, \tag{2.49}$$

where $\Phi_\infty(\hat{\boldsymbol{r}}, k; \boldsymbol{z}) = exp(-ik\hat{\boldsymbol{r}} \cdot \boldsymbol{z})$ is known as the steering function and Γ represents the aperture of the transducer array, which denotes some subset of $\mathbb{S}^1$, a unit circle in $\mathbb{R}^2$. As the transducers are actually discrete, the integrations in Eq. (2.49) are replaced by a discrete sum in real calculations. If a scatterer is located at the imaging point, it will have a large intensity due to the coherent sum; otherwise, the sum would be small as the values cancel themselves out.

The TFM image is a filtered version of diffraction tomography (DT), as a result, the DT image can be obtained by deconvolving the TFM results; and this is used by HARBUT [52], a novel high resolution imaging method. These two methods all neglect multiple scattering [39,53] and share the same fundamental resolution limit, i.e. $\mathcal{O}(\boldsymbol{R}) = 0 \forall R > 2k$.

In real NDE systems, the TFM can be implemented by introducing a combination of time delays to the transducer array and recording the reflections from every point. Another approach to implement TFM is to use it as a post processing method after all the information has been obtained though Full Matrix Capture (FMC) [54]. Once the FMC is completed, the symmetrical signal matrix, which contains the maximum information for one scattering experiment, can be post processed by TFM. According to [15], based on

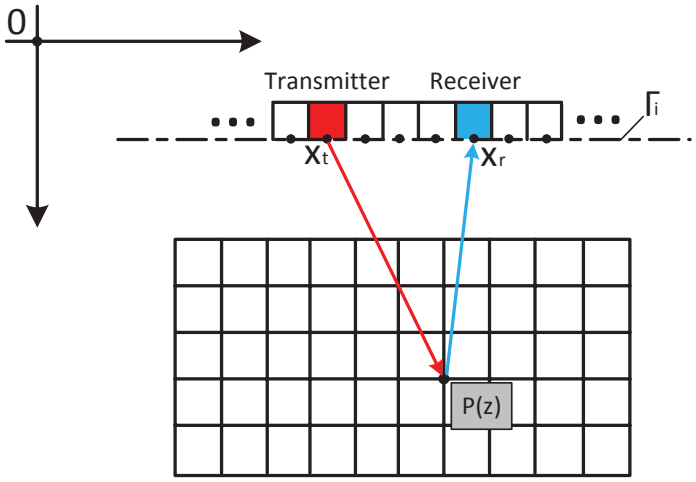


Figure 2.7: Schematic of the configuration of the Total Focusing Method.

the imaging setup shown in Fig. 2.7, the indicator function of TFM is given by

$$\begin{aligned} I_{TFM}(\boldsymbol{z}) &= \int_{\Gamma_i}\int_{\Gamma_i} U^S(\boldsymbol{x_r}, \frac{|\boldsymbol{x_t}-\boldsymbol{z}|+|\boldsymbol{x_r}-\boldsymbol{z}|}{c_0}; \boldsymbol{x_t}) ds(\boldsymbol{x_r}) ds(\boldsymbol{x_t}) \\ &= \sum_{t,r=1}^{N} U^S(\boldsymbol{x_r}, \frac{|\boldsymbol{x_t}-\boldsymbol{z}|+|\boldsymbol{x_r}-\boldsymbol{z}|}{c_0}; \boldsymbol{x_t}), \end{aligned} \tag{2.50}$$

where Γ_i is the surface where the array is located, $\boldsymbol{x_t} \in \Gamma_i$ is the location of the transmitter, $\boldsymbol{x_r} \in \Gamma_i$ is the location of the receiver and $U^S(\boldsymbol{x_r}, t; \boldsymbol{x_t})$ denotes the time domain scattered data from a transducer located at $\boldsymbol{x_t}$ to a receiver located at $\boldsymbol{x_r}$.

2.6.3 Half-Skip Total Focusing Method

The Half-Skip Total Focusing Method (HSTFM) is a modified Total Focusing Method (TFM) developed for imaging and sizing near backwall defects [31,55]. The results showed that the HSTFM has the ability to size a 1.5 wavelength surface-breaking crack that is impossible to be measured through the conventional TFM, however, the HSTFM still had a poor accuracy for the cracks smaller than 1.5 wavelength [31]. Like the TFM, the HSTFM is also based on the weak scattering approximation (e.g., the Born approximation), so there is a fundamental resolution limit (0.5 wavelength) that will limit the application of this method in high resolution imaging [39].

The ray path considered in TFM is the direct ray path, that is the wave directly travels

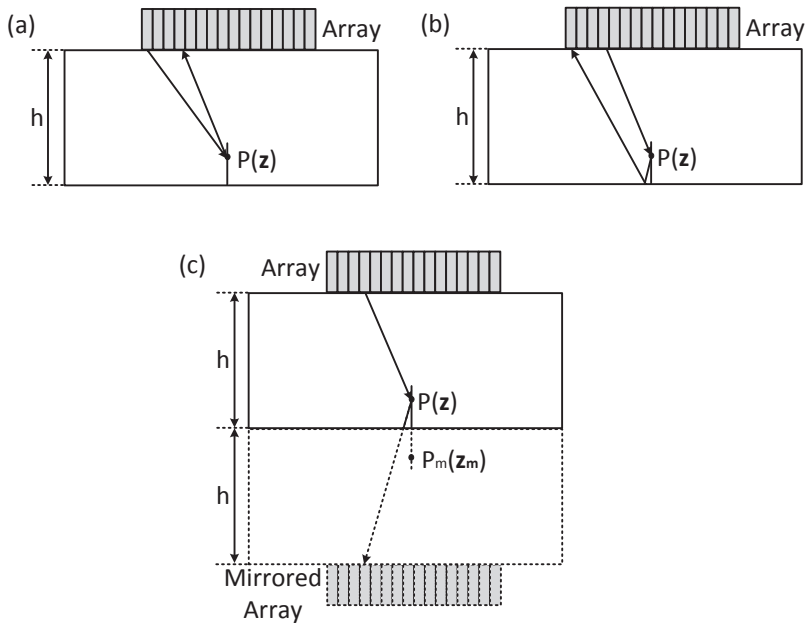


Figure 2.8: (a) Example of the direct ray path considered in TFM, (b) Example of the 'half-skip' ray path considered in HSTFM, (c) Equivalent ray path of the ray path considered in (b).

from the transmitter to the image point P and back to the receiver, as shown in Fig. 2.8(a). However, in the case of detecting the near backwall defect, there is additional complexity from the wave reflecting from the backwall, which is not accounted for in TFM. In response, Lorenz et al. [56] developed the Half-Skip Total Focusing Method (HSTFM) to image and size the near backwall defects. Unlike TFM, HSTFM considers the 'half-skip' ray paths which are reflected on the backwall once, either before or after interacting with the defect, as shown in Fig. 2.8(b).

Imagine that there is a mirrored imaging point P_m located at z_m, as shown in Fig. 2.8(c). The length of the post-defect reflection half-skip path defined in Fig. 2.8(b) is that of a path from the real array to the imaging point P and then from the point P back to the mirrored array, as shown in Fig. 2.8(c). It is obvious that the ray path from the point P to the mirrored array is equivalent to the ray path from the mirrored point P_m to the real array. It is noted that the same is true for a pre-defect reflection by reciprocity. Based

on this, the indicator function of HSTFM is given by

$$\begin{aligned} I_{HSTFM}(\boldsymbol{z}) &= \int_{\Gamma_i}\int_{\Gamma_i} U^S(\boldsymbol{x_r}, \frac{|\boldsymbol{x_t}-\boldsymbol{z}|+|\boldsymbol{x_r}-\boldsymbol{z_m}|}{c_0}; \boldsymbol{x_t}) ds(\boldsymbol{x_r}) ds(\boldsymbol{x_t}) \\ &= \sum_{t,r=1}^{N} U^S(\boldsymbol{x_r}, \frac{|\boldsymbol{x_t}-\boldsymbol{z}|+|\boldsymbol{x_r}-\boldsymbol{z_m}|}{c_0}; \boldsymbol{x_t}), \end{aligned} \tag{2.51}$$

where Γ_i is the surface where the array is located, $\boldsymbol{x_t} \in \Gamma_i$ is the location of the transmitter, $\boldsymbol{x_r} \in \Gamma_i$ is the location of the receiver and $U^S(\boldsymbol{x_r}, t; \boldsymbol{x_t})$ denotes the time domain scattered data from a transmitter located at $\boldsymbol{x_t}$ to a receiver located at $\boldsymbol{x_r}$.

2.7 Super resolution methods

Super resolution is actually a collective name for a number of different methods which can have super resolution, i.e. a resolution exceeding the traditional $\lambda/2$ limit. These different methods always have different implementations and may have different assumptions. One successful optical approach of super resolution is called near field scanning optical microscopy (NSOM). NSOM is based on a direct measurement of the near field scattered wave which contains evanescent waves. The evanescent wave has a spatial wavenumber greater than w/c; and it is fundamental to achieve super resolution [39]. NSOM scans closely to the surface of the scatterers using a sharp glass fibre; then, the evanescent wave propagates along the fibre and is measured in the far field. NSOM is able to achieve a resolution higher than $\lambda/20$ but is not suitable for sub-surface imaging as all of the excitations and measurements typically must be conducted in the far field (at the surface of a component).

Another successful super resolution method, the qualitative inverse scattering method, which was developed recently, is also a post-processing technique which can be used for ultrasonic phased array imaging [39]. The approach is a non-iterative method for obstacle reconstruction with the knowledge of the measured data of the far/near scattered field. The qualitative method does not resort to the weak scattering approximation (i.e. Born approximation) and considers the effect of multiple scattering [39, 53]. Besides, this method is established to reconstruct the shape of the inhomogeneities inside the material

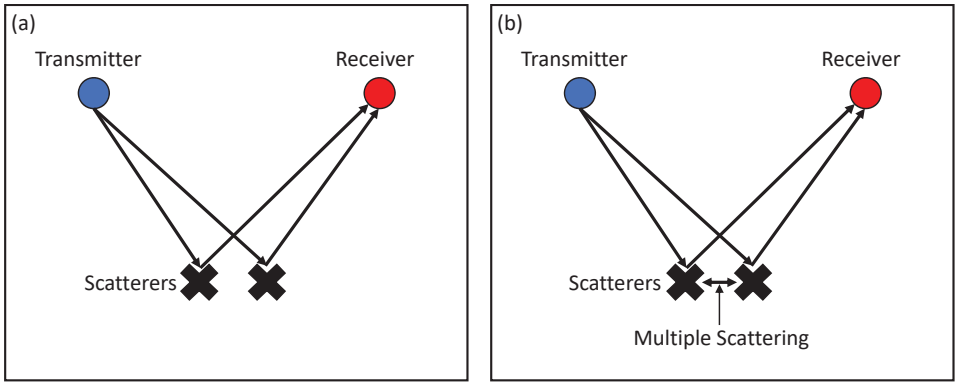


Figure 2.9: Simple case of two scatterers to show the scattered fields with or without multiple scattering. (a) Path of scattering field under Born approximation; there is no interactions between the scattered fields and the targets, (b) Path of scattering field considering multiple scattering; there are interactions between the scattered fields and the targets.

rather than the quantitative values of the object function.

The recent development in the qualitative method has led to the establishment of the Linear Sampling Method (LSM) by Colton [57] and Factorization Method (FM) by Kirsch [37]. The Factorization Method is a recent algorithm for the reconstruction of a scatterer [58–60] and is developed as an alternative to the Linear Sampling Method. Since being established, the FM has attracted much research consideration and has already been successfully applied to different inverse scattering problems [61–63]. Recently, the application of the FM in ultrasonic testing to achieve super resolution imaging (i.e. beyond the Rayleigh limit) has become a focus. For example, Simonetti [40] has proved that the Linear Sampling Method (LSM) and FM can achieve a super resolution imaging and the feasibility of the super resolution was validated through a limited view experiment performed on a metallic plate. A similar result was obtained by Hutt [64] that the FM is able to achieve a resolution better than the Rayleigh limit in the application of ultrasonic phased array imaging.

2.7.1 Multiple scattering

As discussed in Section 2.6.1, under the Born approximation, the effects of multiple scattering between features of the object are neglected. A simple example of the scattered field under the Born approximation is shown in Fig. 2.9, in which there are two scatter-

ers illuminated by an incident field. Under the Born approximation, the scattered field generated by one scatterer will not interact with the other one. However, if the effects of multiple scattering are considered, the interactions of the fields scattered by different features will exist and contribute to the far-field measured, which has been proved to exist in experiments in [65]. The effects of multiple scattering are shown schematically in Fig. 2.9(b).

The discussion of the effects of multiple scattering also starts from the expression of scattering amplitude. If we replace the total field by the sum of incident field and scattered field in Eq. (2.28), we can get

$$f(\hat{\boldsymbol{r}}, k; \hat{\boldsymbol{r}}_0) = \int_D O(\boldsymbol{r'})(e^{ik\hat{\boldsymbol{r}}_0 \cdot \boldsymbol{r'}} + u_s(\boldsymbol{r'}, k; \hat{\boldsymbol{r}}_0))e^{-ik\hat{\boldsymbol{r}} \cdot \boldsymbol{r'}} d\boldsymbol{r'}, \tag{2.52}$$

Then, it can be further rearranged as

$$f(\hat{\boldsymbol{r}}, k; \hat{\boldsymbol{r}}_0) = \hat{O}(k(\hat{\boldsymbol{r}} - \hat{\boldsymbol{r}}_0)) + \int_D e^{-ik\hat{\boldsymbol{r}} \cdot \boldsymbol{r'}} O(\boldsymbol{r'}) u_s(\boldsymbol{r'}, k; \hat{\boldsymbol{r}}_0) d\boldsymbol{r'}. \tag{2.53}$$

The first term of the right hand side of Eq. (2.53) is the scattering amplitude under the Born approximation, defined by Eq. (2.44). It can also be shown that the integration term on the RHS also contains information about the scattering. However, in the current form of Eq. (2.53), the significance of the integral term is not immediately apparent. In order to develop the formalism, a transition amplitude is defined as:

$$K(\alpha\hat{\boldsymbol{u}}, k; \hat{\boldsymbol{r}}_0) = \int_D e^{-i\alpha\hat{\boldsymbol{u}} \cdot \boldsymbol{r'}} O(\boldsymbol{r'}) u(\boldsymbol{r'}, k; \hat{\boldsymbol{r}}_0) d\boldsymbol{r'}, \tag{2.54}$$

where α is an arbitrary constant and $\hat{\boldsymbol{u}}$ is an arbitrary vector. It can be proved easily that when $\alpha\hat{\boldsymbol{u}} = k\hat{\boldsymbol{r}}$, $K(\alpha\hat{\boldsymbol{u}}, k; \hat{\boldsymbol{r}}_0) = f(\hat{\boldsymbol{r}}, k; \hat{\boldsymbol{r}}_0)$. For further derivation, it is also necessary to introduce the eigenfunction expansion of the Green's function [38]:

$$G(\boldsymbol{r}, k; \boldsymbol{r'}) = -\frac{1}{8\pi^3} \int_{-\infty}^{\infty} \frac{e^{i\alpha\hat{\boldsymbol{u}}}(\boldsymbol{r} - \boldsymbol{r'})}{k^2 - \alpha^2 + i\xi} d\alpha, \tag{2.55}$$

where ξ is introduced to avoid singularity. Substituting Eq. (2.55) into Eq. (2.54), we

can get

$$K(k\hat{\boldsymbol{r}}, k; \hat{\boldsymbol{r}}_0) = \hat{O}(k(\hat{\boldsymbol{r}} - \hat{\boldsymbol{r}}_0)) + \frac{k^2}{8\pi^3} \int_{-\infty}^{\infty} d\alpha \frac{\hat{O}(k\hat{\boldsymbol{r}} - \alpha\hat{\boldsymbol{u}}) K(\alpha\hat{\boldsymbol{u}}, k; \hat{\boldsymbol{r}}_0)}{k^2 - \alpha^2 + i\xi}, \tag{2.56}$$

or equivalently,

$$f(\hat{\boldsymbol{r}}, k; \hat{\boldsymbol{r}}_0) = \hat{O}(k(\hat{\boldsymbol{r}} - \hat{\boldsymbol{r}}_0)) + \frac{k^2}{8\pi^3} \int_{-\infty}^{\infty} d\alpha \frac{\hat{O}(k\hat{\boldsymbol{r}} - \alpha\hat{\boldsymbol{u}}) K(\alpha\hat{\boldsymbol{u}}, k; \hat{\boldsymbol{r}}_0)}{k^2 - \alpha^2 + i\xi}. \tag{2.57}$$

As has been mentioned before, the scattering amplitude consists of the scattering amplitude under the Born approximation and an integration term. The spatial frequency of the first part of the right hand side of Eq. (2.57) is located inside the Ewald limit circle while the the second part depends on the integration over the whole K space. Thus, the spatial frequencies are higher than $2k$, which means that the far field scattering amplitude contains the information of geometric size less than $\lambda/2$. As a result, by considering the effects of multiple scattering, it is possible to achieve super resolution [53].

2.7.2 Linear Sampling Method

The Linear Sampling Method (LSM) which is defined by Colton and Kirsch [57] is the first non-iterative inverse scattering algorithm developed to reconstruct the support of the scatterers. This method is able to reconstruct the support of the scatterer without using any nonlinear optimisation method and prior knowledge of the geometry and physical properties of the scatterer [57]. The LSM utilises the assumption that the scattered field can only be generated at the boundary of the scatterer and cannot be produced for a point outside the scatterer, as shown in Fig. 2.10.

To start the derivation of the LSM, we shall recall the definition of the far-field operator F, which is defined as

$$(Fg)(\hat{\boldsymbol{r}}) = \int_{\mathbb{S}^2} f(\hat{\boldsymbol{r}}, k; \hat{\boldsymbol{r}}_0) g(\hat{\boldsymbol{r}}_0) ds(\hat{\boldsymbol{r}}_0). \tag{2.35 revisited}$$

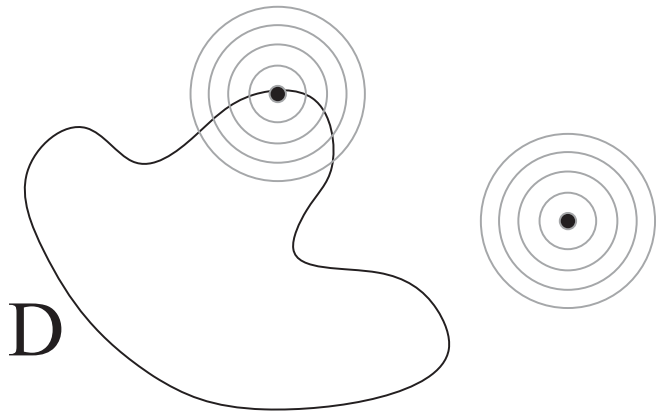


Figure 2.10: The LSM and the FM are based on the fact that the scattered field can only be generated at the boundary of the scatterer but cannot have originated at any point outside the scatterer.

Then, the LSM considers the far-field equation defined as

$$Fg_z = \Phi_\infty(\hat{\boldsymbol{r}}, k; \boldsymbol{z}), \tag{2.58}$$

where $z \in \Omega$ is a sampling point and $\Phi_\infty(\hat{\boldsymbol{r}}, k; \boldsymbol{z}) = e^{-ik\hat{\boldsymbol{r}}\cdot\boldsymbol{z}}$ is known as the steering function. It has been proven (see [66]) that

$$z \in D \iff \Phi_\infty(\cdot, k; \boldsymbol{z}) \in \mathcal{R}(F), \tag{2.59}$$

where $\mathcal{R}(F)$ denotes the range of the operator F. With these premises, according to [46], the theorem that is usually given to describe the approximate solution of the Eq. (2.58) is as follows.

- if $z \in D$, then for every $\varepsilon > 0$, there exists a solution g_z^ε that

$$||Fg_z^\varepsilon(\cdot) - \Phi_\infty(\cdot, k; \boldsymbol{z})||_{L^2(\Omega)} < \varepsilon; \tag{2.60}$$

and

$$\lim_{z\to\partial D} ||g_z^\varepsilon||_{L^2(\Omega)} = \infty, \tag{2.61}$$

$$\lim_{z\to\partial D} ||v_{g_z^\varepsilon}||_{H^1(D)} = \infty, \tag{2.62}$$

where $v_{g_z^\varepsilon}$ is the Herglotz wavefunction with density g_z^ε.

- if $z \in \mathbb{R}^2 \backslash \bar{D}$, then for every $\varepsilon > 0$ and $\delta > 0$, there exists a solution g_z^ε that

$$||Fg_z^{\varepsilon,\delta}(\cdot) - \Phi_\infty(\cdot, k; \boldsymbol{z})||_{L^2(\Omega)} < \varepsilon + \delta; \tag{2.63}$$

and

$$\lim_{\delta \to 0} ||g_z^{\varepsilon,\delta}||_{L^2(\Omega)} = \infty, \tag{2.64}$$

$$\lim_{\delta \to 0} ||v_{g_z^{\varepsilon,\delta}}||_{H^1(D)} = \infty, \tag{2.65}$$

where $v_{g_z^{\varepsilon,\delta}}$ is the Herglotz wavefunction with density $g_z^{\varepsilon,\delta}$.

After obtaining the above results, it is clear that the behaviour of the $||g_z||_{L^2(\Omega)}$ can be used to reconstruct the support of the object D. The common method is to solve the far-field equation $Fg_z = \Phi_\infty(\hat{\boldsymbol{r}}, k; \boldsymbol{z})$ by applying a regularization technique at first, e.g. Tikhonov-Morozov regularization [67], and then, using $\mathcal{I}(z) = 1/||g_z||_{L^2(\Omega)}$ as an indicator function to reconstruct the support of the object D.

2.7.3 Factorization Method

The Linear Sampling Method offers a non-iterative method for fast and accurate reconstruction of the shape of an obstacle. One significant challenge with the LSM is that the regularized results of the far-field equation do not converge when the noise in the data approaches zero. The motivation of the introduction of the Factorization Method by Kirsch is to modify the far-field equation to avoid the convergence problem. According to Eq. (2.37), a factorization of the Operator F can be derived in the form

$$F = H^* S H, \tag{2.66}$$

where $H : L^2(\mathbb{S}^2) \to L^2(\partial D)$ is the the Herglotz operator, $H^* : L^2(\partial D) \to L^2(\mathbb{S}^2)$ is the radiation operator of H and $S : L^2(\partial D) \to L^2(\partial D)$ is the interaction operator. This

factorization is the basis of the Factorization Method and is responsible for its name. Based on this factorization, it has been proven in [66] that instead of interrogating the range of F, a higher quality image can be formed by interrogating the range of H. In particular, Kirsch [68] has demonstrated that the range of H coincides with the range of $(F^*F)^{\frac{1}{4}}$. Therefore, the FM replaces the far-field operator F in the Eq. (2.58) by the operator $(F^*F)^{\frac{1}{4}}$, and then, the far-field equation becomes

$$(F^*F)^{\frac{1}{4}} g = \Phi_\infty. \tag{2.67}$$

It can be shown that the Eq. (2.67) has a solution if and only if $z \in D$, see Kirsch et al [37] for a detailed derivation. Further, $z \in \mathbb{R}^2$ belongs to D if and only if

$$\sum_{i=1}^{\infty} \frac{1}{|\sigma_i|} |\langle \Phi_\infty(\hat{\boldsymbol{r}}, z), \varphi_i \rangle_{L^2}|^2 < \infty, \tag{2.68}$$

where $\{\sigma_i, \varphi_i, \hat{\varphi}_i\}_1^\infty$ is the singular system of F. Eq. (2.68) is also called the Picard's criterion. By utilizing the behaviour of the Picard's criterion, an indicator function can be yielded as

$$FM(z) = \frac{1}{\sum_{i=1}^{\infty} \frac{1}{|\sigma_i|} |\langle \Phi_\infty(\hat{\boldsymbol{r}}, z), \varphi_i \rangle_{L^2}|^2}. \tag{2.69}$$

As a result, if a point z belongs to D, the value of Eq. (2.69) will be non-zero but will be zero otherwise [37]. After applying the indicator function through the whole grid of the target region, a scalar image can be reconstructed and the object is represented by non-zero points.

In this thesis, the FM is implemented in the frequency domain, especially at the central frequency of the ultrasound, and the spectral data $\boldsymbol{F}(w)$ of the far-field operator, which is also called the multistatic response matrix, is used for the calculation of the FM. The multistatic response matrix $\boldsymbol{F}(w)$ is actually built from the recorded FMC data using fast Fourier transforms (FFTs) at the central frequency, w [66]. By assuming a linear array containing N elements, the calculation process of the multistatic response matrix in this thesis is as follows: Firstly, after the acquisition of the FMC data, an $N \times N$ matrix is

provided, whose (m,n)th element is actually the recorded time-domain signal from mth transmitter to nth receiver, where $1 \leqslant m \leqslant N$ and $1 \leqslant n \leqslant N$; then, the FFT of each element in this $N \times N$ matrix is calculated; after that, the complex value of the FFT result at the central frequency w of (m,n)th element is used as the (m,n)th entry of the $\boldsymbol{F}(w)$. For other time domain implementations of the related sampling methods the reader is referred to [60, 69–71] for details.

Chapter 3

Eliminating backwall effects for near backwall defect imaging

3.1 Introduction

Having covered the underlying theory of ultrasonic array imaging, we are now focusing on the practical application of using the ultrasonic array to assess the size and type of fatigue cracks or stress corrosion cracks in this chapter. As mentioned in Chapter 1, these cracks are commonly found near inaccessible interior surfaces, referred to here as 'backwalls', and are of concern in safety-critical components under severe working environment (high pressure or high temperature) or cyclic loading, for example nozzles, piping components and vessel welds [72].

Usually when inspecting for near backwall defects, the array has to be placed on the frontwall to conduct through-wall detection of the defect near the backwall. In these cases, the presence of the backwall brings a strongly reflecting planar interface which will introduce strong specular reflection into the captured FMC data. As a result, for typical FMC data, the signal from the defect and the backwall reflection always overlap in both time and frequency domain, thus, they are hard to separate via the existing signal processing techniques, for example deconvolution techniques [73]. The presence of the strong backwall reflection will introduce strong artefacts that makes imaging of the defect difficult; these will be referred to as backwall effects throughout this thesis. As a

result, the removal or elimination of the backwall effects is of great importance to improve the sensitivity and effectiveness of ultrasonic array in imaging and characterising the near backwall defects.

Recently, the use of ultrasonic arrays to evaluate near backwall defects has attracted a lot of attention [28,31,55,74]. In response to the backwall effects problem, J. Zhang et al. [28] have developed a method which separates the reference backwall reflection from non-overlapping signals (see Fig. 3.3) and then propagates the reference backwall reflection to create a backwall reflection for overlapping signals. After that, the extraction of the defect signal can be achieved by a simple subtraction. The implementation of this method needs a prior TFM image to achieve the knowledge of the defect location and backwall location, and in order to minimise the error, the array should be aligned with the defect as much as possible. These prerequisites may limit the application of this method in real applications. E. Iakovleva et al. [74] also have developed the Echo Transformation Method (ETM) to allow the prediction and filtering of the backwall effects in the TFM images. However, this technique needs to analyse the propagation models of the longitudinal wave in order to recognise and predict the performance of the backwall reflection in the transverse mode TFM image, or the other way around. In some cases [31, 55] the removal of the specular component is achieved by angling the incoming beam such that the specular reflection does not return to the array. The issue is that this generally requires the use of wedges, restricts the illumination angle and makes longer path lengths, increasing attenuation, and therefore this approach is not pursued in this thesis.

In this chapter, new techniques which allow convenient elimination of backwall effects are presented. Two imaging algorithms are used, the HSTFM and the FM, to image the near backwall defects. A detailed introduction to the developed methods which eliminate the backwall effects caused by the backwall reflection is provided in this chapter. In this chapter, we also examine the effectiveness of the developed methods using simulation data. Furthermore, the performance of the imaging algorithms together with the backwall elimination methods are analysed through experiments.

The work in this chapter has been submitted to The Journal of the Acoustical Society of America [P2].

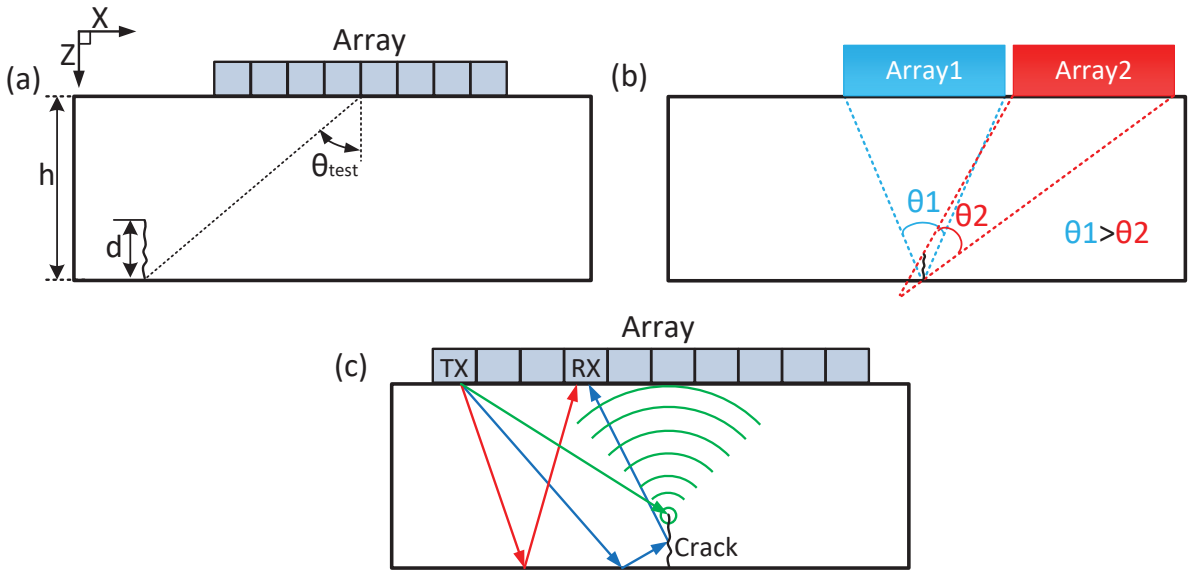


Figure 3.1: (a) Schematic showing the inspection of a component containing a surface-breaking crack. (b) Schematic showing the difference in angle of view between two different imaging setups. (c) Schematic showing the ray paths of different signal components when the defect is located directly beneath the array; note that the red ray path represents the backwall reflection, the blue ray path represents the 'half-skip' reflection and the green ray path represents the tip diffraction.

3.2 Imaging setup

In this chapter, we focus on the problem of subsurface imaging of the near surface defects, especially the surface-breaking cracks. Consider a sample which has two flat parallel surfaces, a thickness of h and a surface-breaking crack located at the lower surface, as shown in 3.1(a). An ultrasonic array is attached to the remote side to perform the subsurface imaging. The depth d of the crack is the vertical distance between the crack tip and the backwall. The line joining the centre of the array to the point where the crack connects to the backwall makes an angle of θ_{test} with the vertical. Thus, the horizontal distance between the point that the crack initiates at and the centre of the array can be calculated by $h \times \tan\theta_{test}$.

In fact, the angle θ_{test} not only determines the relative position between the crack and the array, but also relates to the available viewing aperture or the angle of view. In Fig. 3.1(b), we compare the angle of view difference between two different imaging configurations based on the same array and the same component, one with the crack located directly beneath the array ($\theta_{test} = 0°$), another one with the crack located a distance from the array

(usually, $\theta_{test} = 30°$ or $45°$). It is obvious that the biggest angle of view can be achieved when $\theta_{test} = 0°$. In some papers, for example [31], the array was placed at a distance from the crack ($\theta_{test} = 45°$), so that the backwall reflection can be easily separated from the defect signal. However, this method will not only result in a small viewing angle but also the longer ray path and increasing attenuation. In the case of limited aperture, according to the work done by T. D. Hutt, a small reduction in the angle of view will dramatically degrade the images reconstructed by the FM and TFM [75]. As a result, in order to achieve the biggest angle of view and improve the signal strength, the incident angle θ_{test} was set to be zero in this thesis.

Assuming a zero incident angle, since the planar backwall is a very strong reflector for the ultrasound, a typical recorded signal during detection will contain three components: the backwall reflection, the 'half-skip' reflection and the tip diffraction, as shown in Fig. 3.1(c). Among the three components, the 'half-skip' reflection and the tip diffraction will be referred to as the defect signal in this thesis as they contain information about the defect. The backwall reflection has a much stronger energy than the defect signal as the backwall reflection is the direct specular reflection from the array to the backwall and back to the array, yet provides no information about the defect.

3.3 Eliminating backwall effects

3.3.1 Signal overlap problem

In a typical FMC dataset acquired based on the imaging configuration shown in Fig. 3.1(c), the defect signal and the backwall reflection often overlap in both the time and frequency domains. In order to visually study the overlap of the defect signal and the backwall reflection, we perform a numerical simulation using a finite element model which was created in Abaqus (Dassault Systemes Simulia Corp., Providence, RI) to approximate simulated array data. For simplicity, a 2D FE model is used to analyse this problem under the assumption that all the properties are uniform out of the plane. Here, as the shear wave and the mode conversions between the longitudinal and shear wave always arrive later than the longitudinal wave, and the derivation of the imaging algorithms are based

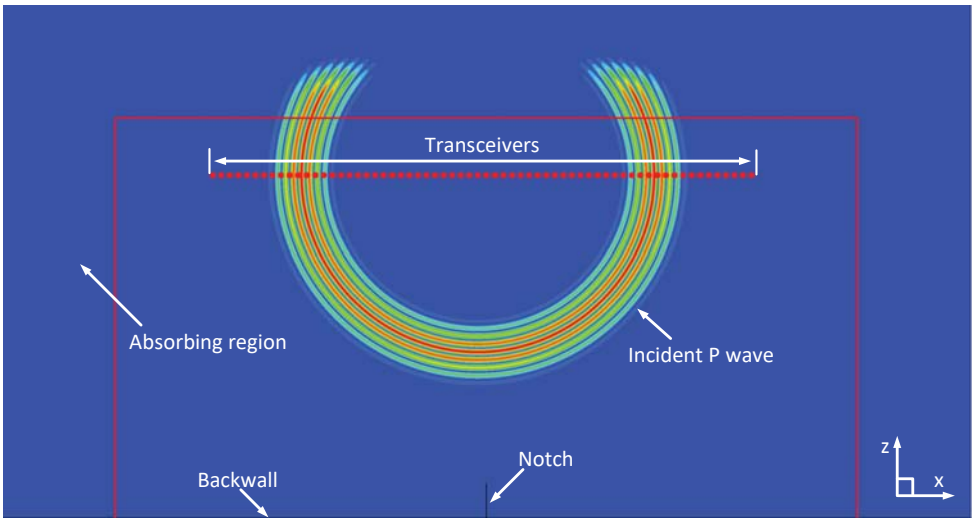


Figure 3.2: Snapshot of the FE model used for simulation in Abaqus (Dassault Systemes Simulia Corp., Providence, RI). The length of the notch is 2λ, the thickness of the component is 20λ and the distance between two transceivers of the array is 0.5λ. Frequency is 2MHz, giving a wavelength (λ) of 3mm.

on the acoustic waves which are a type of longitudinal wave, only a longitudinal wave was excited and recorded for simplicity [76]. The material used for simulation is isotropic steel with a density of $7700kg/m^3$, a Young's modulus of $195GPa$ and a Poisson ratio of 0.28. The element used in this model is the linear 2D plane strain element. The phased array has 64 elements and the wave generated by the array is a Hann windowed 5 cycle tone burst with a central frequency 2MHz. Thus, the wavelength λ of the longitudinal wave is about 3mm. To make this model more general, all of the geometric lengths are defined relative to the wavelength. Here, the length of the notch is 2λ, the thickness of the component is 20λ and the distance between two transceivers of the array is 0.5λ. Absorbing layers [77] were attached to the model to absorb any wave entering them, acting as 'reflectionless boundaries', to effectively model a small section of an infinite region. The notch is simulated by disconnecting nodes along the interface of adjacent elements, thus the width of the notch is zero. Fig. 3.2 shows a snapshot from the FE model used in Abaqus.

From the simulated FMC data from this model, we observed that in the case of detecting the near surface defect, it is easy for the backwall reflection and the defect signal to overlap with each other, and the overlap phenomenon happens in both time and frequency domains [28], as shown in Fig. 3.3. Additionally, from Fig. 3.3, we can also see that the

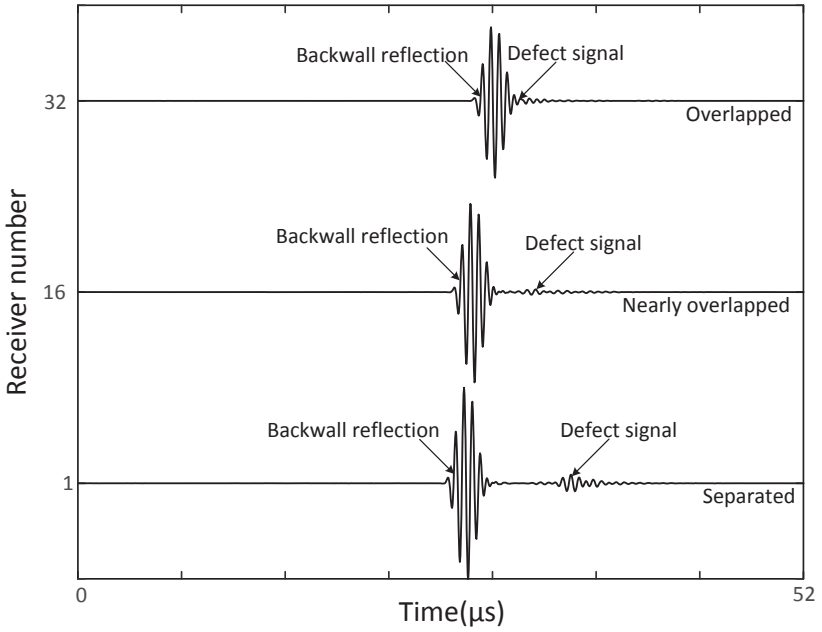


Figure 3.3: The time traces of three different elements based on simulated FMC data; note that the element 1 is used as the transmitter while all the elements used as receivers.

amplitude of the backwall reflection is always much stronger than the defect signal. These problems make the extraction of the defect signal challenging.

The overlap phenomenon will also seriously affect the imaging result. Fig. 3.4 shows the imaging results of HSTFM and FM based on the measured signal containing both the backwall reflection and the defect signal. From Fig. 3.4, it is clear that in all of the three images, the indication of the notch is masked by the strong indications of the backwall and artefacts introduced by the backwall reflection.

Thus, in order to get strong and clear indication of the notch through these imaging algorithms, the primary problem for imaging a near surface defect at $\theta_{test} = 0°$ is how to eliminate the effects introduced by the strong backwall reflection. In response, we have developed several methods to eliminate the backwall effects and to ensure a clear and strong indication of the notch, these methods will be described in detail below.

3.3.2 Backwall subtraction method

One possible way of the extracting the scattered field is by measuring the total field of a defect-free copy of the component which contains the defect; this method is referred

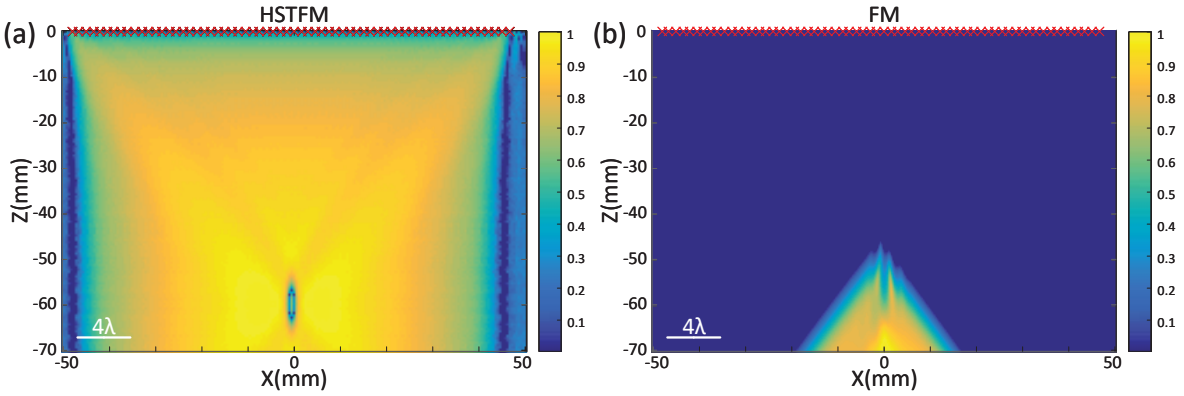


Figure 3.4: Results from setup shown in Fig. 3.2. (a) HSTFM and (b) FM images based on the overall signal. The red 'X' symbols at the top of the images represent the location of the transceivers and the amplitude is normalized to the maximum value in each image. The results here are from simulated data.

to as baseline subtraction in this thesis. The baseline subtraction is easy to be realized with numerical simulations, however, this method is not practical in real inspection as it is not possible to achieve a defect-free copy of the component. Another commonly used method is gating, that is to calculate the arrival time of the backwall reflection and set the corresponding sections of the measured signals to zero at these locations. Due to the complexity of the elasticity and the geometry, the arrival time is actually hard to accurately calculate in practical applications and an accurate calculation still needs a defect-free component to calibrate. The main disadvantage of a simple gating is that scattered signals which overlap with the backwall reflection will be lost. In the subsurface imaging of the surface-breaking cracks, the amplitude of the backwall reflection is much larger than the scattered signal and the signals commonly overlap with each other, as shown in Fig. 3.3. As many imaging algorithms (e.g. FM) are sensitive to the entirety of the scattered field, the loss of the information will strongly influence the image result and will typically introduce artefacts or shadows. Thus, gating is not the best solution for the removal of backwall reflection here.

We assume that the array used for detection has N element, thus, the acquired FMC data shall contain $N \times N$ time traces. The elements of this linear array are numbered from 1 to N. We denote the measured data with the ith element used as transmitter and the jth element used as receiver by $I(i, j)$, where $i = 1 \cdots N$ and $j = 1 \cdots N$. We can arrange the measured data into N different series based on $|i - j|$, i.e. the absolute difference between

the sender and receiver element number. Each $series\{k\}$ contains $N-k$ time traces:

$$\begin{aligned} series\{k\} &= \{I(l,l+k), 1 \le l \le N-k\} \\ &\cup \{I(l+k,l), 1 \le l \le N-k\}, \end{aligned} \tag{3.1}$$

where $k = 0 \cdots N-1$. By assuming that the upper and lower surfaces of the component are flat and parallel and the material is homogeneous, for the transmitter and receiver pairs with the same $|i-j|$ (element i used as transmitter and element j used as receiver), the ray paths of the backwall reflection will be the same while the ray paths of the scattered signal will be different(Fig. 3.5a). In other words, for element pairs of the same lateral separation, the length of ray paths of backwall reflections are identical for the case of two planar surfaces. That means these signals will have the same arrival time and amplitude of the backwall reflection but different arrival time and amplitude of the defect signal (Fig. 3.5b).

As the backwall reflection behaves in a well-defined manner, but the defect signal is much less correlated (Fig. 3.5b), the scattered signal can be regarded as the incoherent noise to the backwall reflection for this series of data. As a result, the backwall reflection $B(k)$ for $series\{k\}$ can be estimated:

$$B(k) = \frac{1}{2(N-k)} \sum_{i=1}^{N-k} (I(i,i+k) + I(i+k,i)), \tag{3.2}$$

where $i = 1 \cdots N$ and $k = 0 \cdots N-1$, i.e. by averaging the matched signals together to minimise the scattered components present. In this thesis, if not otherwise specified, the summation and averaging in Eq. (3.2) is implemented over the full time duration. Having obtained the backwall reflection of each series of data, the scattered signal can be extracted by subtracting this estimated backwall reflection from the total field.

$$S(i,j) = I(i,j) - B(|i-j|), \tag{3.3}$$

where $i = 1 \cdots N$ and $j = 1 \cdots N$. This method for removing the backwall reflection works for the components with flat, parallel surfaces, and homogeneous material. In theory it

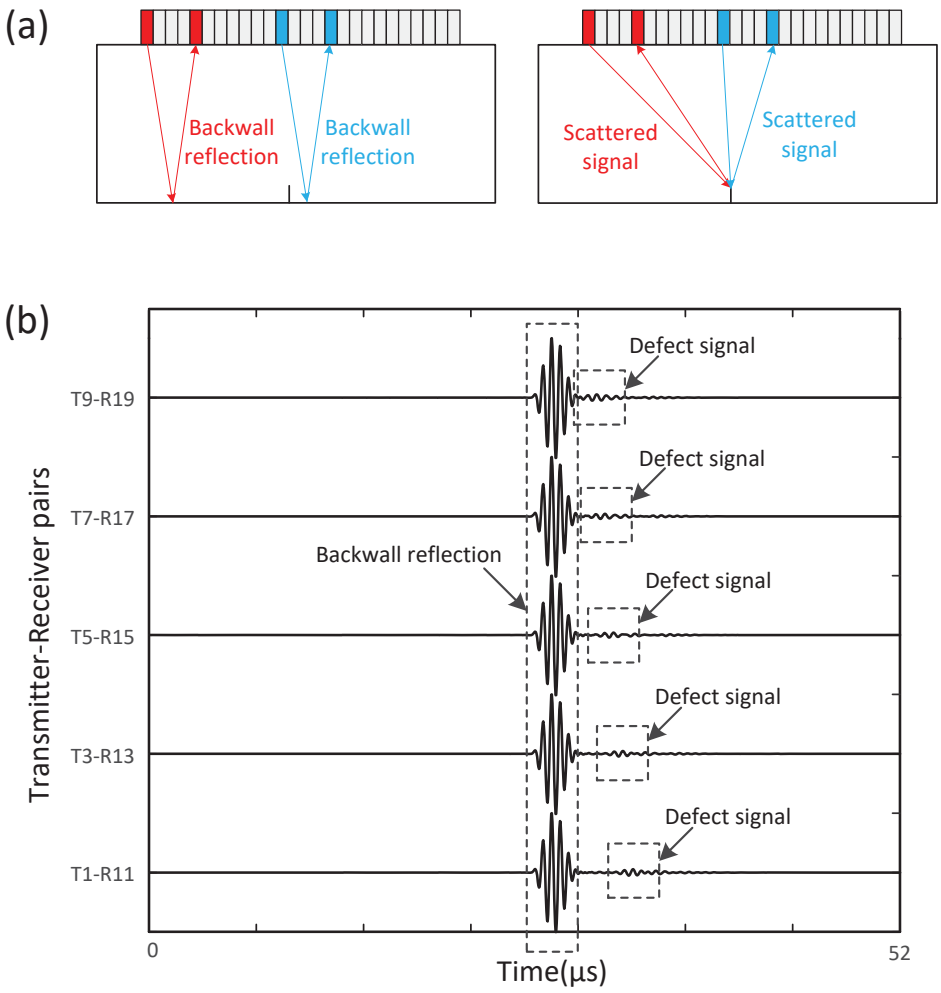


Figure 3.5: (a) Schematic showing the components of a received signal; (b) The time traces of different transmitter-receiver pairs with same $|i-j|$ based on simulated array data for the configuration in Fig. 3.1 when h=60mm, d=6mm and $\theta_{test} = 0°$.

may be possible to achieve the same approach with more complex geometries, provided enough averages of each distinct backwall component can be obtained. In practice it is likely that the case considered here is the only one where this is possible. This method is called the FMC subtraction in this thesis. One problem for this method is that with the bigger k, the $series\{k\}$ will have fewer time traces, which will influence the averaging in Eq. (3.2). This will result in an inaccurate estimation of the backwall reflection, so some residue of the backwall reflection will remain in $S(i,j)$ after subtraction. Actually, for real inspections, even using baseline subtraction to remove the backwall reflection will introduce some residue as a small difference in phase and amplitude will always exist between the measured data.

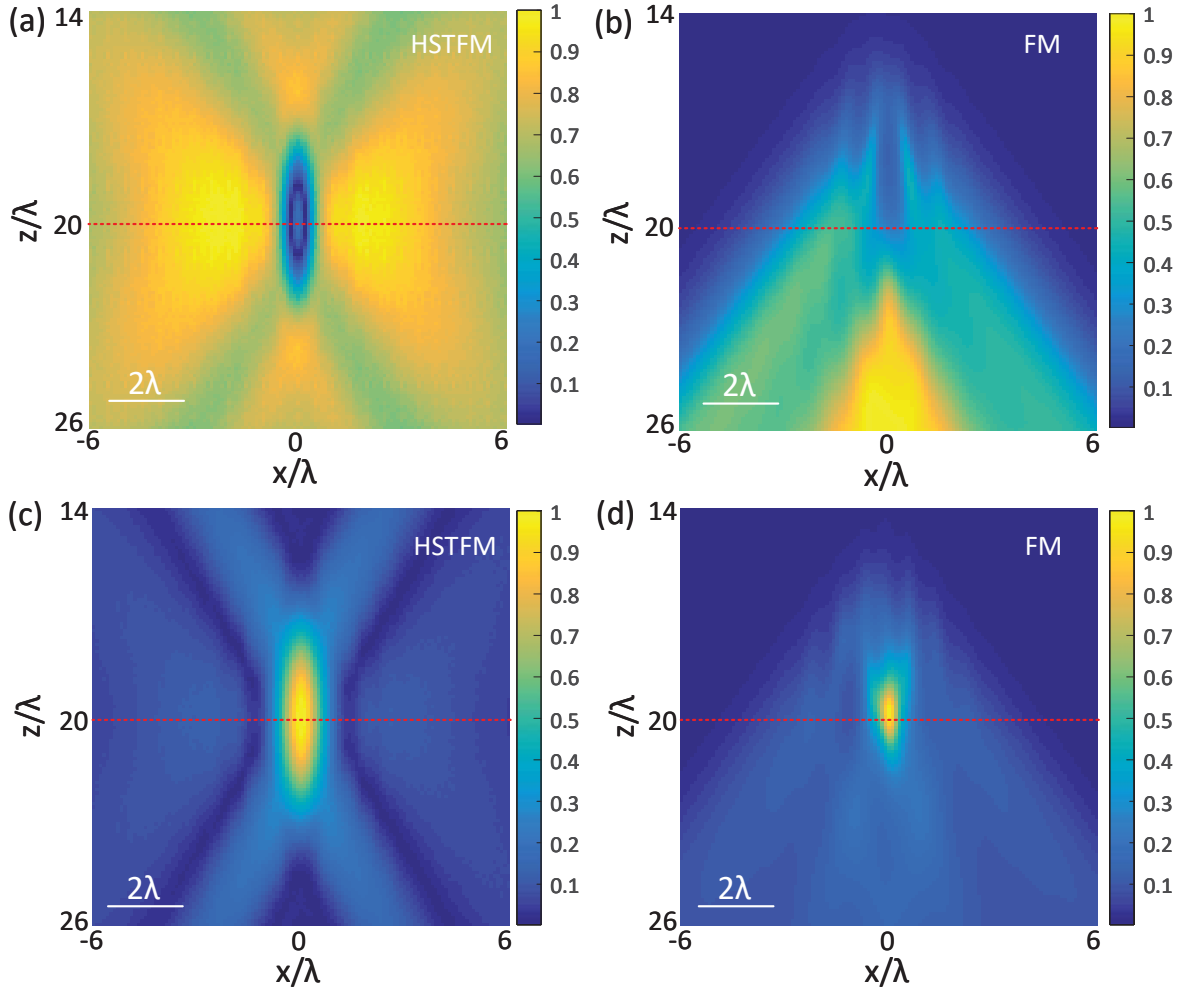


Figure 3.6: Results from setup shown in Fig. 3.2. (a) HSTFM and (b) FM images, all based on the original signal. (c) HSTFM and (d) FM images, all based on the signal after FMC subtraction. The images are normalized to the maximum value in each image. Note that the red dotted lines in the images are used to represent the location of backwall. The results here are from simulated data.

Fig. 3.6 compares different imaging algorithms based on the signal before and after FMC subtraction. Fig. 3.6 (a) and (b) are the HSTFM and FM results based on the original FMC data. In all of these images, it is clear that the strong indication introduced by the backwall totally masks the indication of the notch. Fig. 3.6 (c) and(d) are the HSTFM and FM results based on the FMC data after the FMC subtraction. Obviously, by using the FMC subtraction, there are significant improvements in the imaging results. For the HSTFM, the FMC subtraction shows excellent performance as the imaging results after FMC subtraction have very strong and clear indications of the notch and the residue backwall reflections only introduce some uniform background noise which can be simply

eliminated through a filter. For the FM, the FMC subtraction also helps to achieve a sharp and strong indication of the notch (see Fig. 3.6(d)), which means the majority of the backwall reflection has been removed. However, as the FM imaging algorithm is more sensitive to noise than the HSTFM [75], the residual backwall reflection brings more obvious artefacts to the FM image compared to the HSTFM. These artefacts are the 'side bars' near the strong indication of the notch in Fig. 3.6(d), which may raise the risk of falsely judging the type of the defect. Note that since FMC subtraction is a preprocessing method which operates on the data itself, rather than being incorporated into the algorithm, this method is theoretically suitable for any imaging algorithm which utilises the scattered signal to reconstruct the defect.

3.3.3 Weighting function method for HSTFM

Apart for the FMC subtraction, a specific method for the HSTFM has also been developed. This method is called the weighting function in this thesis. The weighting function method is inspired by the work done by P. Huthwaite in [78], where it is shown that the subtraction of the incident wave is unnecessary when imaging using Diffraction Tomography (DT) as the effects introduced by the incident wave will vanish automatically in the DT algorithm. Also, in [79], F. Simonetti et al. have found that there is a linear mapping between Beamforming (BF) and DT. As TFM or HSTFM is actually a BF algorithm, the results in [78] can be directly applied to HSTFM.

Since HSTFM only considers the 'half-skip' ray paths which are reflected on the backwall once, either before or after interacting with the defect, an equivalent ray path of the 'half-skip' ray path can be derived as in Fig. 2.8(c). Specifically, the equivalent ray paths of the backwall reflection and the 'half-skip' reflection considered in the HSTFM are shown in Fig. 3.7(a) and (b). We neglect the tip diffraction here as the energy of the tip diffraction is too weak compared to the 'half-skip' reflection and backwall reflection. If we define Δ_θ as the angle between the incident direction and the receiving direction in the equivalent model, then all the equivalent ray paths of the backwall reflections will have the same angle $\Delta_\theta = 0°$, see Fig. 3.7(a). At the same time, from the Fig. 3.7(b), the Δ_θ will vary from point to point when considering the 'half-skip' reflection and in this case, Δ_θ can

never be 0° or 180°.

Based on this phenomenon, a weighting function, which can be used as a filter to eliminate the backwall effects, has been introduced as:

$$f(\boldsymbol{x_r}, z; \boldsymbol{x_t}) = |sin(\Delta_\theta)| \tag{3.4}$$

where $\boldsymbol{x_t}$ is the location of the transmitter, $\boldsymbol{x_r}$ is the location of the receiver and Δ_θ is the angle between the forward direction from the real array and the backward direction to the mirrored array, as shown in Fig. 3.7(a) and (b). It is obvious that the value of this weighting function will tend to 0 if Δ_θ is close to 0° or 180°. Then, this weighting function is integrated in Eq. (2.51) as:

$$\begin{aligned} I_{HSTFM}(z) &= \int_{\Gamma_i}\int_{\Gamma_i} f(\boldsymbol{x_r}, z; \boldsymbol{x_t}) U^S(\boldsymbol{x_r}, \frac{|\boldsymbol{x_t} - \boldsymbol{z}| + |\boldsymbol{x_r} - \boldsymbol{z_m}|}{c_0}; \boldsymbol{x_t}) ds(\boldsymbol{x_r}) ds(\boldsymbol{x_t}) \\ &= \sum_{t,r=1}^{N} f(\boldsymbol{x_r}, z; \boldsymbol{x_t}) U^S(\boldsymbol{x_r}, \frac{|\boldsymbol{x_t} - \boldsymbol{z}| + |\boldsymbol{x_r} - \boldsymbol{z_m}|}{c_0}; \boldsymbol{x_t}), \end{aligned} \tag{3.5}$$

where Γ_i is the surface where the array located, $\boldsymbol{x_t} \in \Gamma_i$ is the location of the transmitter, $\boldsymbol{x_r} \in \Gamma_i$ is the location of the receiver and $U^S(\boldsymbol{x_r}, t; \boldsymbol{x_t})$ denotes the time domain scattered data from a transmitter located at $\boldsymbol{x_t}$ to a receiver located at $\boldsymbol{x_r}$. Fig. 3.8(a) and Fig. 3.8(b) are the HSTFM images based on the original FMC data without and with the weighting function, respectively.

From Fig. 3.8, it is obvious that by using the conventional HSTFM together with the weighting function, the effects introduced by the backwall reflection vanish automatically, which means the weighting function shows an excellent ability to eliminate the backwall effects. As a result, a good indication of the notch can be imaged without the backwall subtraction when using the HSTFM with the weighting function. Using the weighting function to eliminate the backwall effects will be called the 'weighting function method' through out this thesis.

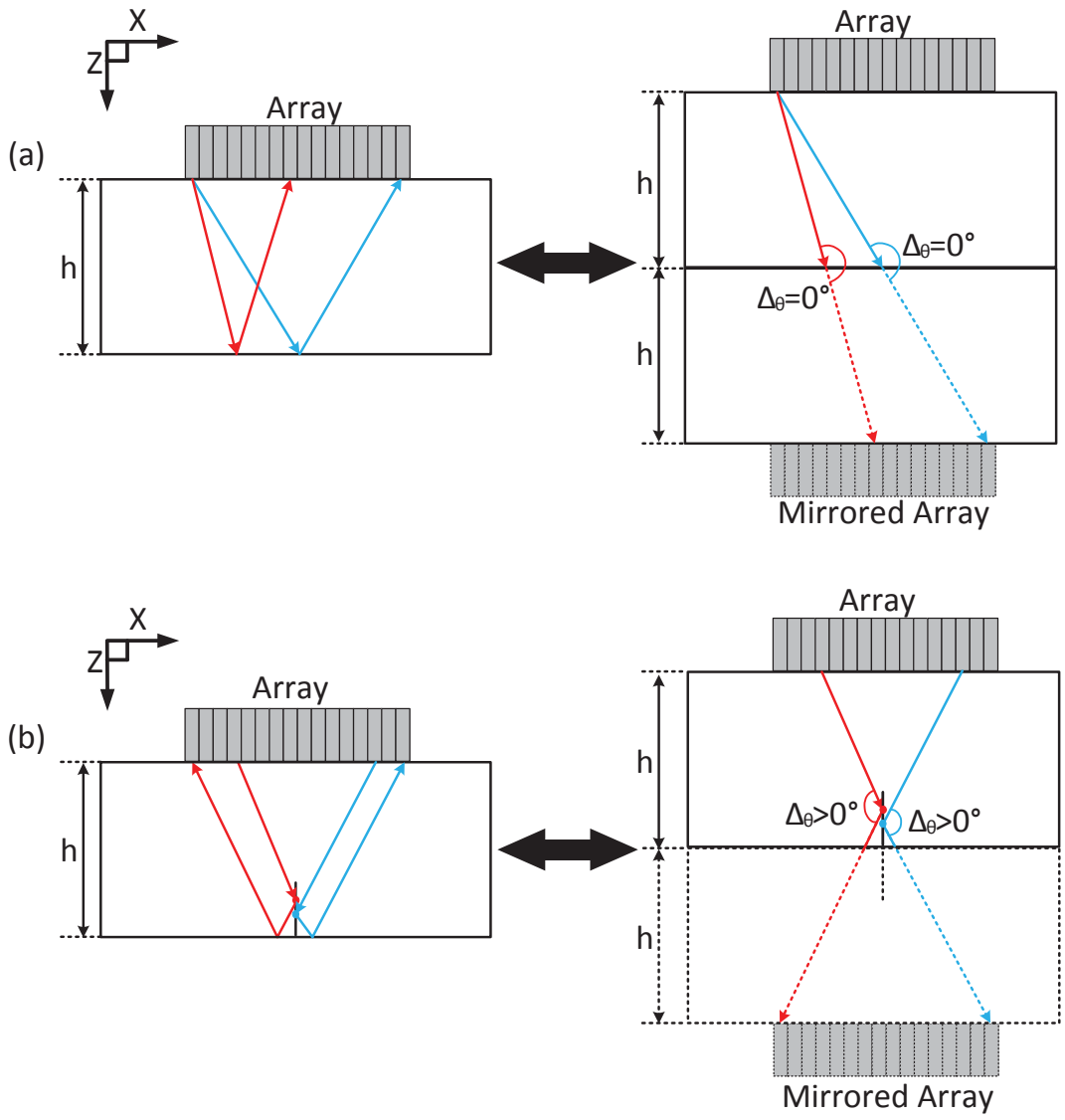


Figure 3.7: (a) Equivalent ray path of the backwall reflection considered in the HSTFM, (b) Equivalent ray path of the 'half-skip' reflection considered in the HSTFM.

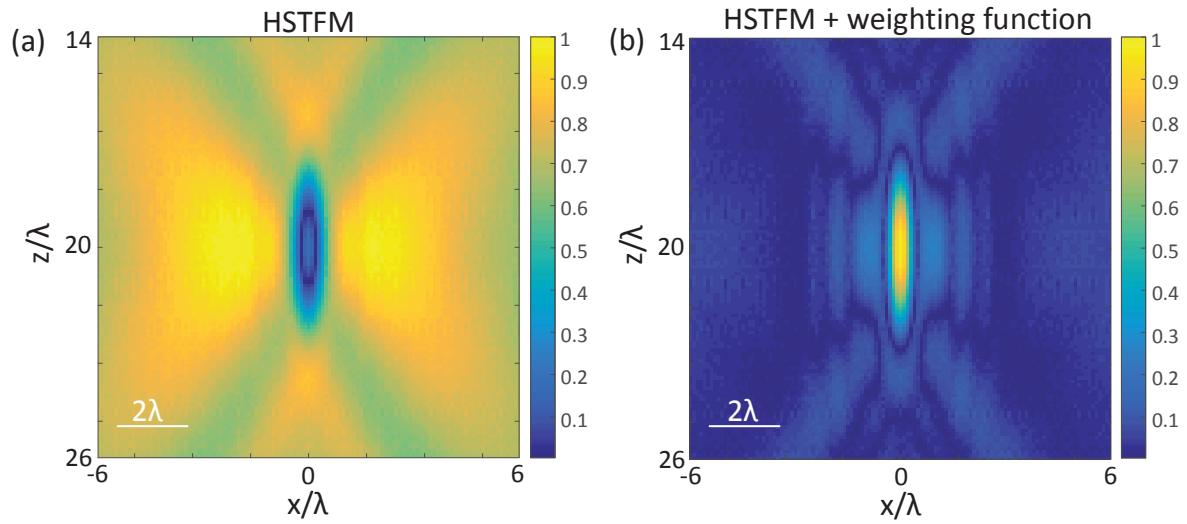


Figure 3.8: Results from setup shown in Fig. 3.2. (a) Conventional HSTFM image based on the overall signal, (b) Conventional HSTFM with the weighting function image based on the overall signal. The images were normalized to the maximum value in each image. The results here were from simulated data.

3.3.4 Truncation method for FM

If we observe the indicator function of the FM algorithm (Eq. (2.69)), it can be found that the calculation of the FM image heavily depends on the singular values and the corresponding eigenvectors of the far-field operator. It has been proved that the singular values and the relevant eigenvectors of the far-field operator are linked to the scatterers [80], that means by using different singular values, the FM is able to reconstruct different scatterers. Based on this theory, an imaging experiment has been conducted using different numbers of singular values for the calculation. In these cases, a threshold criterion can be used to determine how many singular values will be used for imaging.

As shown in Fig. 3.9, 10% of the maximum means that the calculation of the FM algorithm will only use the singular values whose amplitudes are bigger than 10% of the maximum value at each frequency. Three threshold values have been set, 80%, 10% and 1%, and the imaging results of the FM algorithm based on these 3 criteria are shown in Fig 3.10.

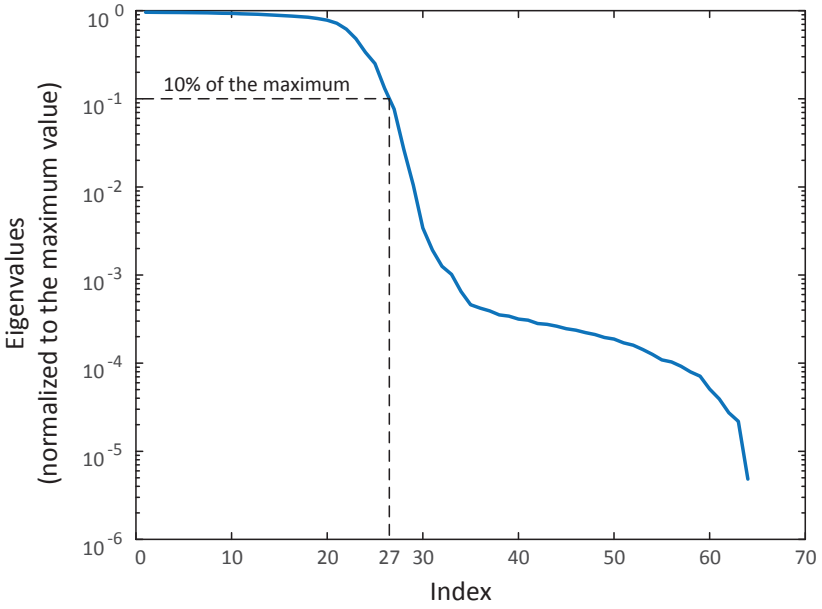


Figure 3.9: Singular values spectrum for the simulated FMC data at 2MHz.

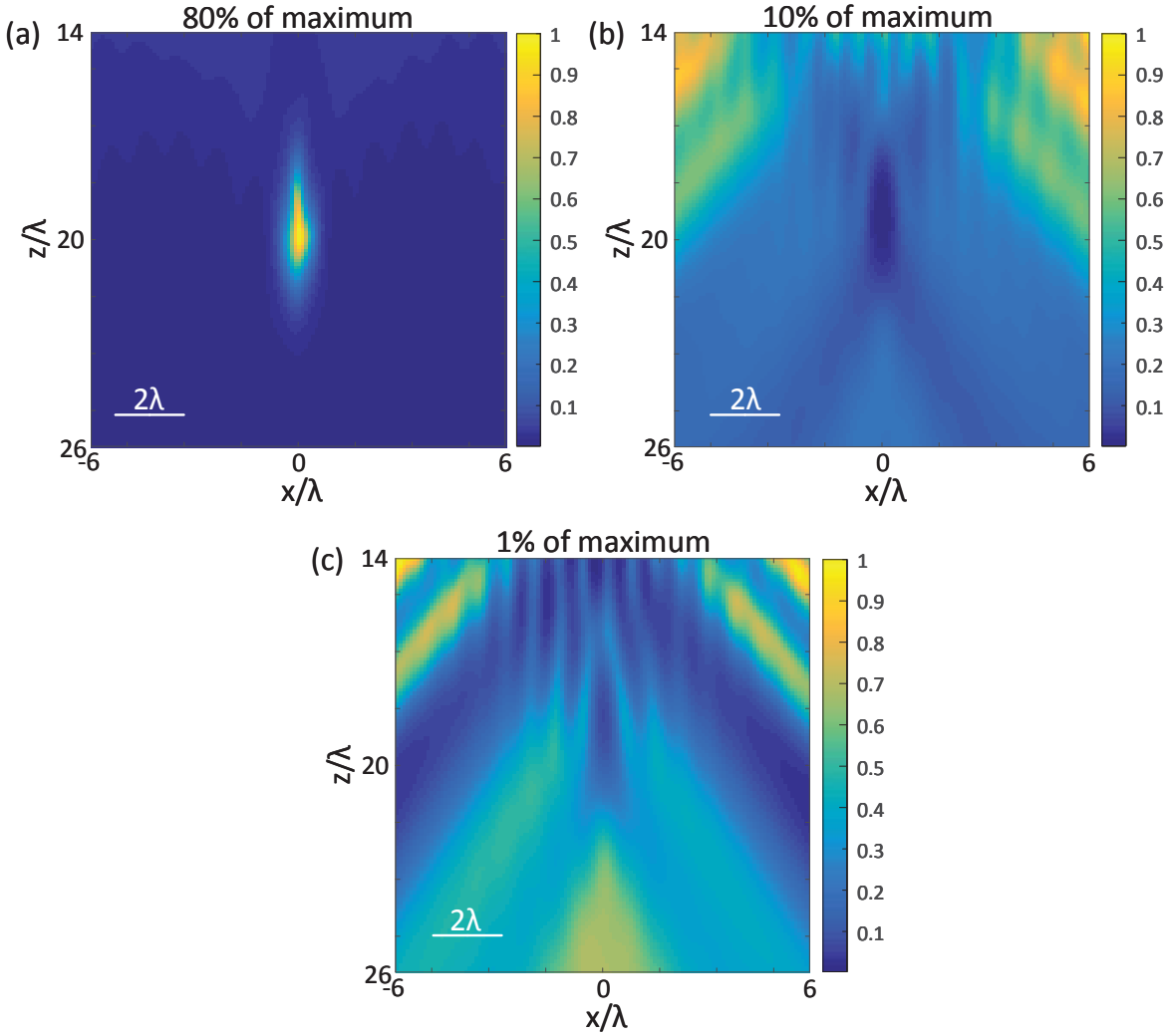


Figure 3.10: Results from setup shown in Fig. 3.2. (a) FM image using the 80% criterion, (b) FM image using the 10% criterion, (c) FM image using the 1% criterion. The images were normalized to the maximum value in each image. The results here are from simulated data.

From Fig. 3.10(a), it is clear that the image only contains a strong indication of the notch, and there are no artefacts introduced by the backwall reflection near the indication of the notch. By using more singular values (10% of maximum), the backwall effects start to dominate the behaviour of the image, see Fig. 3.10(b). If most of the singular values are used (1% of maximum), the indication of the notch is totally masked by the backwall effects, see Fig. 3.10(c). From these images, it indicates that the most significant singular values (80% of the maximum) are linked to the notch and the information brought by the backwall reflections are encoded in the smaller singular values. Here, based on the imaging results, a criterion of 80% of the maximum value at each frequency was found to be a good threshold for the FM algorithm to eliminate the backwall effects, indicating that the backwall reflection is not included in the FM image when the small singular values are truncated. As this method contains a truncation of the small singular values, this method is called the 'truncation method' throughout this thesis. Note that the threshold criterion depends on the type of defect and the structure of the component, so the threshold criterion should be tuned for different inspection scenarios.

One problem of this method is that it ignores the small singular values, thus, it leads to the loss of information. In the case of limited-view imaging, a common way to compensate for the loss of information is to increase the available aperture [81]. In [75], with the purpose of achieving a more detailed image in the case of limited-view, T. D. Hutt has developed a method which utilises the backwall to provide additional views. This method essentially increases the available aperture for a specific array, however, this method is not able to provide good results if the defect is located close to the backwall. Inspired by this, a new method has been developed to increase the available aperture in the case of imaging the near backwall defects, especially the surface-breaking cracks. Based on the derivations of the HSTFM and the weighting function for the HSTFM, it is obvious that the two models in Fig. 3.11 are related.

Here, for the model shown in Fig. 3.11(a), we define the tip diffraction as u_t^∞, the 'half-skip' reflection as u_h^∞ and the overall defect signal as u^∞, while for the model shown in Fig. 3.11(b), we define the forward scattering from array1 to array2 as u_{12}^∞, the forward scattering from array2 to array1 as u_{21}^∞, the backward scattering from array1 back to array1 as u_{11}^∞ and the backward scattering from array2 back to array2 as u_{22}^∞ . The ray

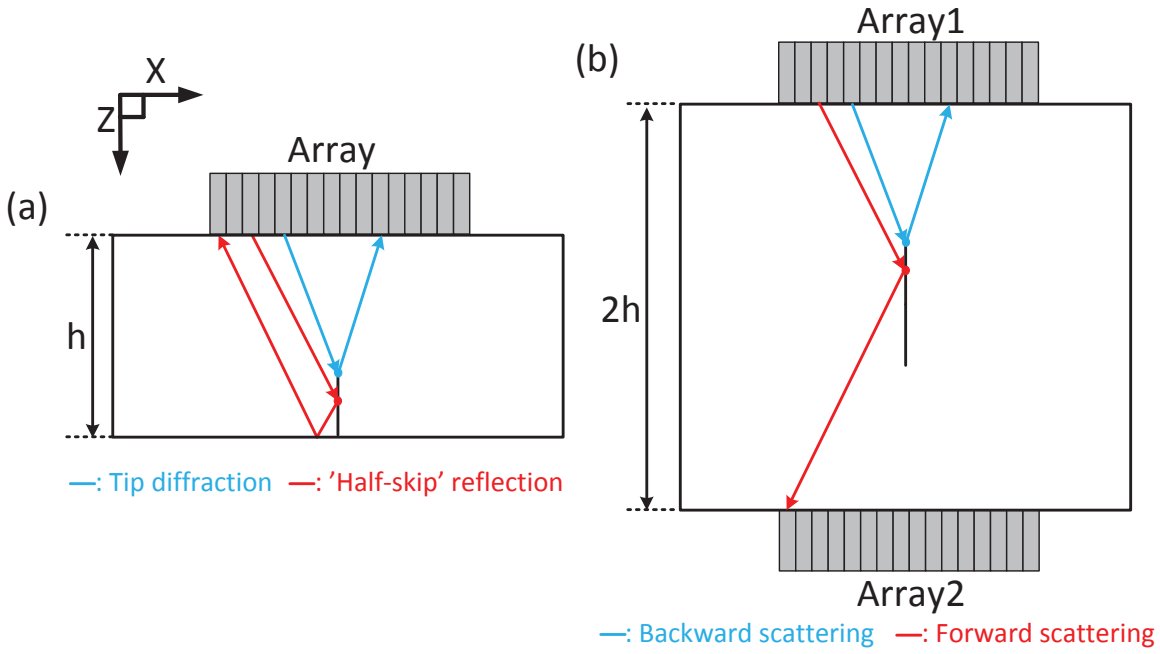


Figure 3.11: Two related models: (a) The configuration of imaging the near surface notch using an array placed on the remote surface, (b) The related two array configuration with the notch located in the middle of the material. The depth of the notch in (b) is twice the depth of the notch in (a).

path of the tip diffraction based on the model shown in Fig. 3.11(a) is actually equivalent to the ray path of the backward scattering from array1 back to array1 based on the model shown in Fig. 3.11(b), similarly, the ray path of the 'half-skip' reflection based on the model shown in Fig. 3.11(a) is actually equivalent to the ray path of the forward scattering from array1 to array2 based on the model shown in Fig. 3.11(b). Because of the symmetry of the model shown in Fig. 3.11(b) and the principle of reciprocity, it is clear that $u_{11}^{\infty} = u_{22}^{\infty}$ and $u_{12}^{\infty} = u_{21}^{\infty}$. Based on all these facts, we have

$$u^{\infty} = u_t^{\infty} + u_h^{\infty}, \tag{3.6}$$

$$u_t^{\infty} = u_{11}^{\infty} = u_{22}^{\infty}, \tag{3.7}$$

$$u_h^{\infty} = u_{12}^{\infty} = u_{21}^{\infty}. \tag{3.8}$$

As the energy of the 'half-skip' reflection and the energy of the specular reflection are

much larger than the energy of the tip diffraction, it is clear that

$$u_h^\infty \gg u_t^\infty, \quad u_t^\infty \approx 0, \tag{3.9}$$

$$u_{12}^\infty \gg u_{11}^\infty, \quad u_{11}^\infty \approx 0. \tag{3.10}$$

Then, Eq. (3.6) becomes

$$u^\infty \approx u_{12}^\infty, \quad u_{12}^\infty = u_{21}^\infty = u_h^\infty. \tag{3.11}$$

Thus, the full data-set u_{full}^∞ which can be recorded based on the model shown in Fig. 3.11(b) becomes

$$\begin{aligned} u_{full}^\infty &= \begin{pmatrix} u_{11}^\infty & u_{12}^\infty \\ u_{21}^\infty & u_{22}^\infty \end{pmatrix} \\ &\approx \begin{pmatrix} 0 & u^\infty \\ u^\infty & 0 \end{pmatrix} \end{aligned} \tag{3.12}$$

Through Eq. (3.12), we can reconstruct the full data-set u_{full}^∞ based on the model shown in Fig. 3.11(b) through the defect signal recorded in the model shown in Fig. 3.11(a). As a result, the available imaging aperture is essentially increased by using the reconstructed u_{full}^∞ and the relevant imaging configuration (Fig. 3.11(b)) for the FM algorithm. This method is called the mirror enhancement throughout this thesis and is used to compensate for some of the lost information when the truncation method is used with the FM algorithm to eliminate the backwall effects for near backwall defects. T. Hutt et al. [75,81] have developed a method that uses a modified Green's function in the calculation of the FM image to utilise the effect of mirror, however, their method has shown a poor performance for near backwall defects. The effect of the mirror enhancement is shown in Fig. 3.12.

From Fig. 3.12, it is clear that by using the FM algorithm together with the truncation method and the mirror enhancement, the majority of the backwall effects can be removed without causing an obvious image degradation. By comparing Fig. 3.12(a) and (b), it is obvious that the implementation of mirror enhancement can help to reduce the

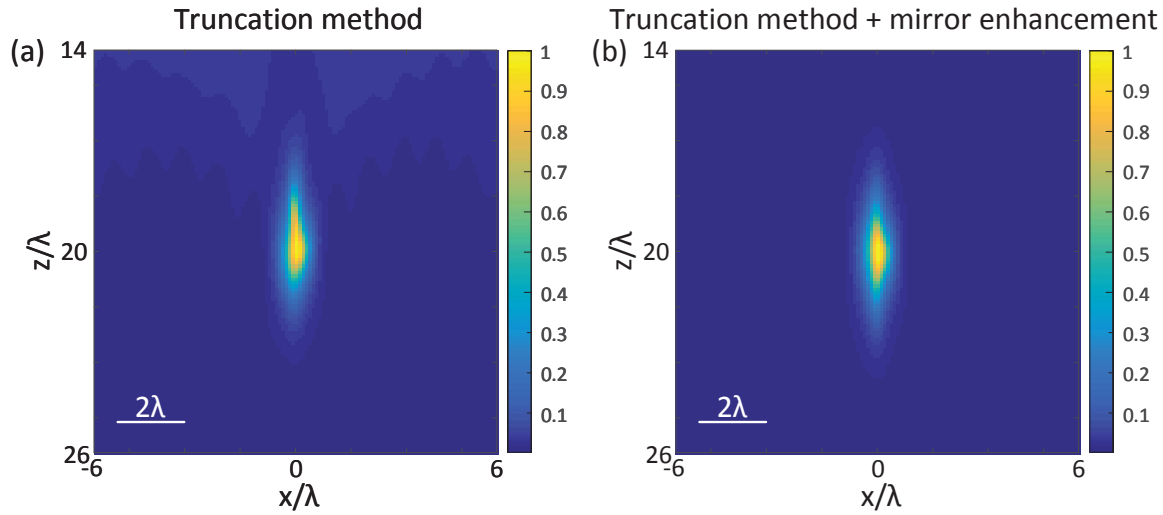


Figure 3.12: Results from setup shown in Fig. 3.2. (a) FM image using the the truncation method to eliminate the backwall effects, (b) FM image using the the truncation method to eliminate the backwall effects and the mirror enhancement to improve the image quality. The images were normalized to the maximum value in each image. The results here were from simulated data.

background noise to improve the image quality.

3.4 Experimental validation

For experimental validation, an array with the parameters shown in Table 3.1 was used for the experimental measurements. This array probe was manufactured by IMASONIC ($Haute - Saône$, France). The sample used for the experimental measurements was a

Table 3.1: Specification of the array transducer used in experimental measurements.

Element number	Central frequency (MHz)	Bandwidth (-6dB; MHz)	Element width (mm)	Element pitch (mm)	Aperture size (mm)
48	2.5	1.66 to 3.22	1.0	1.2	57.4

block of $180 \times 450 \times 40$mm, 304 stainless steel. This sample contains a surface-breaking crack with a size (depth $\times$ length) of 5×20.4 mm and an average opening of $73.0\mu m$, see Fig. 3.13. The crack was produced by using controlled thermal fatigue loading [82]. The depth of the crack is estimated empirically, by destructively analysing previous samples made under the same loading conditions, while the length and opening are measured

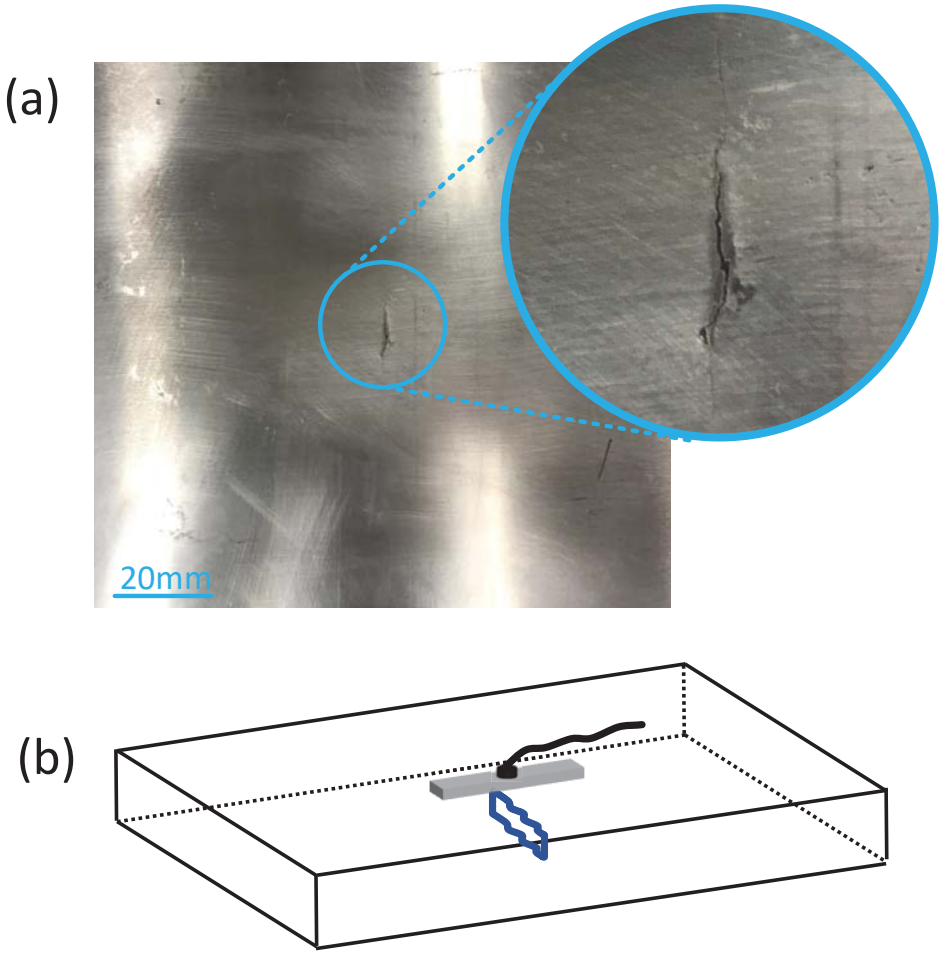


Figure 3.13: (a) The picture of the sample and the crack opening. (b) Schematic showing the experimental setup.

from the micrograph [83]. The surfaces of this sample are flat and smooth. The flawed sample was produced and measured by Trueflaw Ltd. The longitudinal wave speed in 304 stainless steel is $5920m/s$, thus, the depth of the crack is about 2λ for the centre frequency of the 2.5MHz probe. The FMC data were collected from this sample using the 2.5MHz probe, with the same array configuration of $\theta_{test} = 0$ (Fig. 3.1(a)).

After the acquisition of the FMC data, the two imaging algorithms, i.e. the HSTFM and the FM, together with the relevant methods developed to eliminate the backwall effects, were applied to the same FMC data, and all the imaging results are shown in Fig. 3.14. These image results based on the experimental data show a good consistency with those obtained from simulated data.

All the images in Fig. 3.14 show a very good indication of the surface-breaking crack,

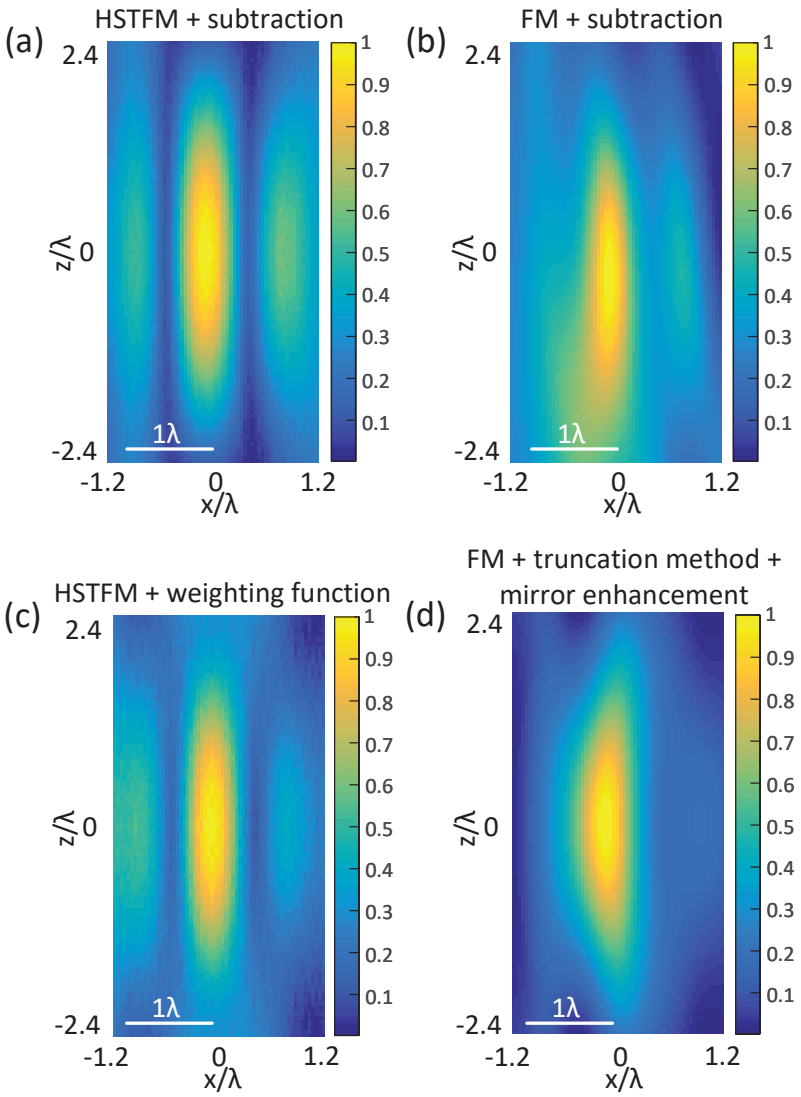


Figure 3.14: (a) HSTFM and (b) FM images based on the FMC data after FMC subtraction, (c) HSTFM with the weighting function image based on the original FMC data, (d) FM with the truncation method and the mirror enhancement image based on the original FMC data. The images are normalized to the maximum value in each image. The results here are from experimental data.

indicating that the methods developed in this chapter, i.e. the FMC subtraction, the weighting function for the HSTFM, and the truncation method for the FM, can successfully eliminate the backwall effects while imaging the near backwall defects, although it is recognised that this is an idealised lab-based setup. The difference between the FMC subtraction and the weighting function method (or the truncation method) is that the FMC subtraction attempts to remove the backwall reflection in the FMC data while the weighting function method (or the truncation method) attempts to directly remove the backwall effects in the imaging process. From the imaging results, it is clear that the images processed by the direct methods (the weighting function method and the truncation method) show a better image quality and contain fewer artefacts than the images processed by the FMC subtraction, see Fig. 3.14(a) vs Fig. 3.14(c) (or Fig. 3.14(b) vs Fig. 3.14(d)). This is because the FMC subtraction will leave a residual backwall reflection in the FMC data after subtraction. The advantage of the FMC subtraction is that this method is very easy to implement as no prior knowledge is needed and it is therefore suitable for any imaging algorithm which utilises the scattered signal to reconstruct the defect. Unlike the FMC subtraction, the weighting function method is developed specifically for HSTFM while the truncation method for the FM requires tuning of the threshold criterion for different imaging configurations. The best result in these images is Fig. 3.14(c), as it contains fewer artefacts compared to the other images and has an accurate reconstruction of the crack. The imaging results also indicate that the two imaging algorithms, i.e. the HSTFM and the FM, have the potential to reconstruct small near backwall defects if the backwall effects can be removed. In [31], Felice et al. has achieved a clear image of a 1.5λ surface-breaking EDM notch by using HSTFM with an offset array ($\theta_{test} = 45°$), however, this method will introduce strong artefacts under the location of the array, which may mask the presence of other defects.

3.5 Conclusions

In this chapter, new techniques to image near-surface defects and to eliminate the backwall effects were presented. This involves both the imaging algorithms themselves and pre-processing methods to eliminate the backwall effects. Two imaging algorithms, the

HSTFM and the FM, were chosen in this chapter to solve the problem of imaging the near backwall defects. However, the two imaging algorithms failed to image the near backwall defects when applied to the original FMC data which contains the backwall reflection, because the strong backwall reflection will introduce strong artefacts to the images. In response to this problem, three methods were developed in this chapter to eliminate the backwall effects and to ensure a good image quality of the defect. FMC subtraction attempts to reconstruct the pure backwall reflection based on the original FMC data and the defect signal can be simply extracted by subtraction. The implementation of this method needs no prior knowledge of the component geometry and this method is theoretically suitable for any imaging algorithms, although it does require the backwall to be parallel to the array. This method will leave some residual backwall reflection in the data, but this is not entirely problematic as the majority of the backwall reflection will be removed. The second method, the weighting function method, is based on the angle difference between the backwall reflection and the defect signal considered in the HSTFM. The weighting function method is developed specifically for HSTFM and can directly filter the artefacts introduced by the backwall reflection in the HSTFM image. The third method, the truncation method, attempts to control the behaviour of the image by selecting the singular values used for the FM algorithm. The implementation of this method needs to tune the threshold criterion at first. The threshold criterion is used to determine which singular values should be used for calculation and this criterion depends on the geometry of the component and the type of defect expected. The truncation of the singular values will cause a loss of information which may degrade the image quality. To compensate for the loss of information caused by the truncation method, a method called the mirror enhancement has been developed to increase the available aperture when imaging the near backwall defects.

These imaging algorithms together with the relevant methods to eliminate the backwall effects are tested with simulated and experimental data, and their performance is assessed through the imaging results. Based on the imaging results, it can be concluded that all the methods developed in this chapter have shown effectiveness to eliminate the backwall effects and are simple in their implementation at the same time. All the imaging results have shown a significant reduction in artefacts when the described methods were applied.

The results also indicate that the imaging algorithms, i.e. the HSTFM and the FM, are able to image the near backwall defects if the backwall effects are eliminated.

Chapter 4

Accurate depth measurement of surface-breaking notches using the Factorization Method

4.1 Introduction

Having developed several backwall eliminating methods in Chapter 3, this chapter studies the practical application of characterising surface-breaking notches.

Among established NDE techniques, there are only two practical modalities for this challenge in subsurface NDE inspections, ultrasound and radiography [84]. Radiography is a NDE technique based on measuring x-ray radiation having been transmitted through a component, effectively recording the cumulative attenuation experienced along each ray path. This can provide an indication of any subsurface defects. Because of the principle of this technique, any defect must be well aligned with the ray paths for maximum detectability, thus a thin crack with unfavourable orientation will be hard to detect through radiography [85]. Another big issue of radiography is the use of ionising radiation, which is harmful to humans in even small doses. For the purposes of safety, a large exclusion zone must be cordoned off around the inspection location to prevent any significant human exposure [1], which makes the approach highly impractical in many practical scenarios.

Compared to radiography, ultrasonic testing is more suitable for routine detection of

near backwall surface-breaking notches as it is safer and much easier to implement [86]. One direct idea of sizing the surface-breaking notch directly from ultrasonic signals is to measure the flight time of the diffracted echoes and calculate the notch depth with the knowledge of the geometry of the component, which has led to the development of the Impulse-Echo-Technique (IET) [87] and the Time of Flight Diffraction Technique (TOFD) [32,88]. Shiuh-Chuan Her et al. [89,90] applied the IET to conduct the through-wall detection of the surface-breaking notches, while Baby et al. [33] evaluated the depth of the surface-breaking notch on the far surface using the TOFD. The results of their work showed that these methods can achieve a good accuracy for a notch larger than one wavelength but have a poor performance for the notches smaller than one wavelength [33, 89].

Driven by the need of more sensitive and reliable inspections, the use of ultrasonic arrays as an alternative for the reliable sizing of the near backwall surface-breaking notches has attracted a lot of attention [28,31,55]. As has been mentioned in Chapter 1, the commonly used imaging algorithm (TFM) is not effective enough for near backwall defects where there is additional complexity from the wave reflecting from the backwall. In [31,55], Felice et al. used the Half-Skip Total Focusing Method (HSTFM) to measure the depth of the surface-breaking notch which is near the backwall. The results showed that the HSTFM has the ability to size a 1.5 wavelength surface-breaking notch that is impossible to be measured through the conventional TFM, however, the HSTFM still had a poor accuracy for the notches smaller than 1.5 wavelength [31]. Also, as mentioned in Chapter 2, the HSTFM is based on the weak scattering approximation (i.e. the Born approximation) and has a resolution limit of 0.5 wavelength, which will limit the application of these methods in high resolution imaging [39].

As an alternative approach, J. Zhang et al. [28] used a scattering matrix based approach, which compares an experimentally acquired scattering matrix to a database of pre-calculated scattering matrices to characterize the defect. This method has achieved a good accuracy based on the experiment array data, however, for this method, even for a limited type of defect, a large number of scattering matrices have to be calculated. To ensure the accuracy of sizing, the implementation of this method needs a prior TFM image to achieve the knowledge of the defect location and backwall location, and in order

to minimise the error, the array should be aligned with the defect as much as possible. These prerequisites may limit the application of this method in real applications.

In this chapter, the ability of the FM to image and size the surface-breaking notches is explored. As has been shown in Chapter 3, when a zero incident angle is chosen (Fig. 3.1(c)) and FM is used to image the near backwall defects, it will be impossible to have a clear reconstruction if the backwall effects are present. In response to this problem, some backwall eliminating methods for FM have been developed in Chapter 3. Thus, the remainder of this chapter is organised as, follows with the motivation to practically apply the FM to the detection of near backwall defects. Firstly, a detailed introduction about the FE models that will be used to provide array data is provided. Then, the imaging results of the TFM and the FM based on the pure defect signal are shown and compared. Based on this, the effectiveness of the FM is discussed and the sizing method of the FM is described. More importantly, the effectivenesses of the FM with the relevant backwall eliminating methods on the FMC data which contains both backwall reflection and defect signal are examined. The experimental validations of the FM with the relevant backwall eliminating methods and the sizing methods are also provided in this chapter. Although relevant methods have also been developed for the HSTFM to eliminate the backwall effects, the use of the HSTFM to image and size surface-braking notches has already been studied in [31, 55], thus, interested readers can refer to [31, 55] for details.

The work in this chapter is published in IEEE Trans. Ultras. Ferr. Freq. Control 2018 [P1].

4.2 FE model description

In this chapter, Finite Element (FE) modelling has been used to compare the performances of TFM and FM on imaging surface-breaking notches and to study the effects of the FMC subtraction mentioned in the previous section.

Fig. 4.1 shows a schematic diagram of the FE model used to simulate the phased array imaging of the surface-breaking notch. This model has been run using the commercial FE package ABAQUS/Explict [91]. The input source was introduced by exciting a concentrated force with a time-varying amplitude on the source point. The input force signal

was a 5-cycle tone burst with a centre frequency of 2MHz. We have defined 64 source points distributed uniformly on the upper surface to represent a 64 element phased array. Every source point was also set as a monitoring point as every element of a phased array can be used as a transmitter and a receiver.

The material used for simulation was steel with a density of $7700kg/m^3$, a Young's modulus of 195GPa and a Poisson ratio of 0.28. Thus, the wavelength λ of the longitudinal wave was about 3mm. To simplify the problem, the material was isotropic throughout. The sample had a thickness of h=60mm and a surface-breaking notch of $\theta_{tilt} = 0°$, while the phased array was placed at $\theta_{test} = 0°$ to ensure the largest angle of view. The 4 node bilinear plane strain quadrilateral elements with a length of 0.1mm were utilised in this model. For simplification, only the longitudinal wave was excited and recorded at monitoring points [76]. The shear waves and mode conversions between the longitudinal and shear waves are not considered in this chapter, which is because these waves always arrive later than the longitudinal waves used for imaging and the derivation of the FM is based on the acoustic waves which are a type of longitudinal wave. Absorbing layers [77] were attached to the model to absorb any wave entering them, acting as 'reflectionless boundaries', to effectively model a small section of an infinite region.

In order to simulate the working process of phased array imaging, the 64 source elements were fired successively while all the monitoring points were working simultaneously, which was described as the FMC in the previous section. As the purpose of the simulation is to compare the performance of the imaging algorithms and the backwall subtraction methods, simulation results from different notch depths are necessary. As a result, 6 models with the same material and array parameters but different notch depths were created and the notch depths were 0.5λ, 1λ, 2λ, 3λ, 4λ and 5λ, respectively.

4.3 FM vs TFM

In this section, the performances of TFM and FM were compared directly by using them to image the same surface-breaking notches. For the comparison between the TFM and the FM, the backwall reflections were subtracted by using the baseline subtraction technique as this is easy to implement with numerical data, and will enable the backwall reflections

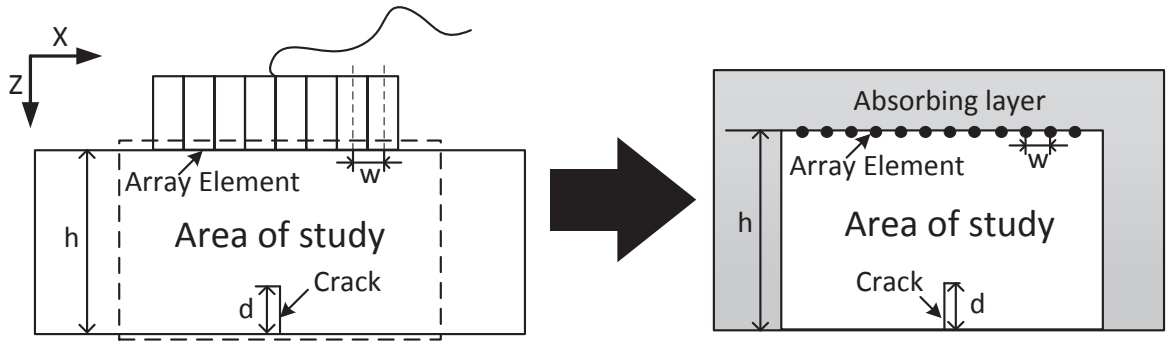


Figure 4.1: Schematic of the FE model (not to scale).

to be removed clearly. In the following numerical examples, if not otherwise specified, the TFM is performed in the time domain, i.e. using the full frequency spectrum of the recorded signals, and the FM is performed using the central frequency component of the recorded signal. In addition, for the standard FM, all of the singular values at the central frequency are used to generate the FM images. Thus, TFM uses all the available information in the signals while for FM, some part of the information contained in the measured signals is discarded. It is still an open question exactly how much more information there is in the full spectrum vs just at a single frequency.

The TFM algorithm and the FM algorithm were applied to the simulated FMC data and the resulting images based on the data from the model with a notch depth of 4λ are shown in Fig. 4.2(a) and Fig. 4.2(b), respectively. From Fig. 4.2(a), it is clear that the conventional TFM successfully reconstructed the notch tip and the notch root to indicate the presence of the notch. However, the intensity of the indication of the notch tip was much smaller than the indication of the notch root as the energy of the tip diffraction is weak. At the same time, the tip is not as obvious as the root and the intensity of the artefacts in the image are comparable to the notch tip. As a result, if TFM is used in the practical application of imaging surface-braking cracks, the tip indication may not be distinguishable from the artefacts so the crack will be hard to size. From Fig. 4.2(b), we can see that both the location and the shape of the notch has been reconstructed correctly by FM. Because of the advantage in resolution, the image reconstructed by FM is sharper and clearer than the image reconstructed by TFM; additionally, as FM attempts to directly reconstruct the shape of the object, the defect in the resulting FM

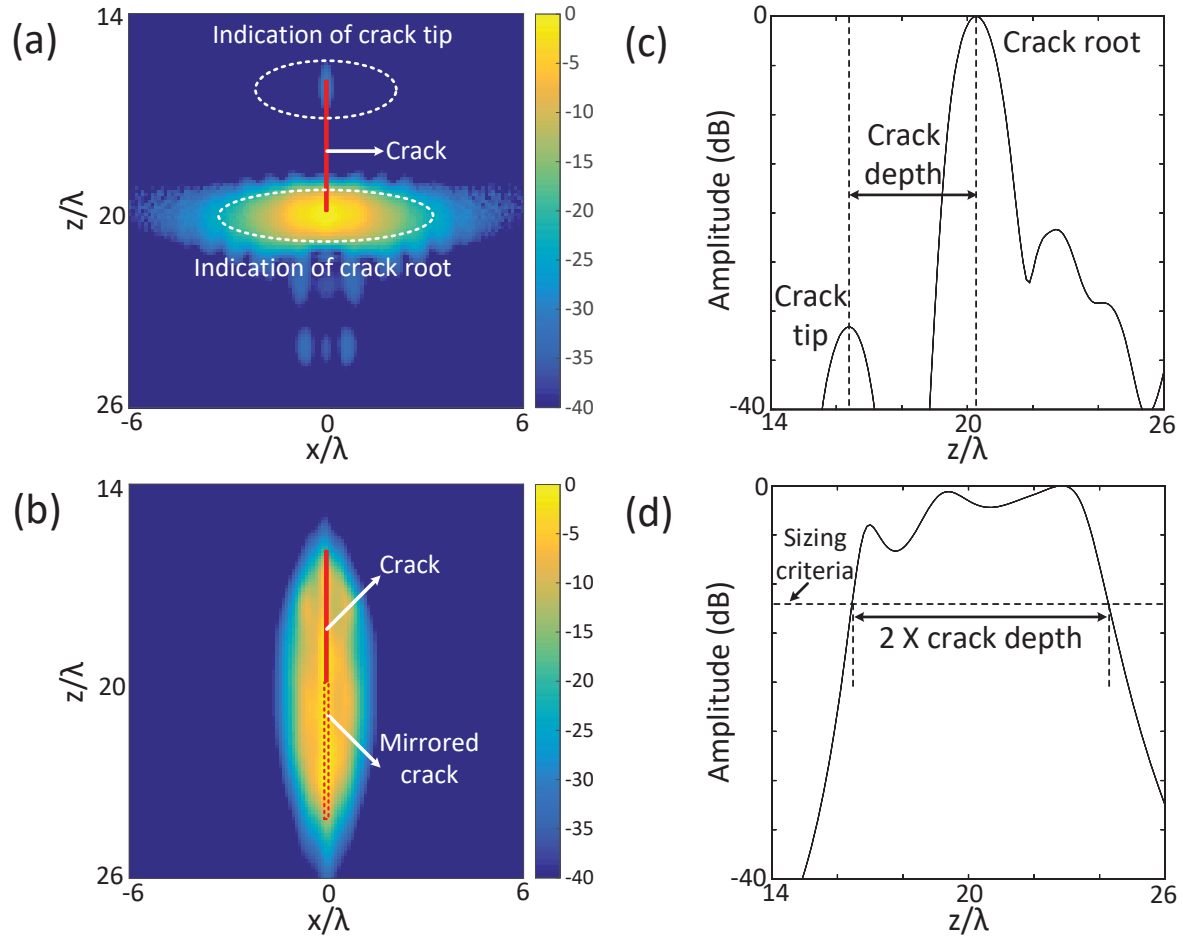


Figure 4.2: (a) TFM image of a 4λ deep notch. (b) FM image of a 4λ deep notch. (c) Notch sizing method for the TFM image. (d) Notch sizing method for the FM image. Note that the red lines in the images were used to indicate the location and length of the notch in models and the amplitude is on dB scale, normalized to the maximum value in each image. The results here were from simulated data.

image is easier to identify as a notch than the TFM image.

The principal objective of subsurface imaging is to have an accurate sizing of the surface-breaking notch. As the indications of the notch are different between the TFM image and the FM image, the sizing methods used for the FM image are quite different from the TFM image. For FM, the sizing method is shown in Fig. 4.2(d). In this, the centre of the notch in the horizontal direction, x_c, is determined as the position where the pixel has the maximum amplitude in the image, then the image value at $x = x_c$ is plotted against vertical distance, z. After that, the z values of the two points on the plot whose amplitude are equal to the sizing threshold are measured, where the sizing criterion is a

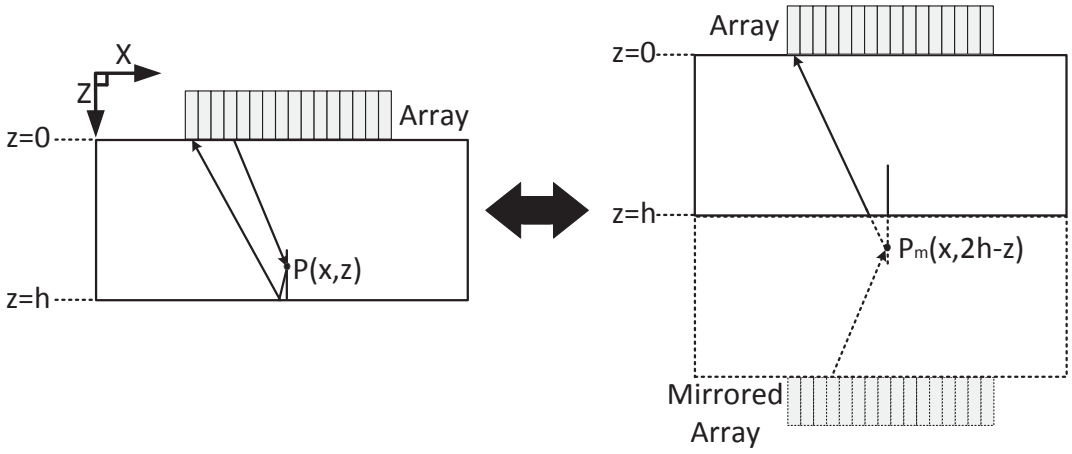


Figure 4.3: Schematic of the wave undergoing the half-skip reflection, which causes mirror effect in the FM images.

manually set number used for sizing, e.g. -6dB or -12dB from the peak, and finally, the notch depth is equal to half of the difference of the two measured z values, due to the mirroring effect. For the TFM image of the same notch, the image value at the same x_c is plotted, but the notch depth is determined by measuring the distance between the peak of the root indication and the peak of the tip indication (Fig. 4.2(c)).

In the FM image, it can be noticed that half of the indication of the notch is just above the location of the backwall and half of the indication is beneath the backwall, i.e. the imaging algorithm reconstructed a mirrored notch in the image. That is because for a point P along the notch above the backwall, there are different ray paths of the ultrasound from the transmitter to the point P and back to the receiver. One travels directly from the transmitter to P and back to the receiver, while another one is reflected in the backwall at each interaction. There are also other 'half skip' paths which are reflected on the backwall once, either before or after interacting with the defect. The length of the pre-defect reflection half-skip path is that of a path from the mirrored array to the mirrored point P_m beneath the backwall and then directly back to the real array, as shown in Fig. 4.3. It is noted that the same is true for a post-defect reflection by reciprocity. For the FM imaging algorithm, when the position of the real array is used for imaging, the ultrasound waves that underwent the direct ray path gave the intensity to the point P above the backwall and the waves that underwent the half-skip reflection gave the intensity of the point P_m beneath the backwall.

The noise was not considered in the previous comparison. From Eq. (2.69), we can notice that FM uses all the singular values including those with very small amplitudes. Those small singular values contain the information of the object and are crucial for achieving super resolution, however, those singular values are easily lost or corrupted with the presence of the noise. The TFM method is essentially a Beamforming algorithm which mainly depends on the large singular values [75], which is why TFM is more noise robust than FM.

Typically, the imaging algorithms will experience various levels of noise, and be used with a variety of notch sizes. In order to compare the TFM algorithm and the FM algorithm in a more direct way and explore the limitations of each imaging algorithm, the two algorithms were applied to simulated data with different notch depths and noise levels, as shown in Fig. 4.4. Various levels of additive white Gaussian noise were added to the simulated signals. The noise was scaled relative to the root-mean-square (RMS) magnitude of the simulated signal, for example, 20dB SNR corresponds to noise with a RMS magnitude of 10% of the RMS magnitude of the simulated signal.

As TFM is noise robust, only two extreme noise levels (50dB and 5dB) are considered here. For the TFM images, with the smaller notch depth, the indication of the notch tip is closer to the indication of the notch root. As the energy of the tip diffraction is much weaker than the energy reflected by the root corner, the indication of the notch tip is much weaker than the root, which causes the tip to be masked by the root in the TFM image of the 1λ deep notch. The smallest notch that TFM can successfully reconstruct is about 2λ, which shows good consistency with other research focused on imaging small notches [31]. The TFM algorithm shows excellent robustness to noise as the addition of the noise does not affect the TFM images.

When the backwall reflection is removed clearly, the FM algorithm shows good robustness to the reduction of the notch depth and the addition of the noise, but one trend is also very clear: with an increase in noise, more artefacts are introduced around the reconstructed notches in the images. As the indication of the notch shape is much more robust than the artefacts introduced by the noise in the FM image, the judgement and sizing of the notch would not be influenced by the addition of the noise when a pure scattered field is used for imaging. FM has an advantage in imaging resolution [92] and it directly estimates

the notch shape rather than estimating the indication of notch tip and root, thus, it can reconstruct a small notch that cannot be successfully reconstructed by TFM, for example a 1λ deep notch.

Fig. 4.5 shows the sizing results of the TFM and the FM methods with different notch depths and noise levels. TFM shows a very accurate estimation of the notch depth with an error smaller than 5%. TFM also shows excellent noise robustness as the sizing results stay the same when the noise level varies. However, for TFM, notches which are smaller than 2λ are neither detectable nor measurable. Fig. 4.5 shows the sizing results of the FM under two different sizing criteria, -6dB and -12dB thresholds below the peak amplitude. Using the different sizing criteria, the sizing results of the FM are also different. By using the -6dB as the criterion – a common threshold used in industry, the notch depths were undersized; while using the -12dB criterion, the FM is able to accurately size the notch from 1λ and the sizing results show a good consistency to the sizing results of TFM. For notches larger than 1λ, FM can provide accurate sizing even for a large noise level ($SNR = 5dB$) with an error smaller than 7.5%. The noise level will affect the sizing results of the FM algorithm, especially for the small notches, as the sizing error for the 1λ notch is 5% when $SNR = 50dB$ but 20% when $SNR = 5dB$, however, for the notches larger than 1λ, the influence of the noise level is negligible. Based on these results, it is clear that using -12dB threshold is able to have an accurate sizing from standard FM images. As further decreasing the sizing threshold will increase the risk of measuring noise (e.g. -15dB), if not otherwise specified, -12dB is used as the sizing criterion for the standard FM images. Also, these sizing results demonstrate that FM outperforms HSTFM in imaging small surface-breaking notch, as HSTFM can only accurately image and characterise notches that are bigger than 1.5λ [31]. It should be noted that the sizing results here are based on the data from one noise realisation, different noise realisations need to be investigated in the future to validate the sizing accuracy of the FM images.

4.3.1 The effect of the FMC subtraction

Here, the effects of two different methods to remove the backwall reflections to enhance the reconstruction of near-backwall defects are compared. Among the two methods, one

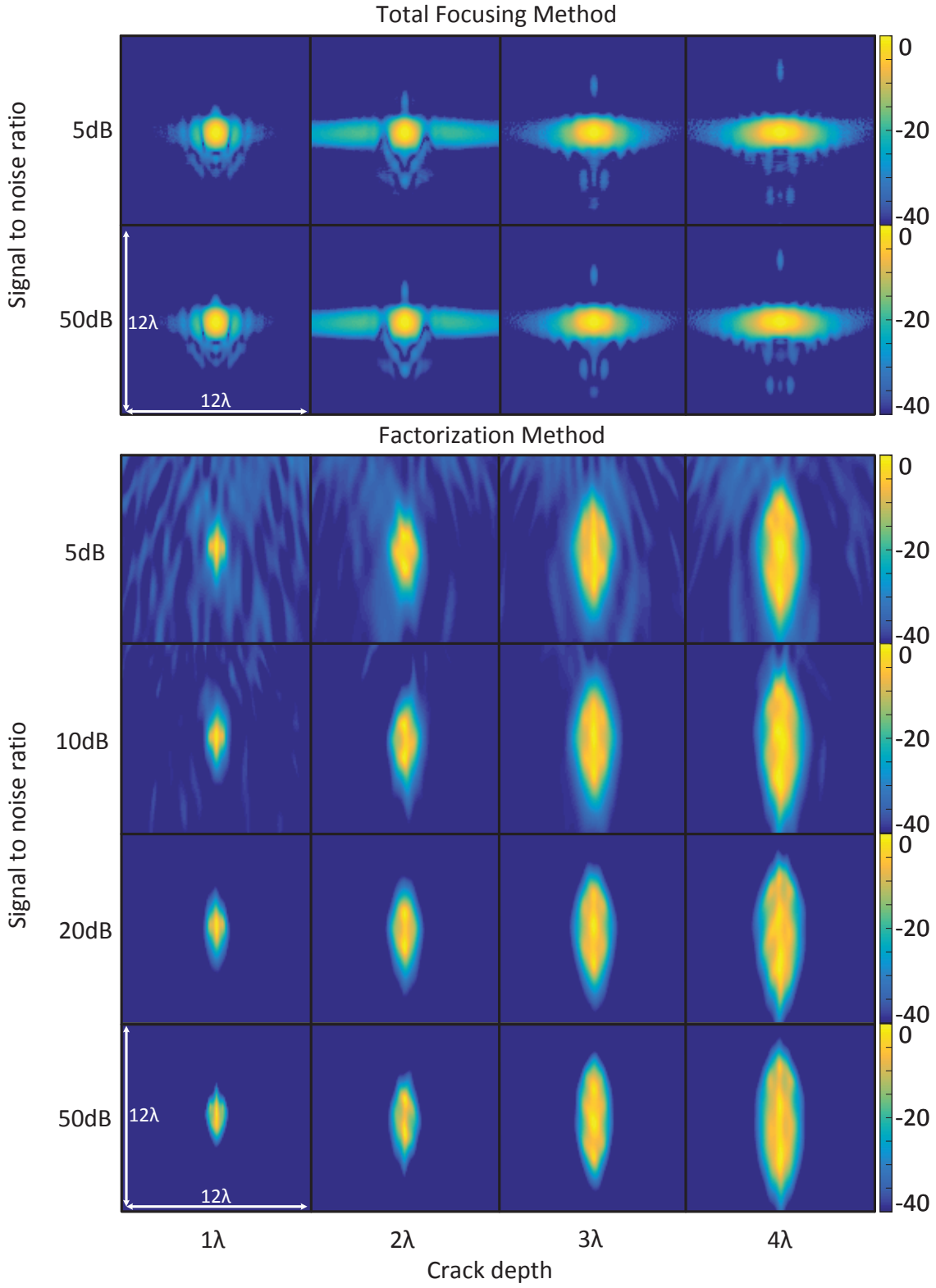


Figure 4.4: The imaging results of the TFM and the FM with various noise levels and notch depths. The TFM results only contain two noise levels as TFM is not sensitive to the noise. Note the images were normalized to the maximum value in each image. The results here were from simulated data.

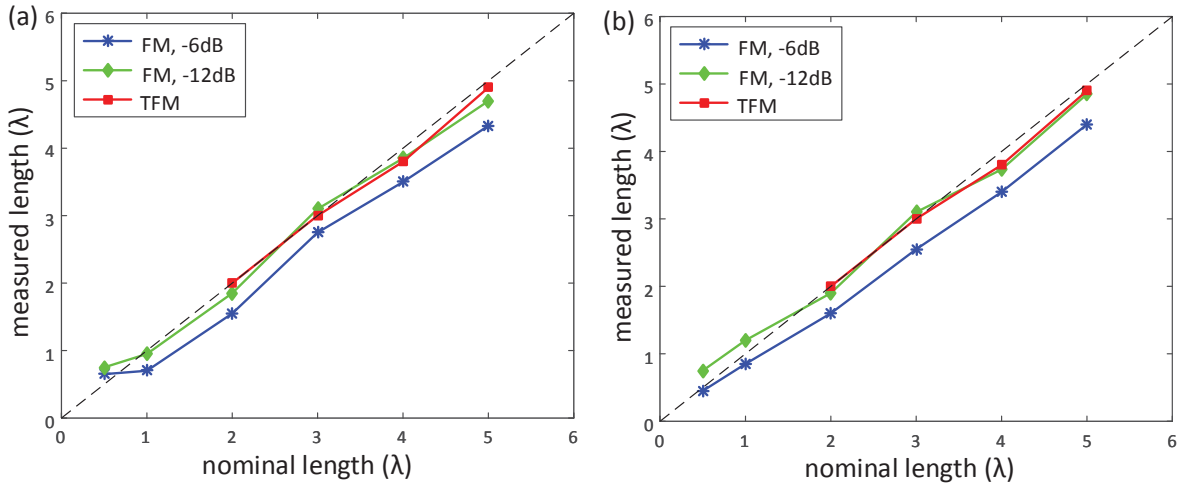


Figure 4.5: The sizing results of the TFM and the FM with different notch depths and noise levels: (a) The sizing results when SNR=50dB; (b) The sizing results when SNR=5dB. The -6dB and -12dB correspond to the amplitudes relative to the peak at which the end of the notch is considered to end, providing a sizing estimate.

is baseline subtraction and the other one is the FMC subtraction, and the definition for each of these can be found in previous sections. The removal of the backwall reflection from measured data is based on the subtraction of a pure backwall reflection when the notch is absent. For baseline subtraction, this backwall reflection is obtained through measuring the data from a defect-free copy of the component under inspection, while for FMC subtraction, the pure backwall reflection is estimated based on the FMC data obtained through the component under inspection. The backwall reflection components for the two cases, taken from a simulated example with a notch of depth 2λ, are plotted in Fig. 4.6.

By observing the plots carefully, we can find that for the FMC subtraction method, the reconstructed pure backwall reflections are quite close to the pure backwall reflection obtained through the defect-free model, especially when the number difference between the transmitter and receiver, i.e. $|i-j|$, is small. When $|i-j|$ becomes larger, the FMC subtraction starts to underestimate the amplitude of the pure backwall reflection although the phases are correctly estimated. This is because the reconstruction of the backwall reflection from the FMC data is based on the averaging of different time traces with the same $|i-j|$, and for large $|i-j|$ there are fewer time traces in the FMC data compared to the small $|i-j|$. As an example, for $|i-j|=1$, there are 126 time traces in

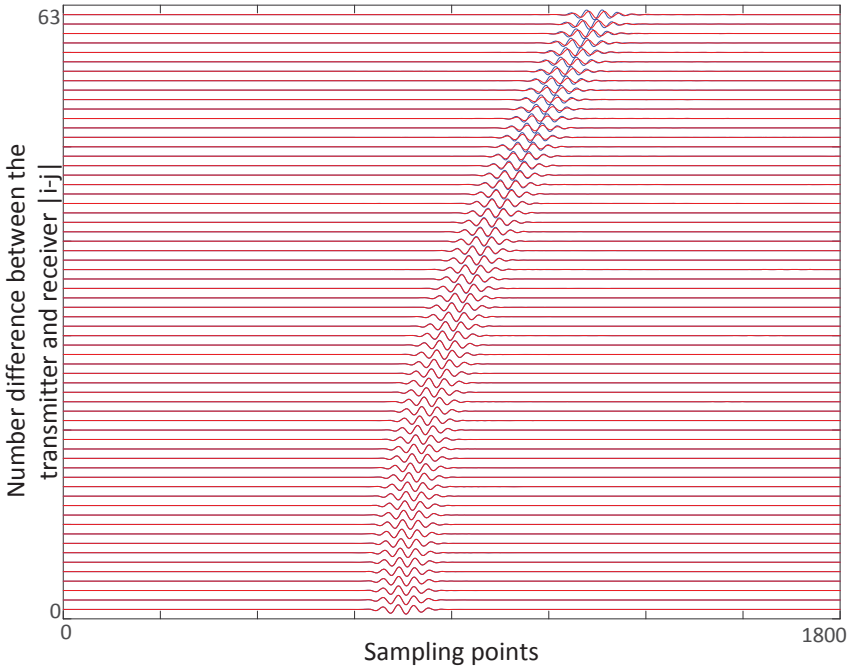


Figure 4.6: Plots of the pure backwall reflections used in the baseline subtraction (blue) and the FMC subtraction (red). Note that array element 1 is used as the transmitter while all the elements used as receivers.

FMC data, i.e. $I(1,2), I(2,1), \cdots, I(63,64), I(64,63)$. However, for $|i-j| = 63$, there are only two time traces contained in the FMC data: $I(1,64)$ and $I(64,1)$. As a result, with large $|i-j|$, there are only a few time traces that can be used for averaging, meaning that the backwall reflection estimate is likely to be of limited accuracy. For all of the estimated backwall reflections obtained by the Eq. 3.2, the biggest error is 45% and the smallest error is 1.8% when compared to the backwall reflection used in the baseline subtraction, where the error refers to the difference in peak amplitude here.

Because of the presence of the errors, there are some residual components of backwall reflection after FMC subtraction, which will influence the quality of the images generated. As the error varies for different time traces and there are huge numbers of time traces contained in the FMC data, it is hard to study the effects of the FMC subtraction directly. A possible way is to compare the imaging results using different subtraction methods.

Fig. 4.7(a) is the TFM image of a 2λ notch without removing the backwall reflection. This image contains a very strong indication of the backwall which masks the indication of the notch root. As a result, it is hard to judge the type of defect, thus the sizing of the notch will be impossible. Fig. 4.7(b) is the TFM image after the backwall reflection

was removed by the baseline subtraction. This image shows a clear indication of the notch root and the notch tip, and according to the previous section, will provide an accurate estimation of the notch depth. Fig. 4.7(c) is the TFM image after the backwall reflection was removed by the FMC subtraction. This image provides a good indication of the notch root and notch tip and is quite close to Fig. 4.7(b). It indicates that the FMC subtraction can remove the majority of the backwall reflection and the effect of this method is roughly equal to the baseline subtraction for the TFM algorithm. Additionally, FMC subtraction also showed good noise robustness for the TFM algorithm as the TFM images were generated at a high noise level, i.e. $SNR = 5dB$. It should be noted that FMC subtraction approach suppresses the backwall more effectively away from the defect location, since the defect itself can introduce some coherent components which are not removed by averaging.

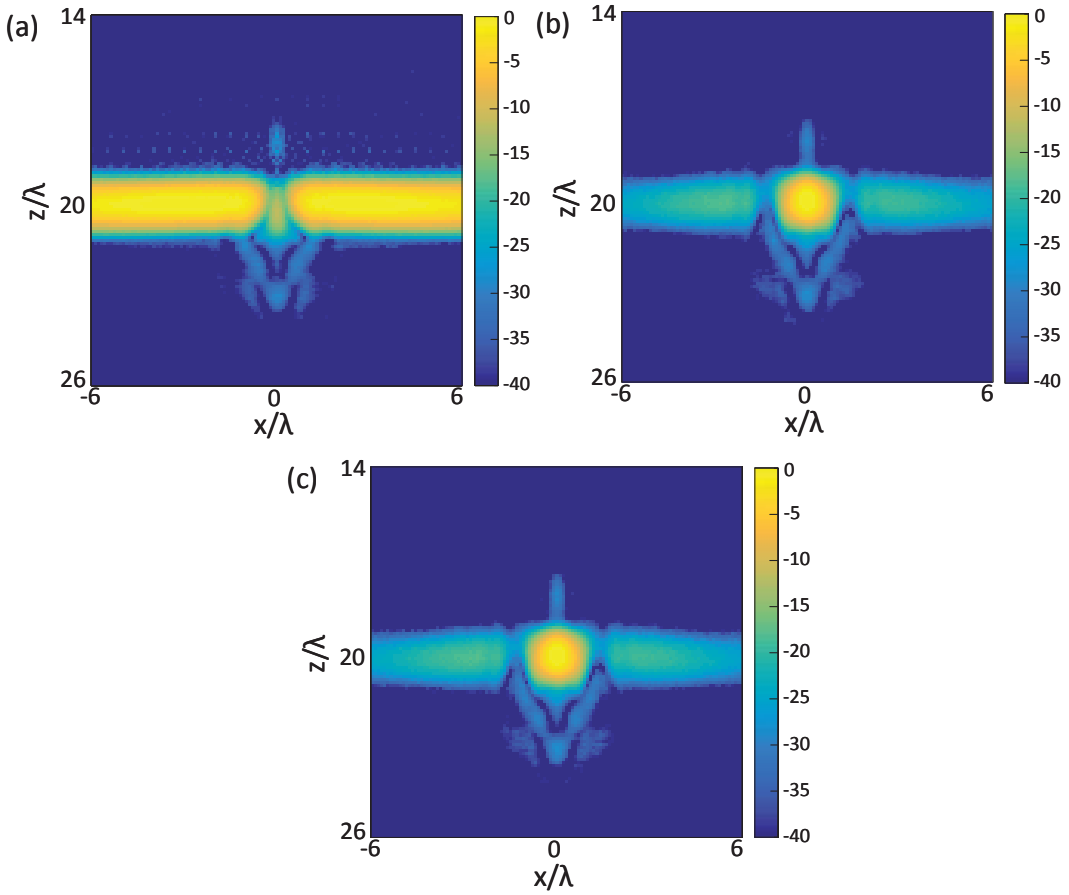


Figure 4.7: The TFM images of a 2λ notch when $SNR = 5dB$: (a) Without removing the backwall reflection; (b) The backwall reflection was removed by baseline subtraction; (c) The backwall reflection was removed by FMC subtraction. Note that the images were normalized to the maximum value in each image. The results here were from simulated data.

Fig. 4.8(a) and Fig. 4.8(b) are the FM images of a 2λ notch without removing the backwall reflection at $SNR = 50dB$ and $SNR = 5dB$, respectively. From these two images, we can see that the strong indication introduced by the backwall reflection totally masked the indication of the notch. Fig. 4.8(c) and Fig. 4.8(d) are the FM images of a 2λ notch with baseline subtraction at $SNR = 50dB$ and $SNR = 5dB$, respectively. It is clear that the removal of the backwall reflection can significantly improve the quality of the FM images, both in the defect judgement and notch sizing. Additionally, after the baseline subtraction, the FM gave good noise robustness as when the noise level became larger, the indication of the notch remained sharp and stable. Fig. 4.8(e) and Fig. 4.8(f) are the FM images of a 2λ notch with FMC subtraction at $SNR = 50dB$ and $SNR = 5dB$, respectively.

These two images have a sharp indication of the notch which indicates that the FMC subtraction has removed the majority of the backwall reflection. However, as the FM algorithm is much more sensitive to noise than the TFM algorithm, the effect of the residual backwall reflection after FMC subtraction becomes much more obvious. This component introduced strong artefacts into the FM images, which are the strong side bars near the indication of the notch. These artefacts raise the risk of falsely judging the type of the defect. However, these two images also showed good robustness to the noise as the indications of the notch remained stable and sharp even at a high noise level.

Except for the image quality, the effects of the FMC subtraction on the sizing accuracy should also be studied, as one of the main objectives of imaging is to provide an accurate sizing. Fig. 4.9 shows the sizing results of the TFM images and the FM images using different methods to remove the backwall reflection. From these sizing results, we can see that by using the FMC subtraction to remove the backwall reflection, the FM algorithm is able to provide an accurate sizing for a notch whose depth is between 1λ to 3λ, which means that the FMC subtraction only works for small notches. This is because the primary assumption of the FMC subtraction is that the amplitude of the scattered signal is much smaller than the backwall reflection, when the notch becomes larger, the assumption become invalid. However, given that the goal is to improve imaging and sizing of the smallest defects, this trend is not entirely problematic. For the sizing results of the TFM images, it is clear that the effect of the FMC subtraction is roughly equal to the baseline

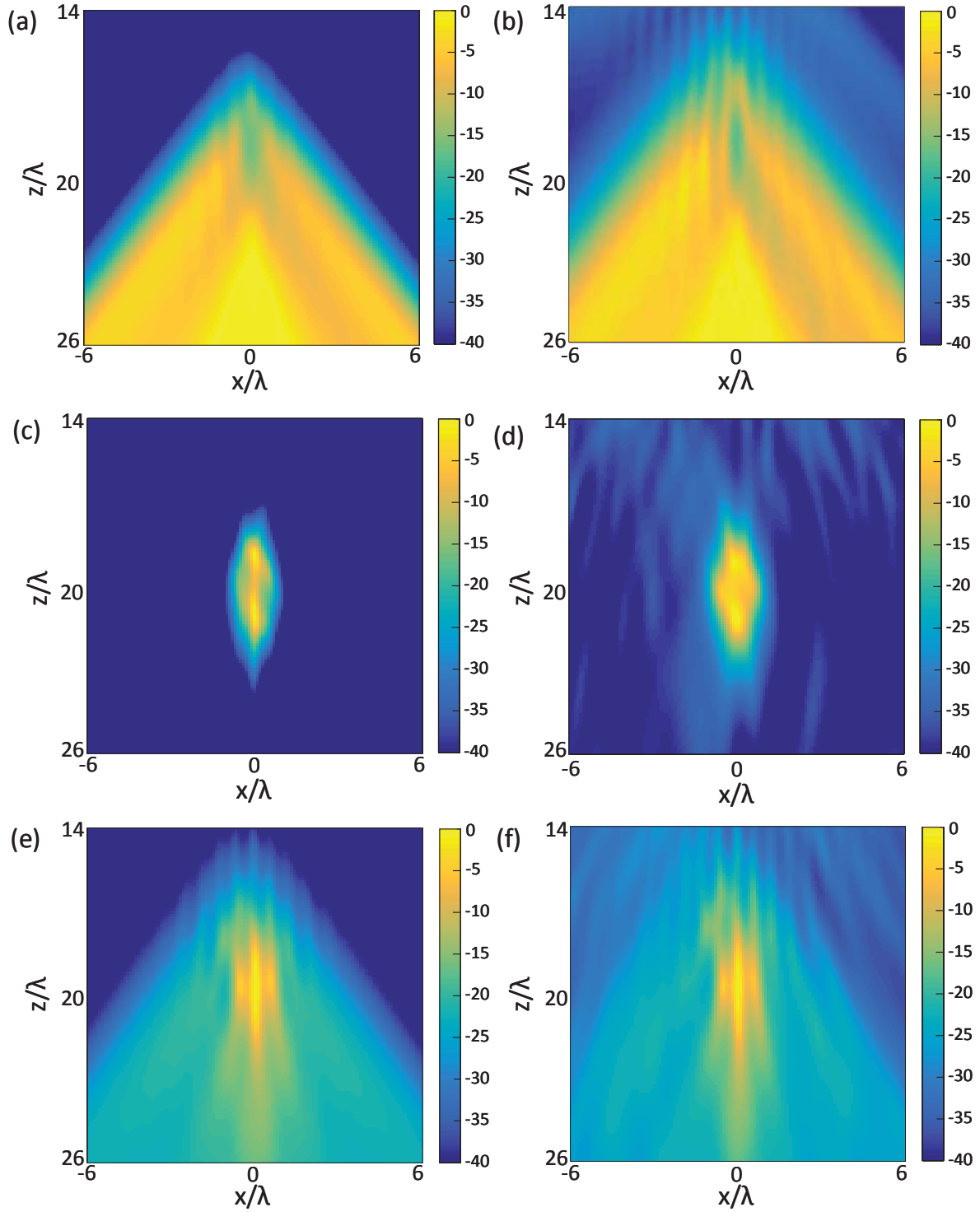


Figure 4.8: The FM images of a 2λ notch: (a) Without removing the backwall reflection at $SNR = 50dB$; (b) Without removing the backwall reflection at $SNR = 5dB$; (c) The backwall reflection was removed by baseline subtraction at $SNR = 50dB$; (d) The backwall reflection was removed by baseline subtraction at $SNR = 5dB$; (e) The backwall reflection was removed by FMC subtraction at $SNR = 50dB$; (f) The backwall reflection was removed by FMC subtraction at $SNR = 5dB$. Note that the images were normalized to the maximum value in each image. The results here were from simulated data.

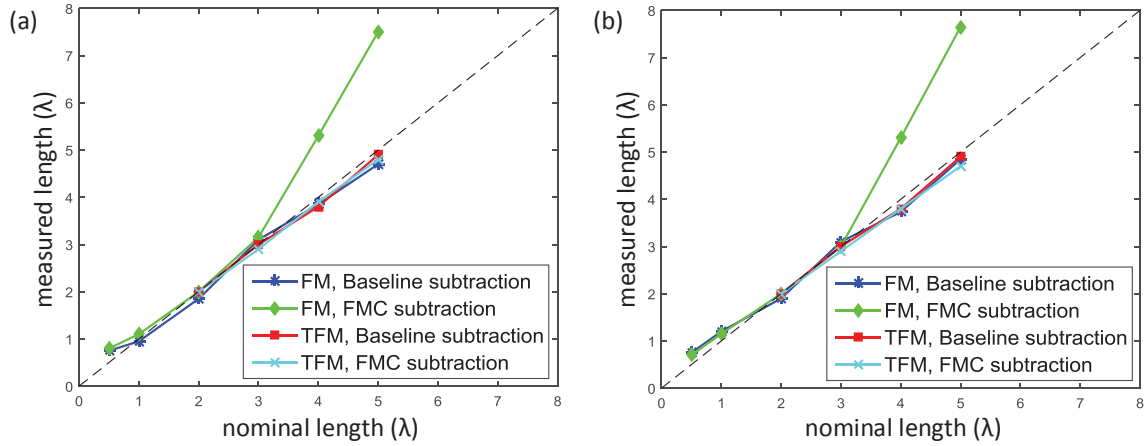


Figure 4.9: The sizing results of the FM images and the TFM images using different methods to remove the backwall reflection: (a) The sizing results when SNR=50dB; (b) The sizing results when SNR=5dB.

subtraction as the sizing results based on these two methods are quite close to each other.

4.3.2 The effect of the truncation method

The truncation method, which has been introduced in Chapter 3, is also a method that can eliminate the backwall effects for the FM. This is different from the FMC subtraction method which is implemented as a signal processing method to the acquired FMC data, this method aims to eliminate the backwall effects during the imaging process by controlling the singular values used for the calculation of the FM images. In order to compensate for the loss of information when fewer singular values are used, the mirror enhancement has been developed (see Chapter 3) to improve the image quality if the truncation method is used. In this chapter, the truncation method is used together with the mirror enhancement to eliminate the backwall effects without a dramatic degradation of the image quality. As the standard FM uses all the singular values for imaging, if the truncation method and the mirror enhancement are used, FM would show different characteristics compared to the standard FM combined with the previously discussed subtraction methods (baseline subtraction or FMC subtraction). Fig. 4.10 shows the imaging results when FM together with the truncation method and mirror enhancement were applied to original simulated data with different notch depths and noise levels.

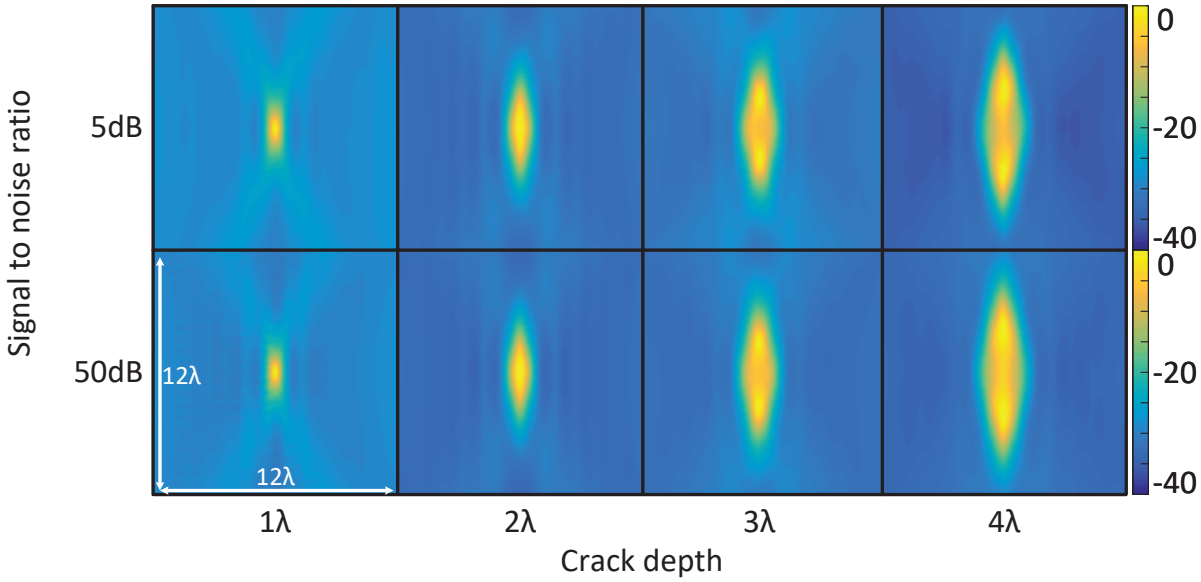


Figure 4.10: The imaging results of the FM with various noise levels and notch depths based on the original FMC data. The truncation method (80% threshold) together with the mirror enhancement were used to eliminate the backwall effects. Note the images were normalized to the maximum value in each image. The results here are from simulated data.

If we compare Fig. 4.4 and Fig. 4.10, it is clear that the employment of the truncation method increases noise robustness of the FM. This is because the truncation method forces the FM to use the information encoded into the larger singular values and the larger singular values would not be significantly affected by the addition of noise when compared to the smaller singular values [75]. Further, from these images, it is also clear that the FM with the truncation method can provide good reconstructions (in both shape and depth) for the notches larger than 1λ. The shape reconstruction of the 1λ notch in Fig. 4.10 is less accurate than the shape reconstruction of the 1λ notch in Fig. 4.4. This is because the truncation method abandons the small singular values which contain information about the finer details of the scatterer and are crucial to achieve super resolution [75]. As has been mentioned before, the principal objective of notch imaging is to ensure an accurate measurement of the notch depth. The application of the truncation method will unavoidably influence the imaging result, making it different from the imaging result generated by the standard FM. Thus, the sizing criterion for FM when the truncation method is applied has to be tuned. The sizing results based on the truncated FM images based on different sizing criterion are shown in Fig. 4.11.

In order to select a proper sizing criterion for the truncated FM images, three different

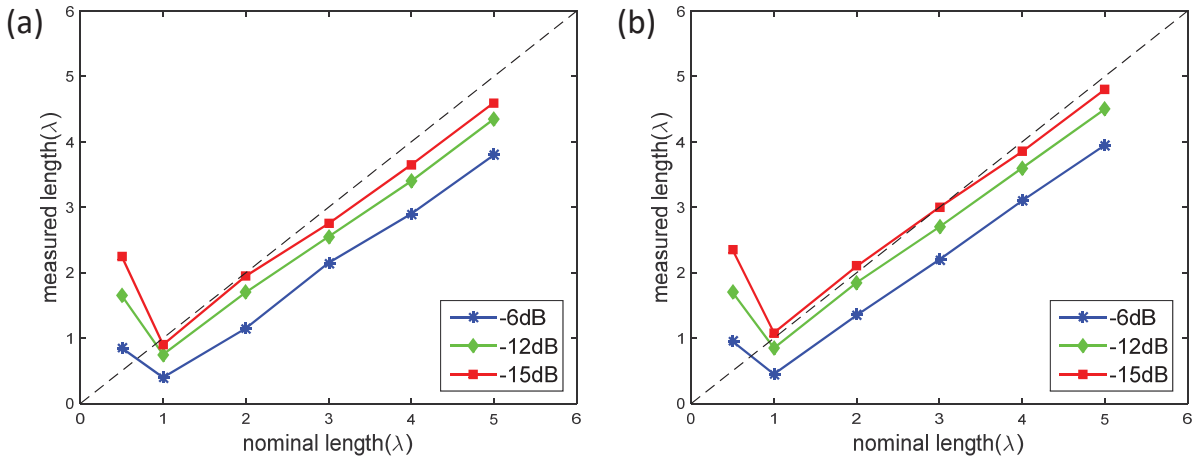


Figure 4.11: The sizing results of the FM images when the truncation method is used to eliminate the backwall effects: (a) The sizing results when SNR=50dB; (b) The sizing results when SNR=5dB.

sizing criteria, i.e. -6dB, -12dB and -15dB, are used in Fig. 4.11. It is clear that by using -6dB or -12dB, the notch depths are underestimated. By using -15dB as the sizing criterion, sizing results are accurate for notches whose depths are not smaller than 1λ with an error smaller than 8.75% under different noise levels. One can immediately see from the sizing results that for the notches smaller than 1λ, all the sizing criteria failed to provide acceptable depth estimations, this is because the FM is not able to accurately reconstruct the shape of the notch when the small singular values are truncated. It is obvious that the noise level can affect the sizing results, especially for the larger notches, as the sizing error for the 4λ is 8.5% when $SNR = 50dB$ but 3.75% when $SNR = 5dB$. In this chapter, if not otherwise specified, -15dB is chosen as the sizing criterion for the FM when the truncation method together with the mirror enhancement are used to eliminate the backwall effects.

4.4 Experiment results

For the experimental validation, two arrays with centre frequencies of 1MHz and 5MHz were used. These two array probes were manufactured by IMASONIC ($Haute - Saône$, France), the details of the parameters are shown in Table 4.1. A mild steel sample with a thickness of 38mm was used (ultrasonic longitudinal wave velocity=5960 m/s). This

Table 4.1: Array parameters

Array parameter	Probe 1	Probe 2
Element number	64	64
Element width (mm)	1.6	0.5
Element pitch (mm)	2.1	0.6
Centre frequency (MHz)	1	5
Bandwidth (-6dB; MHz)	0.756 to 1.33	3.37 to 6.64

sample contains an EDM notch whose depth is 11mm and width is 0.5mm. As a result, for the 1MHz probe, the notch is 1.85λ and for the 5MHz probe, the notch is 9.23λ. The FMC data were collected from this sample using two different probes listed in Table 1, with the same array configuration of $\theta_{test} = 0$ (Fig. 3.1(a)).

Firstly, the performance of FM using FMC subtraction to remove the backwall effects was experimentally validated. Thus, after the acquisition of the FMC data, the backwall reflections were removed by FMC subtraction. For generating the experimental images, TFM was performed in the time domain while FM was performed at the central frequency of the array probe and used all the singular values at the central frequency to generate images, which is in accordance with our numerical simulations. The central frequencies and bandwidths of the two array probes used for experimental validation are listed in Table 4.1. The TFM and FM imaging results at different frequencies are shown in Fig. 4.12. These image results based on the experimental data show a good consistency with the imaging results based on the simulations.

Fig. 4.12(a) and Fig. 4.12(b) are the FM images of the 11mm EDM at different centre frequencies. These two images give a very good indication of the EDM notch, however, there are also some strong artefacts, i.e. the 'side bars' near the main indication, which were consistent with our numerical examples (see Fig. 4.8(e) and Fig. 4.8(f)) and were considered to have been introduced by using the FMC subtraction to remove the backwall reflection. Fig. 4.12(c) and Fig. 4.12(d) are the TFM images based on the experiment data acquired by two different array probes. It can be seen from Fig. 4.12(c) that the amplitude of the artefacts introduced by the noise is comparable to the tip indication, which makes the sizing of the notch difficult if the real location and shape of the defect is unknown in advance.

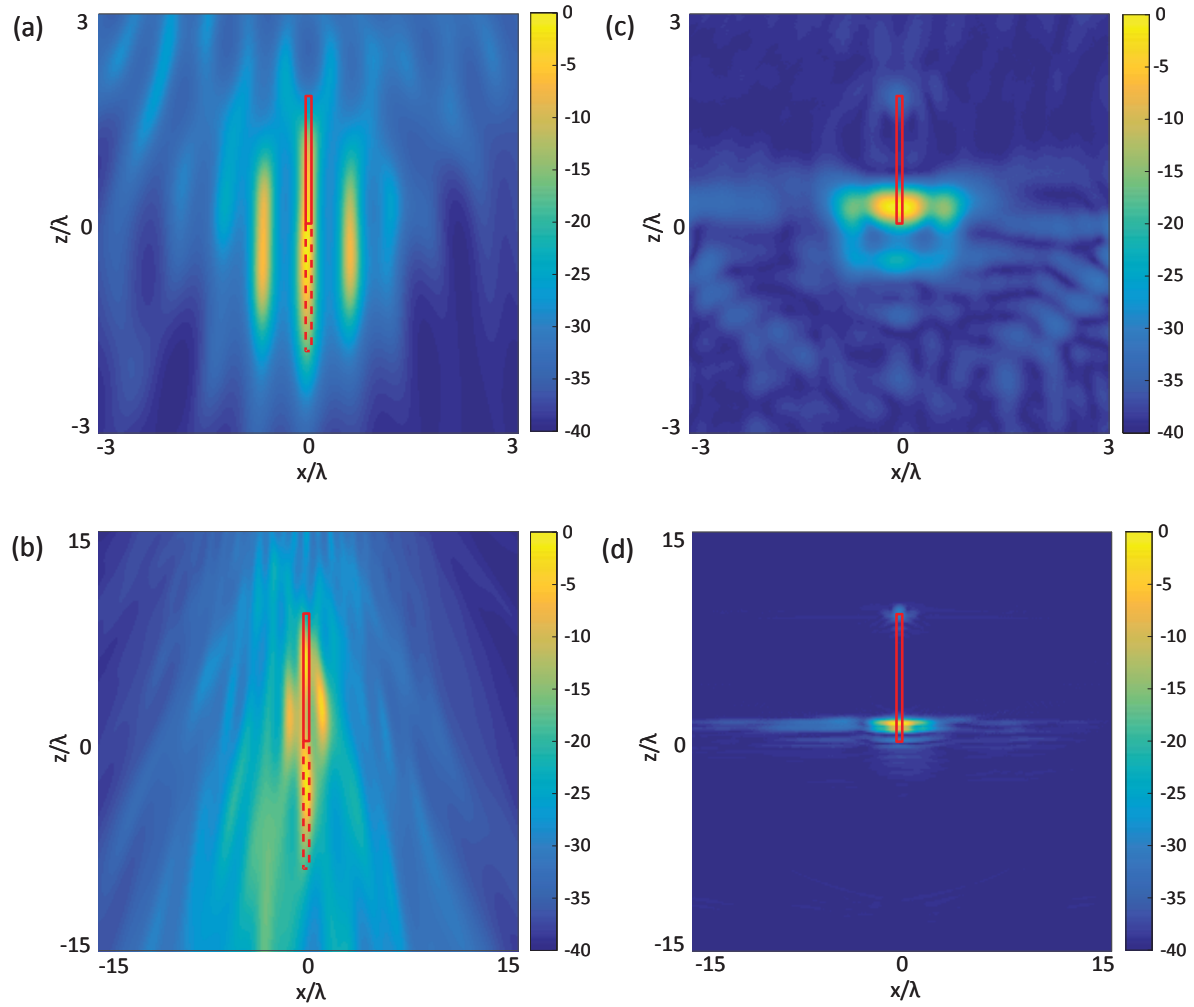


Figure 4.12: The imaging results of the TFM and the FM based on the experiment data acquired by two different array probes: (a) FM image with a 1MHz centre frequency; (b) FM image with a 5MHz centre frequency; (c) TFM image with a 1MHz centre frequency; (d) TFM image with a 5MHz centre frequency. Note that the EDM notch is labelled in the images. The FMC subtraction was used to remove backwall reflections The results here were from experimental data.

Table 4.2: FM and TFM sizing results based on the FMC subtraction - the true notch size is 11mm

	1MHz probe	5MHz probe
FM algorithm	13.7mm	36.4mm
TFM algorithm	10.0mm	9.7mm

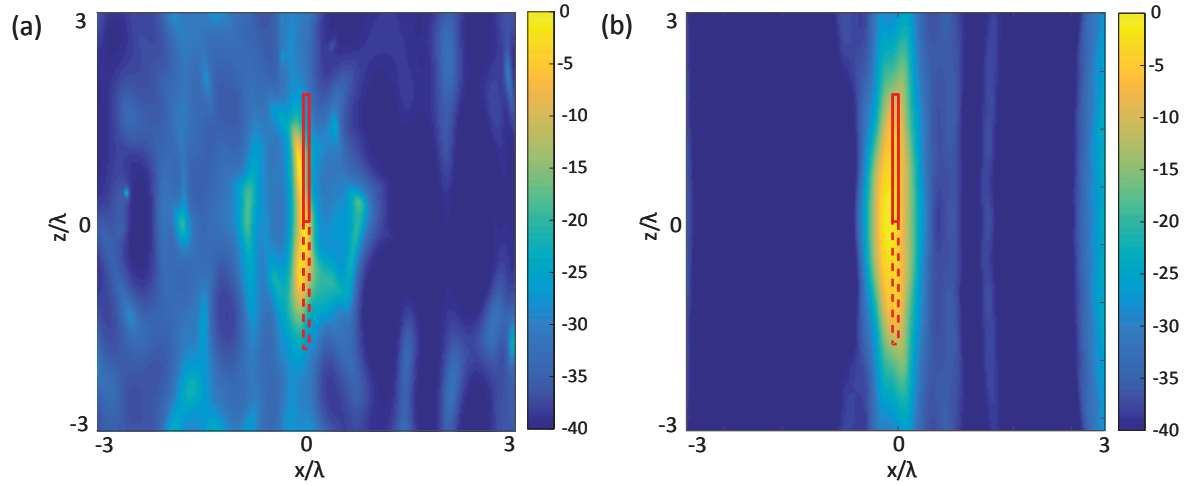


Figure 4.13: The imaging results of the FM based on the experimental data acquired by two different array probes: (a) FM image with a 1MHz centre frequency; (b) FM image with a 5MHz centre frequency. Note that the EDM notch is labelled in the images. The truncation method together with the mirror enhancement were used to eliminate the backwall effects.

The sizing results from these images are shown in Table 4.2. We can see that the FM algorithm gives us a good estimation of the notch depth at 1MHz but fails to provide an accurate estimation at 5MHz, which is because for the 5MHz probe, the small notch assumption of the FMC subtraction is not valid. These sizing results, based on the FM images, shows a very good consistency with the simulation results. TFM provides us an accurate estimation of the notch depth at both 1MHz and 5MHz. However, for the TFM image with a centre frequency of 1MHz, to size the defects prior knowledge is needed about the type of the defect, as the tip indication can easily be masked by the artefacts. Additionally, FM overestimated the notch depth while TFM underestimated the notch depth.

After that, the performance of FM with the backwall effects eliminated by the truncation method together with the mirror enhancement was also experimentally validated. In this case, the original FMC data was directly used for the calculations of the FM images. These imaging results are shown in Fig. 4.13.

These two images also provide an acceptable reconstruction of the EDM notch and are in consistent with the simulation results (Fig. 4.8). It can be seen that the background noise in these experimental images is much stronger than the simulation results, which is because the experimental data contains not only the longitudinal wave but also the

Table 4.3: FM sizing results based on the truncation method - the true notch size is 11mm

1MHz probe	5MHz probe
11.1mm	12.1mm

shear wave and the mode conversions between the longitudinal wave and shear wave. The sizing results based on these images with the -15dB criterion are given in Table 4.3. These indicate that using the FM together with the truncation method and the mirror enhancement is able to provide an accurate sizing for a notch whose depth is not smaller than 1λ, although the sizing error will become larger with an increase in the notch depth.

Although the aperture difference between the 1MHz array and the 5MHz array is not considered here, both the 1MHz array and the 5MHz array have successfully detected and imaged the surface-breaking notch, which implies that the aperture sizes of these two arrays are enough for imaging small defects with relative simple shape (crack-like). In [93], Humeida et al. has successfully imaged and sized small embedded notches (3mm depth) using TFM based on the data from a 7MHz array with a small aperture size of 20.2mm. Also, Hutt et al. [75] have studied the effect of aperture size on using TFM and FM to image kite-shape voids and have found that FM is able to image a near surface kite-shape void with an aperture size of 80°. Hence it will be helpful to investigate the influence of the aperture size on the effectiveness of using FM to image surface-breaking notch and to find the minimum aperture size that can ensure a clear FM image when imaging a surface-breaking notch in the future.

4.5 Conclusions

Previous work on the Factorization Method for NDE was mainly concerned with the super resolution effect [39, 40, 64, 92], but rarely addressed specific applications. This chapter investigated the application of the FM algorithm to the subsurface imaging of the surface-breaking notches. To evaluate the performance of the FM algorithm directly, the widely used imaging algorithm, the TFM algorithm, was used as a reference. The main challenge of this application of the FM algorithm is that the backwall will introduce a strong reflection which will mask the presence of the notch while imaging. In this chapter,

the performance of the FM algorithm with different methods to eliminate backwall effects was tested in the case of surface-breaking notches.

Firstly, the TFM algorithm and the FM algorithm were applied to the simulated data and their performance were compared under different values of notch depth and noise level. Through the comparison, we found that the FM algorithm is able to correctly detect and accurately size a notch whose depth is not smaller than 1λ, while the smallest notch that the TFM can reliably be applied to is 2λ. Additionally, the FM algorithm also gives good noise robustness as the FM algorithm is able to provide a sharp indication of the notch and an accurate sizing result under a high noise level ($SNR = 5dB$).

The effects of the FMC subtraction approach were also studied through simulation. Through all the imaging and sizing results, the best performance of FMC subtraction can be achieved when the notch depth is between 1λ and 3λ. Furthermore, the effects of the employment of the truncation method and the mirror enhancement were also studied through numerical experiments. By employing this method, FM is able to directly reconstruct a clear indication of the surface-breaking notch without any artefacts. The best performance of this method was also achieved when the notch depth is not shorter than 1λ.

After performing these simulations, FM with FMC subtraction and FM with the truncation method were applied to experimental data. The results showed good consistency with the simulations. From this, we found that the FM algorithm is able to image and size small surface-breaking notches.

The work in this chapter also verifies the possibility of the Factorization Method as an alternative to the Total Focusing Method for phased array imaging. The present work is to our mind a significant step toward the application of the Factorization Method to an experimental phased array imaging system.

Chapter 5

Novel imaging algorithms for imaging near backwall defects using FMC data

5.1 Introduction

This thesis has so far applied TFM, HSTFM and FM to the imaging of the near backwall defects and also developed a specific sizing method to measure the depth of surface-breaking notches based on the FM image. It should be possible to further extend the applicability and effectiveness of ultrasonic arrays in imaging near backwall defects by extending the current library of imaging algorithms.

With the development and application of inverse scattering theory and computing technology, the imaging algorithms developed for phased array imaging have advanced significantly in recent years. For example, a different type of sampling method, which is called the Direct Sampling Method (DSM) was proposed in [94] in order to provide effective retrieval of the location and geometrical features of scatterers. The DSM shares the same basic idea with other non-iterative sampling methods (e.g. LSM [46], FM [37] and Time-Reversal Multiple Signal Classification (TR-MUSIC) [95]), that is to design an indicator function which has high values for sampling points inside the scatterer and low values outside. In addition, an innovative imaging algorithm called the Fast Topological Imaging has also been developed [30]. Different from the BF algorithms and 'sampling' type algorithms, this method is actually developed from a mathematical optimization

method based on the topological sensitivity analysis [96].

This chapter aims to extend the current library of imaging algorithms in order to extend the applicability of ultrasonic array imaging. Thus, the DSM and FTIM algorithms are applied to the ultrasonic array imaging of defects in this chapter. The effectiveness of these two imaging algorithms is tested with both simulated and experimental array data, and their performance is examined in terms of the ability to reconstruct different types of defects and the robustness to noise. The remainder of this chapter is organised as follows. Firstly, an overview of the background theory and some brief derivations of the proposed imaging algorithms are provided. Then, the effectiveness of the proposed imaging algorithms for ultrasonic array imaging is tested through several numerical examples. Here, the influence of defect type and added noise is also examined. After that, some experimental results based on the near backwall defects are shown and the performance of the proposed imaging algorithms is discussed.

A paper reporting the work of this chapter is in preparation [P3].

5.2 Background theory of the imaging algorithms

5.2.1 Direct Sampling Method

Similar to the Factorization Method, the idea of the Direct Sampling Method (DSM) is also to construct an indicator function whose value will change dramatically from inside the scatterer to the outside. Recall the scattering theory which has been introduced in Chapter 2. According to [97] and [98], for any two points $\boldsymbol{r_j}$ and $\boldsymbol{r_p}$ inside the sampling domain Ω, it is true that

$$\int_{\mathbb{S}^1} G_\infty(\hat{\boldsymbol{r}}, k; \boldsymbol{r_j})\overline{G_\infty(\hat{\boldsymbol{r}}, k; \boldsymbol{r_p})}ds(\hat{\boldsymbol{r}}) = C\Im(G(\boldsymbol{r_p}, k; \boldsymbol{r_j})) \tag{5.1}$$

where $\mathbb{S}^1$ denotes the unit circle in $\mathbb{R}^2$, C is a constant, depending only on the wave number k and $\Im$ refers to the imaginary function which returns the imaginary coefficient of a complex number. According to [94], the right-hand side term $C\Im(G(\boldsymbol{r_p}, k; \boldsymbol{r_j}))$ has

the following behaviour

$$C\Im(G(\boldsymbol{r_p}, k; \boldsymbol{r_j})) = J_0(k|\boldsymbol{r_p} - \boldsymbol{r_j}|), \tag{5.2}$$

where J_0 is Bessel function of the first kind. Then, the sampling domain which encloses the scatterer D is divided into a set of small squares $\{\tau_j\}$. By using the rectangular quadrature rule, Eq. (2.30) can be approximated as

$$u_\infty(\hat{\boldsymbol{r}}, k; \hat{\boldsymbol{r}}_0) = -k^2 \int_D O(\boldsymbol{r}') u(\boldsymbol{r}', k; \hat{\boldsymbol{r}}_0) G_\infty(\hat{\boldsymbol{r}}, k; \boldsymbol{r}') d\boldsymbol{r}' \approx k^2 \sum_{j=1}^{N} w_j G_\infty(\hat{\boldsymbol{r}}, k; \boldsymbol{r_j'}) \tag{5.3}$$

where $\boldsymbol{r_j'}$ is the location of the centre of small square τ_j, N denotes the total number of small squares and the weight w_j depends on $O(\boldsymbol{r})u(\boldsymbol{r}, k; \hat{\boldsymbol{r}}_0)$ and the area of small square τ_j. By using Eq. (5.1) and Eq. (5.3), it is easy to obtain

$$\int_{\mathbb{S}^1} u_\infty(\hat{\boldsymbol{r}}, k; \hat{\boldsymbol{r}}_0) \overline{G_\infty(\hat{\boldsymbol{r}}, k; \boldsymbol{r_p})} ds(\hat{\boldsymbol{r}}) \approx k^2 C \sum_{j=1} w_j \Im(G(\boldsymbol{r_p}, k; \boldsymbol{r_j})). \tag{5.4}$$

Considering Eq. (5.2), the right-hand side term of Eq. (5.4) will remain constant when $\boldsymbol{r_p}$ is close to some point scatterer $\boldsymbol{r_j}$ but will decay dramatically when $\boldsymbol{r_p}$ moves away from $\boldsymbol{r_j}$ [94], as shown in Fig. 5.1.

Motivated by this behaviour, an indicator function was developed for the Direct Sampling Method for any point $\boldsymbol{z}$ inside the sampling domain [99]. Based on the limited aperture data, the indicator function of DSM is given by

$$I_{DSM}(\boldsymbol{z}, k) = \int_\Gamma \int_\Gamma \frac{G_\infty(\hat{\boldsymbol{r}}, k; \boldsymbol{z}) u_\infty(\hat{\boldsymbol{r}}, k; \hat{\boldsymbol{r}}_0)}{||G_\infty(\hat{\boldsymbol{r}}, k; \boldsymbol{z})|| \cdot ||u_\infty(\hat{\boldsymbol{r}}, k; \hat{\boldsymbol{r}}_0)||} ds(\hat{\boldsymbol{r}}) ds(\hat{\boldsymbol{r}}_0), \tag{5.5}$$

where Γ denotes some subset of $\mathbb{S}^1$ in the case of limited aperture. The Multiple-frequency Direct Sampling Method (MDSM) was developed in [100] in order to compensate a lack of incident directions of the incident waves, i.e. limited aperture data. The indicator function of MDSM is written as:

$$I_{MDSM}(\boldsymbol{z}) = \int_{k_1}^{k_M} \int_\Gamma \int_\Gamma \frac{G_\infty(\hat{\boldsymbol{r}}, k; \boldsymbol{z}) u_\infty(\hat{\boldsymbol{r}}, k; \hat{\boldsymbol{r}}_0)}{||G_\infty(\hat{\boldsymbol{r}}, k; \boldsymbol{z})|| \cdot ||u_\infty(\hat{\boldsymbol{r}}, k; \hat{\boldsymbol{r}}_0)||} ds(\hat{\boldsymbol{r}}) ds(\hat{\boldsymbol{r}}_0) ds(k). \tag{5.6}$$

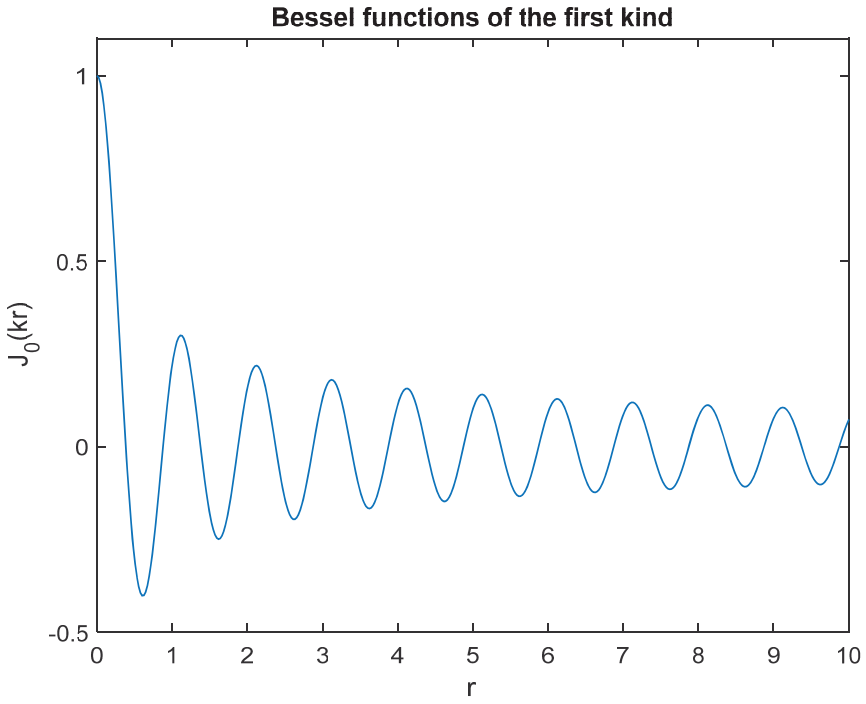


Figure 5.1: Decay patterns of $C\Im(G(\boldsymbol{r_p}, k; \boldsymbol{r_j}))$ as $r = |\boldsymbol{r_p} - \boldsymbol{r_j}|$ when $k = 2\pi$.

The computational implementation of DSM is convenient as only simple operations such as the inner product are involved in this method, which contrasts with the Factorization Method or the Linear Sampling Method which uses Singular Value Decomposition first to calculate the singular system of the far-field operator. It has been proved in [94, 99–101] as a fast and effective tool for providing reliable estimations of positions and shapes of unknown scatterers.

5.2.2 Time Domain Sampling Method

To facilitate the following formulation, we have defined the time-reversed scattered data by

$$U^{tr}(\boldsymbol{x_r}, t; \boldsymbol{x_t}) = \begin{cases} U^s(\boldsymbol{x_r}, T - t; \boldsymbol{x_t}), & 0 \leq t \leq T, \\ 0, & t < 0, \end{cases} \tag{5.7}$$

if the time domain scattered data $U^s(\boldsymbol{x_r}, t; \boldsymbol{x_t})$ is given, where $\boldsymbol{x_t} \in \Gamma_i$ is the location of the transmitter, $\boldsymbol{x_r} \in \Gamma_i$ is the location of the receiver and Γ_i is the surface where the

array located. It should be noted that U^s is the time domain equivalent of u_∞. Inspired by the frequency domain sampling methods [99, 101], Guo et al [102] developed the Time Domain Sampling Method as a strengthened TFM. Assuming the time-reversed scattered data U^{tr} is given, the indicator function of TDSM is given by

$$I_{TDSM} = \int_0^T \int_{\Gamma_i} \left(\int_{\Gamma_i} U^{tr}(\boldsymbol{x_r}, \tau - \frac{|\boldsymbol{z} - \boldsymbol{x_r}|}{c_0}; \boldsymbol{x_t}) ds(\boldsymbol{x_r}) \right)^2 ds(\boldsymbol{x_t}) d\tau. \tag{5.8}$$

By comparing Eq. (5.8) and Eq. (5.6), one can see that the TDSM is actually the DSM in time domain. The TDSM also shares the same essential requirement of the imaging scheme of the FM, which is to find a spatial varying indicator function which has a significant difference in values for points inside and outside the scatterer. In fact, the indicator function of the TDSM (Eq. (5.8)) is also similar to the indicator function of the TFM (Eq. (2.50)), but the indicator (Eq. (5.8)) has an integration over the recording time T and a square of the integrand, thus, Guo et al. [102] believe that these differences in indicator function will help the TDSM to achieve a better performance over the standard TFM. Although the theory behind the TDSM is only partially resolved, the TDSM has already been implemented on imaging point-like scatterers and regular-size notches, and achieved satisfactory results on these applications [102]. Here, this method will be applied to the limited view far-field measurements, although this method was initially developed for the transient acoustic near-field measurements.

5.2.3 Fast topological imaging

The Fast Topological Imaging (FTIM) method is based on the topological sensitivity methods [103–109], thus, a brief introduction of the topological sensitivity methods is helpful to understand the FTIM. The topological sensitivity methods are developed from shape optimization mathematics and they create images in an equivalent virtual domain to allow a reconstruction of the reflective objects in the medium through mathematical tools. These images are created from an optimization process based on the experimental data and the virtual domain is defined by the experimental conditions (elastic properties, density and possibly the geometry). Generally, a cost function is used for the optimization

process and the reflective objects are located where this cost function is minimized. To represent the image of the objects, the mathematical variable can either be the analytically obtained topological derivative [110] or the topological energy [104], and in the latter case, the expression is more simplified and more general.

The topological sensitivity analysis method defines two problems to be solved [30]: the direct problem and the adjoint problem. In the case of array imaging, these two problems correspond to the virtual propagation of two different sets of waves emitted at the location of the array in the virtual domain based on the incident field and the experimental data. It should be noted that the virtual domain used here is semi-infinite and defect-free, and the virtual domain used in the direct problem should be the same as the virtual domain used in the adjoint problem.

From an applicative point of view, solving the direct and adjoint problems consist of (i) emitting waves into the medium under inspection and measuring the related scattered field using an ultrasonic array; (ii) solving two virtual propagation problems (direct and adjoint) in the virtual domain through numerical computation; (iii) computing the image based on the two wave fields obtained in step (ii). It should be noted that the direct and adjoint problems in step (ii) consist of the same propagation problem with two different emitted sources. In the direct problem, the emitted source is the incident source used in the experimental measurement, while in the adjoint problem, the emitted source is the time reversed experimentally measured scattered fields [30]. In the case of the FTIM, only the first iteration of the optimization process is performed, this is because the imaging results obtained from the first iteration is already satisfactory. The imaging schema of the FTIM is shown in Fig. 5.2.

In the FTIM method, the direct problem and the adjoint problem are solved in the frequency domain in order to perform a fast and flexible calculation. Before the calculations of the direct problem and the adjoint problem, the 2D radiation pattern H_j of the transducer j in the virtual domain should be calculated first, where $1 \leq j \leq N$ and N is the number of array elements. The radiation pattern can be calculated either numerically or analytically if the propagation model of the given medium is available, and for a given medium, the radiation pattern need only be calculated once. For example, in a 2D homogeneous fluid medium, the propagation of the wave can be described by the Helmholtz

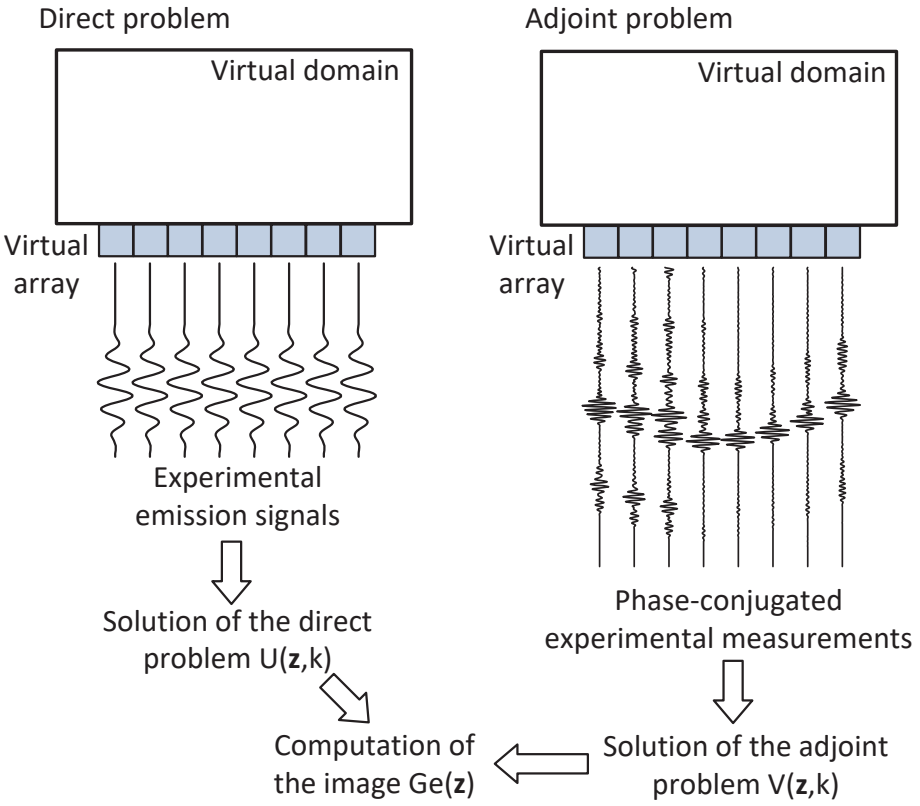


Figure 5.2: The imaging schema of the Fast Topological Imaging. Note that the signals are plotted in the time domain for clarity.

equation and the radiation pattern of the wave can be described by the analytical Green function [45] such as

$$G(r) = -\frac{i}{4} H_0^{(1)}(kr) \tag{5.9}$$

where $H_0^{(1)}$ represents the zero order Hankel function of the first kind, r is the distance from the source to the observation point and k is known as the wave number. After that, the solutions U and V of the direct problem and the adjoint problem respectively can be calculated by multiplying the 2D radiation pattern of each transducer with the Fourier transformed signals emitted in the virtual domain and summing up all the fields

corresponding to each transducer:

$$U(\boldsymbol{z},k)=\sum_{j=1}^{N}H_j(\boldsymbol{z},k)S_j(k), \tag{5.10}$$

$$V(\boldsymbol{z},k)=\sum_{j=1}^{N}H_j(\boldsymbol{z},k)M_j^*(k), \tag{5.11}$$

where k is the wave number, S_j is the Fourier transformed signals of the experimental signals excited by the transducer j in the direct problem, M_j is the Fourier transformed signals of the signal measured by the transducer j in the experimental inspection and the $*$ symbol represents the complex conjugation and H_j refers to the 2D radiation pattern of transducer j. For a given medium, assuming the 2D radiation pattern has already been calculated, the calculation of the image based on a new measurement only requires the mathematical operations in Eq. (5.10) and Eq. (5.11). No further physical modelling is needed for the calculation of the FTIM image.

The solutions of the direct problem and the adjoint problem allow the calculation of the topological gradient [96], which will depend on the type of inhomogeneity considered. Performing an integration of the topological gradient over the frequency domain will lead to an image of the medium with the difference between the experimental medium and the virtual (i.e. undamaged in an NDE contact) medium emphasized. In order to define a more general method that can be adapted to different inhomogeneities, a more simplified and generic definition of the topological gradient is used in the FTIM method, which is given by:

$$\begin{aligned}\mathcal{G}(\boldsymbol{z})&=\int_{\mathbb{R}}U(\boldsymbol{z},k)V(\boldsymbol{z},k)dk\\&=2\mathfrak{R}(\int_{\mathbb{R}^+}U(\boldsymbol{z},k)V(\boldsymbol{z},k)dk).\end{aligned} \tag{5.12}$$

where $\mathfrak{R}$ refers to the real function that which returns the real coefficient of a complex number. Also, the topological gradient can be defined on a discrete frequency domain

$[k_1, \ldots, k_M]$ as $\mathfrak{R}(G(\boldsymbol{z}))$, where the definition of $G(\boldsymbol{z})$ is given by:

$$G(\boldsymbol{z}) = \sum_{i=1}^{M} U(\boldsymbol{z}, k_i) V(\boldsymbol{z}, k_i). \tag{5.13}$$

In the FTIM method, the image of the experimental medium can be represented by plotting the topological gradient with respect to space such as

$$G_e(\boldsymbol{z}) = |G(\boldsymbol{z})|. \tag{5.14}$$

According to [96], in order to increase the resolution of the FTIM, another formulation of the image is suggested, which is given by:

$$G(\boldsymbol{z}) = \sum_{i=1}^{M} \frac{U(\boldsymbol{z}, k_i) V(\boldsymbol{z}, k_i)}{|U(\boldsymbol{z}, k_i)|^2}. \tag{5.15}$$

In the case of the FMC data, assuming that the array has N elements, the FMC data actually contains $N \times N$ measurements, i.e. N experimental inspections. Thus, based on the N measurements, N images can be obtained through the FTIM. Then, the final image is the mean value of the N images obtained. It might be helpful to study variance of the N images rather than only the mean in the future.

5.3 Numerical simulation

In this section, several 2D numerical examples are given to demonstrate the effectiveness of the proposed imaging methods when used as post-processing algorithms for ultrasonic array imaging. The scattered data were generated through numerical simulations using the finite element models created in Abaqus (Dassault Systemes Simulia Corp., Providence, RI). The properties of these 2D models are assumed to be uniform out of the plane and the material used is isotropic steel with a density of $7700 kg/m^3$, a Young's modulus of $195 GPa$ and a Poisson ratio of 0.28. The element used is the 4-node bilinear plane strain quadrilateral. For simplicity, absorbing layers were attached to the model to approximate an unbounded exterior domain [77], however, the backwall was kept in the model to

approximate the practical inspection conditions. As the derivations in this paper are based on the acoustic waves which are a type of longitudinal wave and the shear wave and mode conversions always arrive later than the longitudinal wave, only longitudinal waves were excited and recorded [76]. The ultrasound was excited by a 64 element array with an element pitch of 0.5λ and the wave generated by this array set to be a 5 cycle Hann windowed tone burst with a 2MHz central frequency. Therefore, the wavelength λ of the longitudinal wave was approximately 3mm. In the following sections, in order to ensure convenient comparison, the amplitude of the imaging result is normalized to the maximum value in each image and the images are scaled to the range of [0,1] if not otherwise specified.

5.3.1 Reconstruction of point scatterers

Firstly, the proposed imaging algorithms were used to reconstruct point scatterers based on the simulated array data. Fig. 5.3(a) shows the schematic of an FE model which contains two well-resolved targets. The linear array was placed at a distance of 20λ from the backwall and the array and the backwall are parallel. The two point scatterers were separated by 0.5λ and located at a distance of 10λ from the array. These two point scatterers should be well-resolved as the distance between these two point scatterers is equal the Rayleigh limit (0.5λ). The Rayleigh limit is actually the resolution limit of conventional Beamforming algorithms [39]. To ensure they behave as point scatterers, the diameter of each scatterer was set to be 0.2λ.

Based on this model, the Full Matrix Capture (FMC) data was captured. The FMC data is obtained by using each element to excite ultrasound waves in turn, which is then measured by all of the elements in the array, thus, a complete data set can be captured. The simulated array data based on this model contained the scattered signal from the defects and the reflection from the planar backwall. Here, in order to focus on the study about the performance of different imaging algorithms, baseline subtraction was used to extract the pure defect signal. The baseline subtraction algorithm extracts the scattered field by measuring the total field of a defect-free copy of the component, then, the pure defect signal can be extracted through a simple subtraction. Additive white Gaussian

noise with a SNR of 20dB was then added to the pure defect signal. The SNR is defined by (cf. [16])

$$SNR = 20log_{10}\frac{Q_{\text{signal peak}}}{\delta_{\text{noise RMS}}} \tag{5.16}$$

where $Q_{\text{signal peak}}$ is the peak amplitude of defect signal and $\delta_{\text{noise RMS}}$ is the RMS value root-mean-square (RMS) magnitude of the noise. Thus, 20dB SNR corresponds to noise with a RMS magnitude of 10% of the RMS magnitude of the defect signal.

Fig. 5.3(b) and (c) give the reconstructions of the well-resolved point scatterers based on Direct Sampling Method (DSM) and Multi-frequency Direct Sampling Method (MDSM), respectively. As can be seen from Fig. 5.3(b) and (c), strong indications which represent two point scatterers can be clearly visualized in both of the images. Furthermore, it is clear that both DSM and MDSM accurately estimate the location of the point scatterers, which is in accordance with our theoretical analysis. From Fig. 5.3(b), it can be seen that there are ripples near the main indications of the point scatterers, which increases the variation of the image and raises the risk of falsely judging the type of the defect. By comparing the Fig. 5.3(b) and (c), it is clear that Fig. 5.3(c) contains fewer ripples than Fig. 5.3(b), which suggests that the multiple-frequency version algorithm is able to provide a more stable reconstruction (fewer artefacts) of the point scatterers. This is because the multiple-frequency information is able to compensate for some of the information missing in the limited aperture data.

Fig. 5.3(d) shows the imaging result based on the Time Domain Sampling Method (TDSM). Since the TDSM uses the time domain data that also contains multiple-frequency information, it also provides a more clear image than the DSM (see Fig. 5.3(b) and (d)). However, the MDSM or the TDSM didn't show an obvious improvement in reconstruction as the main indications in Fig. 5.3(c) (or Fig. 5.3(d)) are quite close to Fig. 5.3(b). This is because the multiple-frequency information can only partly compensate for the information loss in limited aperture data, thus the multiple-frequency version algorithm is not required to produce a better reconstruction than the single-frequency version. A similar phenomenon was observed by Y. Guo et al. in [111], in which the performance of single-frequency LSM, multiple-frequency LSM and time domain LSM were compared

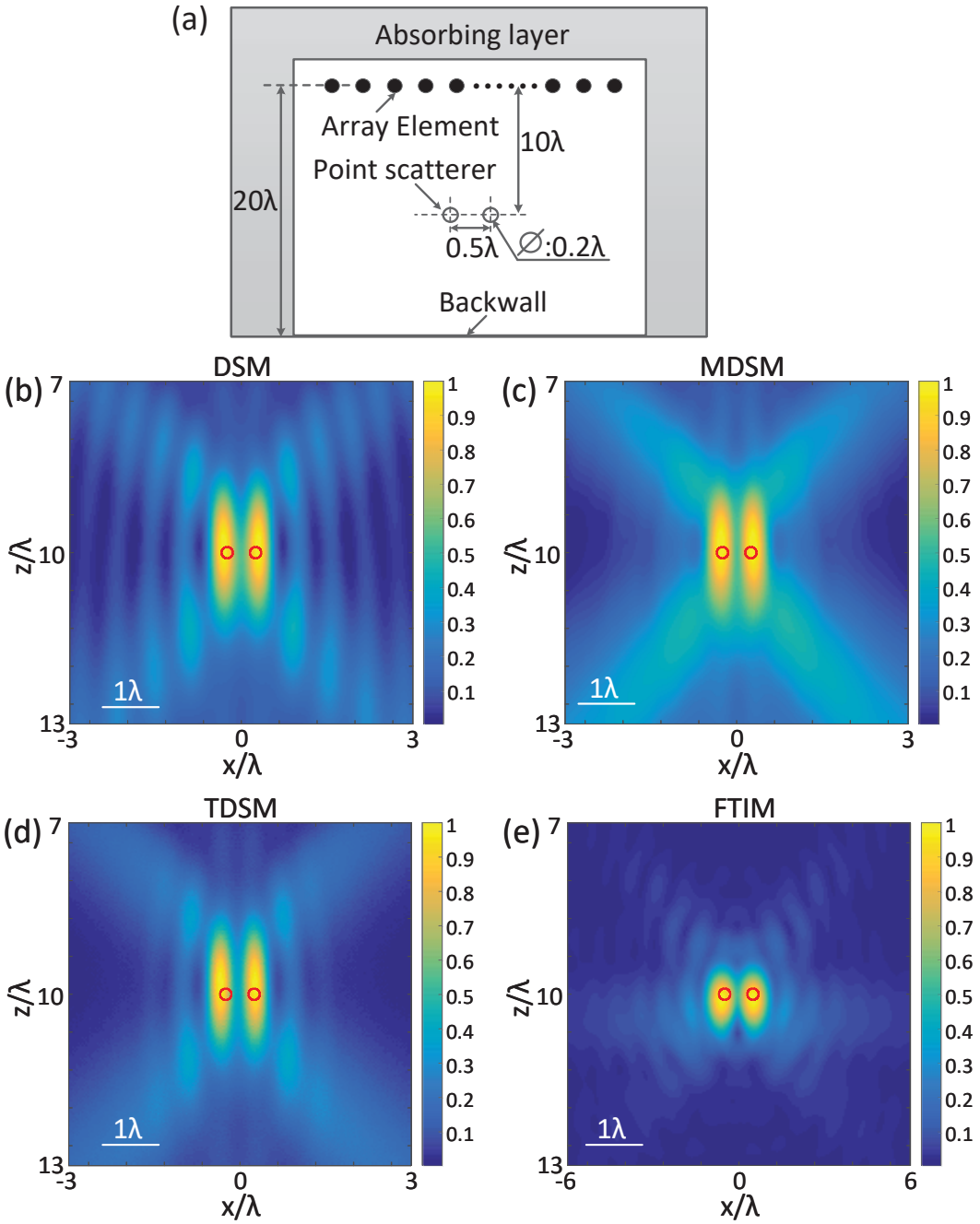


Figure 5.3: (a) Schematic of the FE model containing two well-resolved point scatterers (not to scale). (b) DSM image of two well-resolved point scatterers at the central frequency 2MHz, (c) MDSM image of two well-resolved point scatterers using 10 uniformly distributed frequencies between 1.5MHz and 2.5MHz, (d) TDSM image of two well-resolved point scatterers using time domain data, (e) FTIM image of two well-resolved point scatterers using a 35kHz frequency step between 1.5MHz and 2.5MHz. Note that the red circles in the images are used to represent the true location and shape of point scatterers. The imaging results here are from simulated data.

based on the same small aperture data, however, the best reconstruction achieved was provided by the single-frequency LSM.

Besides, the FTIM also provided a good reconstructed image of these two scatterers as the two main indications are quite strong and clearly separated (Fig. 5.3(e)). It is also notable that in this image, the two scatterers show less of the vertical elongation present in the other images, which occurs because of the limited aperture. The algorithm may therefore be better suited to limited data situations. Overall, since the indications in the FTIM image are smaller than the indications in DSM images, it suggests that FTIM outperforms DSM for imaging point scatterers.

Following on from the model containing well-resolved point scatterers, a more challenging case was simulated, as shown in Fig. 5.4(a). The point scatterers in this model are poorly-resolved because the distance between them is only 0.4λ, smaller than the Rayleigh limit. The other parameters and properties of this model were kept the same as the model shown in Fig. 5.3(a). Again, the backwall reflection was removed using baseline subtraction and noise was added to achieve a SNR of 20dB.

Fig. 5.4(b) illustrates the performance of DSM in reconstructing two poorly-resolved point scatterers. It can be seen clearly that the DSM also reconstructed two indications with accurate location estimation, however, the two main indications are not well separated and have blurred edges. From Fig. 5.4(b), it is clear that the resolution limit of DSM is 0.5λ, this result is consistent with the study about the resolution limit of DSM in [94]. This is because that the DSM assumes that multiple scattering is weak and thus ignored for multi-component small-scaled scatterers [94].

Similar to the well-resolved point scatterers case, the MDSM or the TDSM also showed a better performance in the reconstruction of the poorly-resolved scatterers than the DSM. The reconstruction of two poorly-resolved point scatterers in Fig. 5.4(c) is slightly better than Fig. 5.4(b) as the edges of the main indications in Fig. 5.4(c) became clearer than the indications in Fig. 5.4(b), although the edges are still blurred in Fig. 5.4(c). This is because for the frequencies higher than 2MHz contained in the multiple-frequency data, the relevant wave would have a shorter wave length than 3mm, e.g. for 2.5MHz, the relevant wavelength is approximately 2.4mm, thus these two point scatterers are not actually poorly resolved at this frequency.

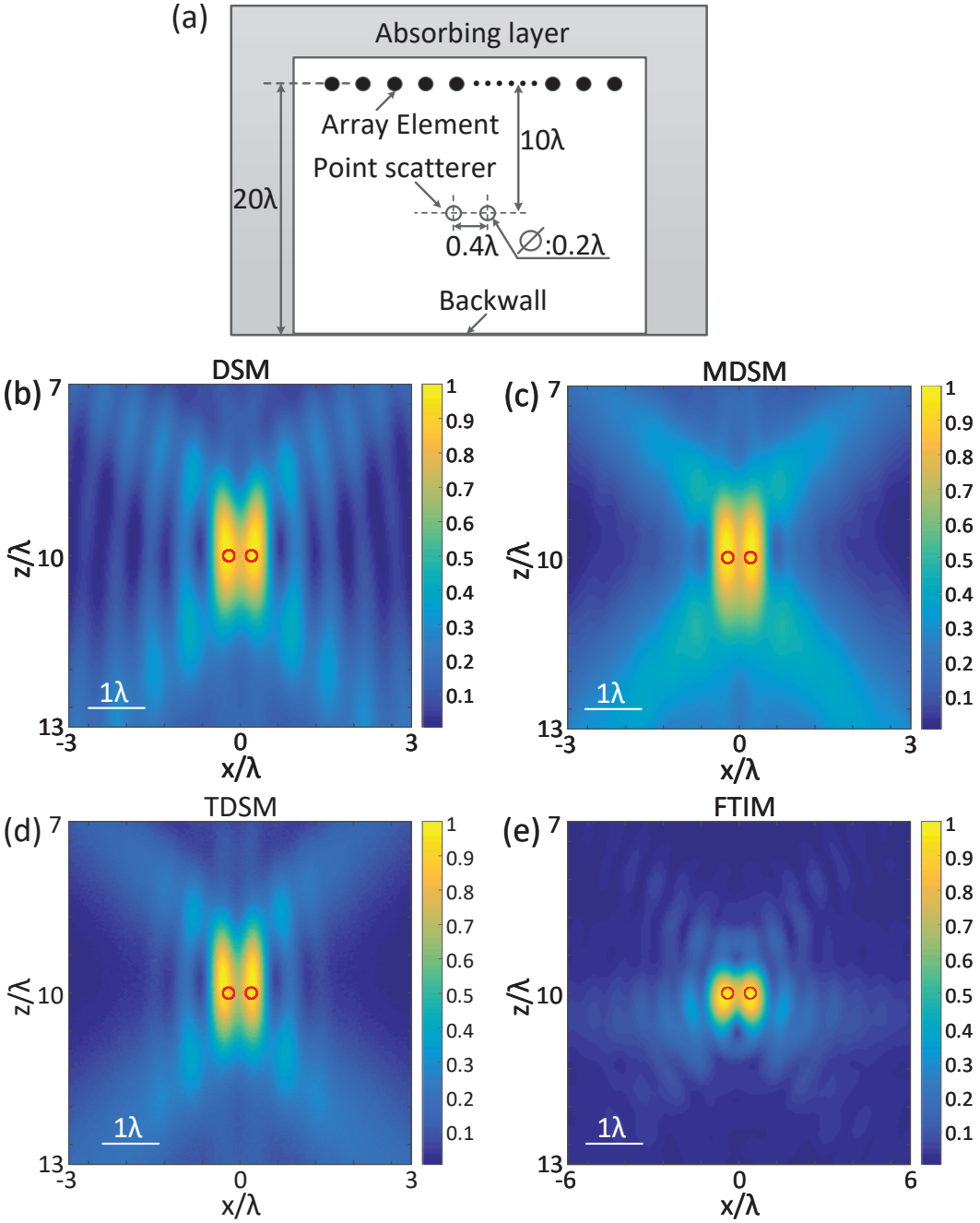


Figure 5.4: (a) Schematic of the FE model containing two poorly-resolved point scatterers (not to scale). (b) DSM image of two poorly-resolved point scatterers at the central frequency 2MHz, (c) MDSM image of two poorly-resolved point scatterers using 10 uniformly distributed frequencies between 1.5MHz and 2.5MHz, (d) TDSM image of two poorly-resolved point scatterers using time domain data, (e) FTIM image of two poorly-resolved point scatterers using a 35kHz frequency step between 1.5MHz and 2.5MHz. Note that the red circles in the images are used to represent the true location and shape of point scatterers. The imaging results here are from simulated data.

The TDSM showed an even better performance than the MDSM, as the two main indications in the Fig. 5.4(d) are more well separated and have clear edges, which is because the time domain data used in the TDSM actually contains all the possible multi-frequency information in the measurements while the multiple-frequency data used in the MDSM contains only part of the multi-frequency information in the measurements.

Although the FTIM also uses the multiple frequency data, it cannot resolve two points scatterers with a distance shorter than 0.5λ (see Fig. 5.4(e)), as the resolution of the FTIM is diffraction limited [30].

5.3.2 Reconstruction of crack-like scatterers

In this section, the proposed imaging algorithms are used to reconstruct crack-like defects, since this is the primary industry interest. Fig. 5.5(a) shows the schematic of an FE model which contains an embedded notch with zero tilt angle, i.e. perpendicular to the array. The direction of the notch is parametrised as tilt angle relative to the vertical. The vertical distance from the linear array to the centre of the notch is set to be 10λ. The other parameters and properties of this model are kept the same as the model shown in Fig. 5.3(a). Again, the backwall reflection was removed using baseline subtraction and noise was added to achieve a SNR of 20dB.

From Fig. 5.5(b), it is clear that DSM accurately reconstructed the location and the shape of the notch. However, the length of the notch was underestimated as the main indication is shorter than the real length of the notch.

The image reconstructed by MDSM, as shown in Fig. 5.5(c), is quite close to the image reconstructed by DSM, and the main indication of it was strengthened when compared to Fig. 5.5(b), this is because the indication function of DSM (Eq. 5.6) contains a sum of single frequency images which acts as an averaging process to reduce artefacts and enhance the main indication. With the help of the multiple-frequency information, the notch length was more precisely estimated in the image generated by the MDSM.

As can be seen from Fig. 5.5(d), the image generated by the TDSM is also quite similar to the image generated by the DSM, but there are fewer artefacts in the image generated by the TDSM.

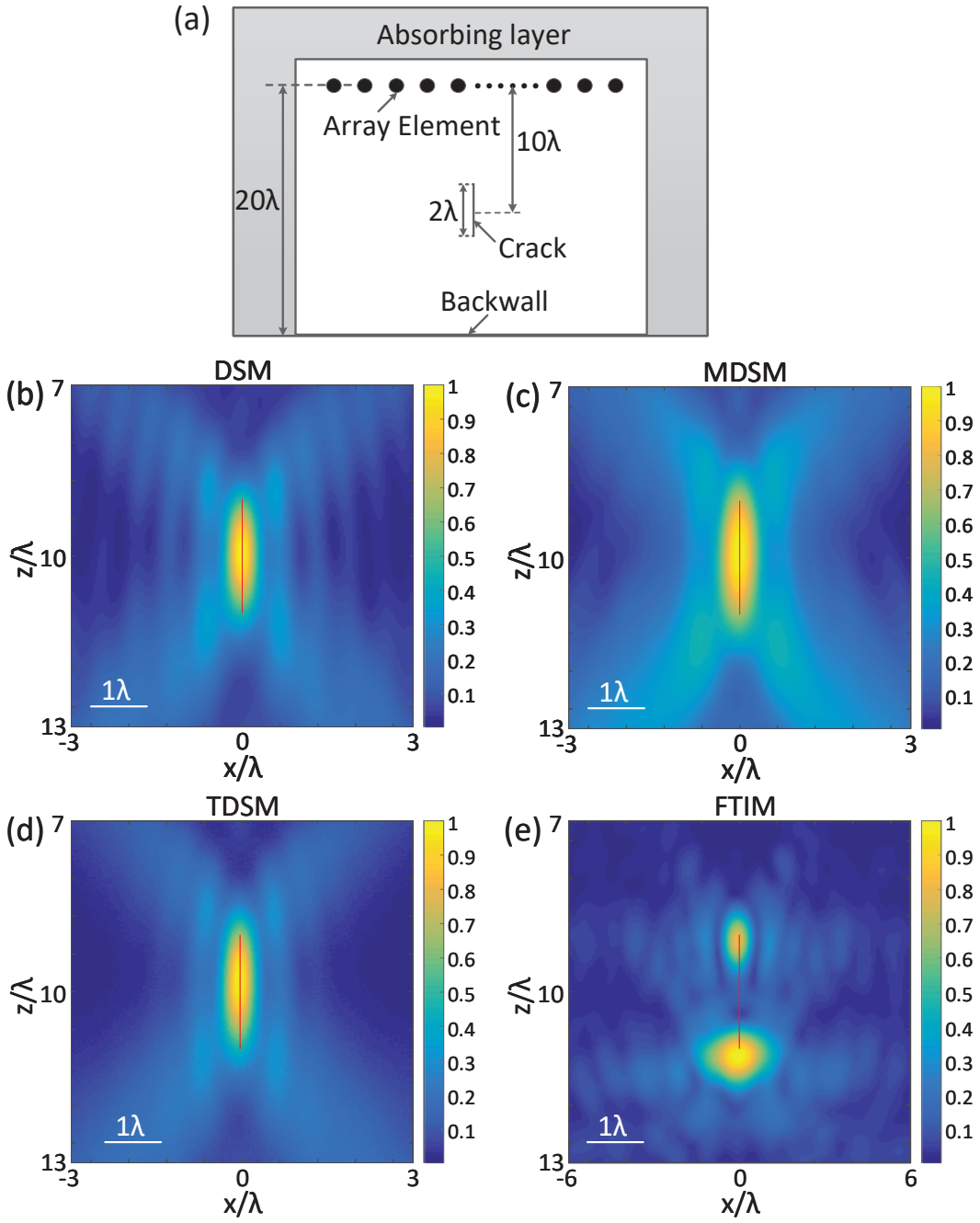


Figure 5.5: (a) Schematic of the FE model containing an embedded notch with zero tilt angle (not to scale). (b) DSM image of a notch with zero tilt angle, (c) MDSM image of a notch with zero tilt angle using 10 uniformly distributed frequencies between 1.5MHz and 2.5MHz, (d) TDSM image of a notch with zero tilt angle using time domain data, (e) FTIM image of a notch with zero tilt angle using a 35kHz frequency step between 1.5MHz and 2.5MHz. Note that the red line in the images is used to represent the true location and shape of the notch. The imaging results here are from simulated data.

Distinct from the DSM methods that reconstructed the shape of the notch, the image reconstructed by the FTIM (Fig. 5.5(e)) only contains two strong indications of the notch tips, which is similar to the image generated by the Total Focusing Method (TFM) when imaging a notch. These two tip indications can help us to achieve an accurate sizing of the notch but may cause difficulty in judging the type of defect.

In Fig. 5.6 we compare the reconstructions of a notch with a tilt angle of 15° using the proposed imaging algorithms. Fig. 5.6(a) shows the schematic of an FE model which contains an embedded notch with a tilt angle of 15°. Except for the tilt angle, all the properties and parameters of the model in Fig. 5.6(a) are the same as the model shown in Fig. 5.5(a). Again, the backwall reflection was removed using baseline subtraction and noise was added to achieve a SNR of 20dB.

In this case, from Fig. 5.6(b), it is clear that DSM provide a very accurate reconstruction which precisely estimated the location, shape, tilt angle and length of the notch. Also, the MDSM and the TDSM also provide good reconstructions of the tilted notch, see Fig. 5.6 (c) and (d). When we further increase the tilt angle of the notch (bigger than 15°), DSM, MDSM and TDSM cannot accurately reconstruct the tilt angle of the notch any longer (See Fig. 5.7). Besides, from Fig. 5.6(e) and Fig. 5.7(e), it is clear that the FTIM is able to reconstruct the tips of the tilted notches.

From the above notch examples, the DSM, the MDSM and the TDSM all showed good performance on the notch with a small tilt angle in location estimation and shape reconstruction. Furthermore, the DSM methods are able to tolerate a tilt angle up to 15°, and the ability to image tilted notches indicate it is suitable for a wide scope of applications in notch detection. Although the FTIM is not able to reconstruct the shape of the embedded notch, the notch tips can still be identified from FTIM images, which allows the estimation of the length and tilt angle of the notch.

5.3.3 Noise robustness

In this section, the noise robustness of the proposed imaging algorithms are examined. The defect signal used here is based on the model containing a notch with zero tilt angle (as shown in Fig. 5.5(a)), then noise was added to achieve two different noise levels:

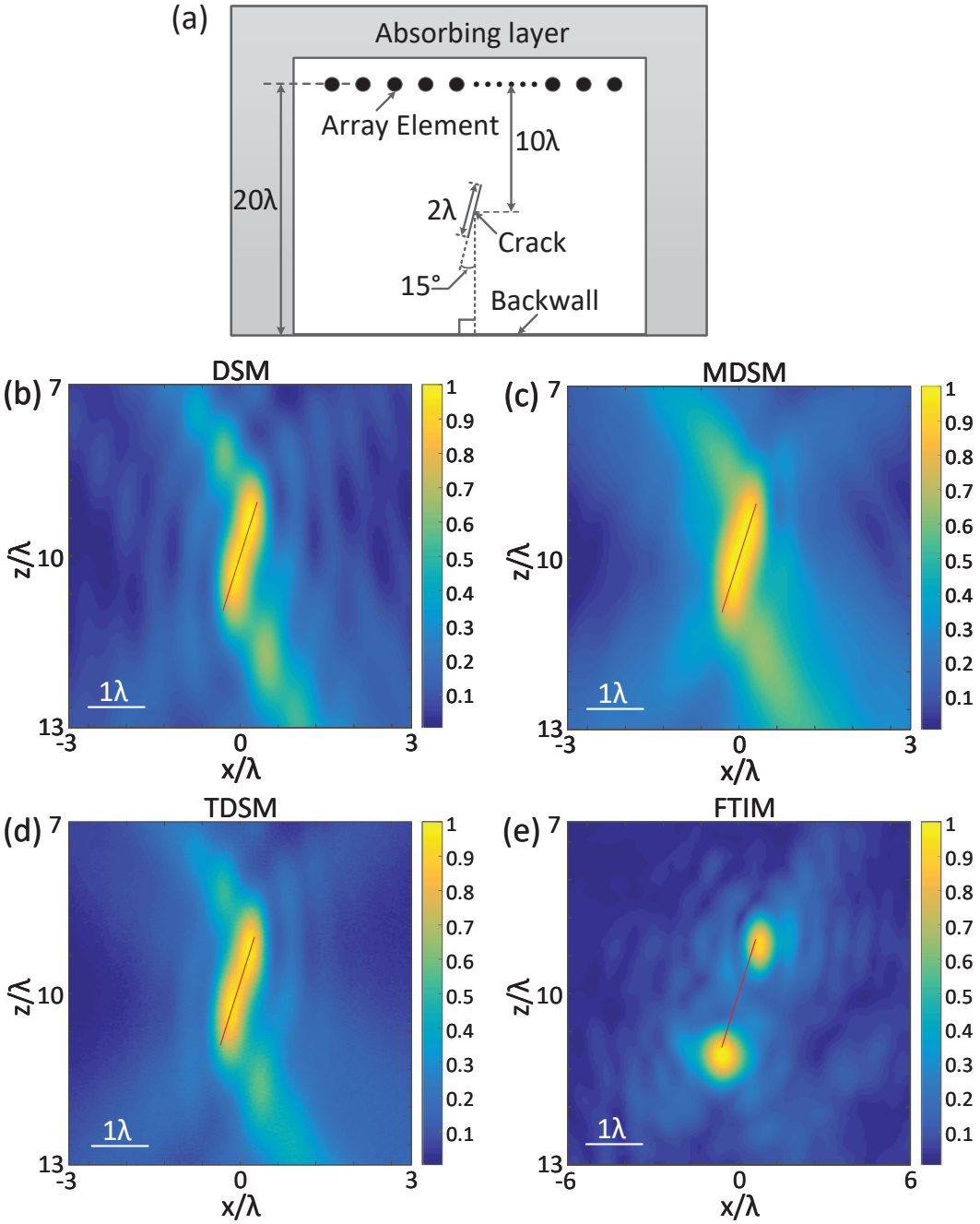


Figure 5.6: All plots as in Fig. 5.5, except for a tilt angle of 15°.

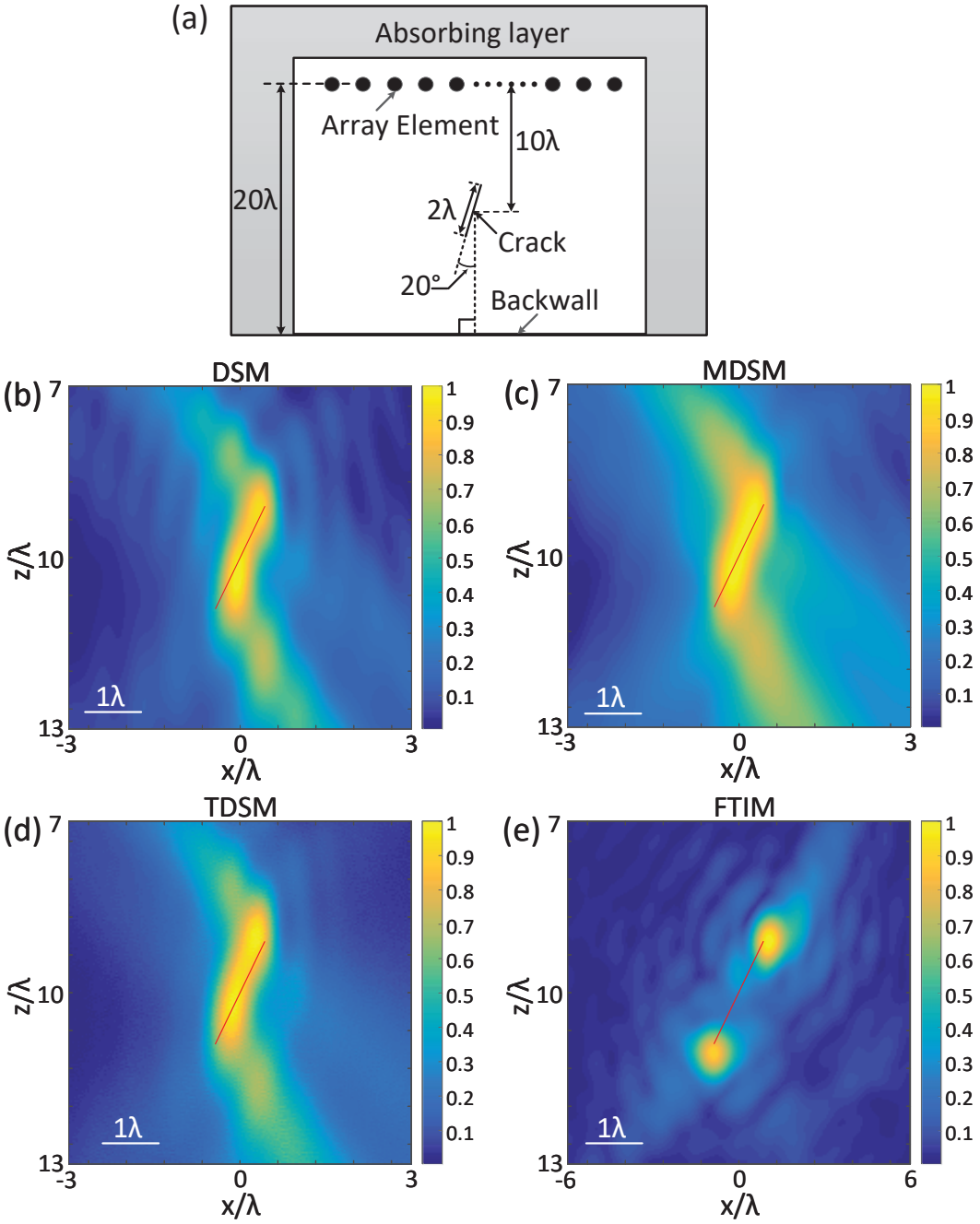


Figure 5.7: All plots as in Fig. 5.5, except for a tilt angle of 20°.

$SNR = 20dB$, and $SNR = 5dB$. The imaging results of the proposed imaging algorithms under different noise levels are shown in Fig. 5.8. These DSM algorithms (DSM, MDSM and TDSM) are able to stably image defects under a high noise level ($SNR = 5dB$) as the generated images were not affected by the addition of the noise, as shown in Fig. 5.8. It is clear that FTIM shows good robustness to the addition of the noise, but one trend is also very clear: with an increase in noise, more artefacts are introduced around the reconstructed notches in the images.

From Fig. 5.8, it is clear that all of the proposed algorithms are able to work stably and effectively under high noise levels.

5.4 Application in NDE for imaging near backwall defects

This chapter aims to verify the potential of the proposed imaging algorithms in the application of ultrasonic array imaging for non-destructive evaluation, especially for imaging the near backwall defects. Therefore, in this section, the proposed imaging algorithms were applied to different types of near backwall defect to test their applicability in the field of NDE.

5.4.1 Near backwall side-drilled holes

The proposed imaging algorithms were firstly applied to detect and image near backwall side-drilled holes embedded in a 50 × 260 × 30mm 304L steel block, as shown in in Fig. 5.9.

The diameters of the holes are 3mm and the distance between any two holes is 10mm. These holes are only 5mm from the backwall. An array probe with the parameters shown in Table 5.1 was used for experimental measurements. This array probe was manufactured by IMASONIC ($Haute - Saône$, France). The longitudinal wave speed in 304L steel is about $5800m/s$, therefore, the diameter of the holes is about 1.25λ while the holes are only 2λ from the backwall, which means that the signals from the defect will easily be masked by the reflections from the backwall. Then, the array was placed directly above

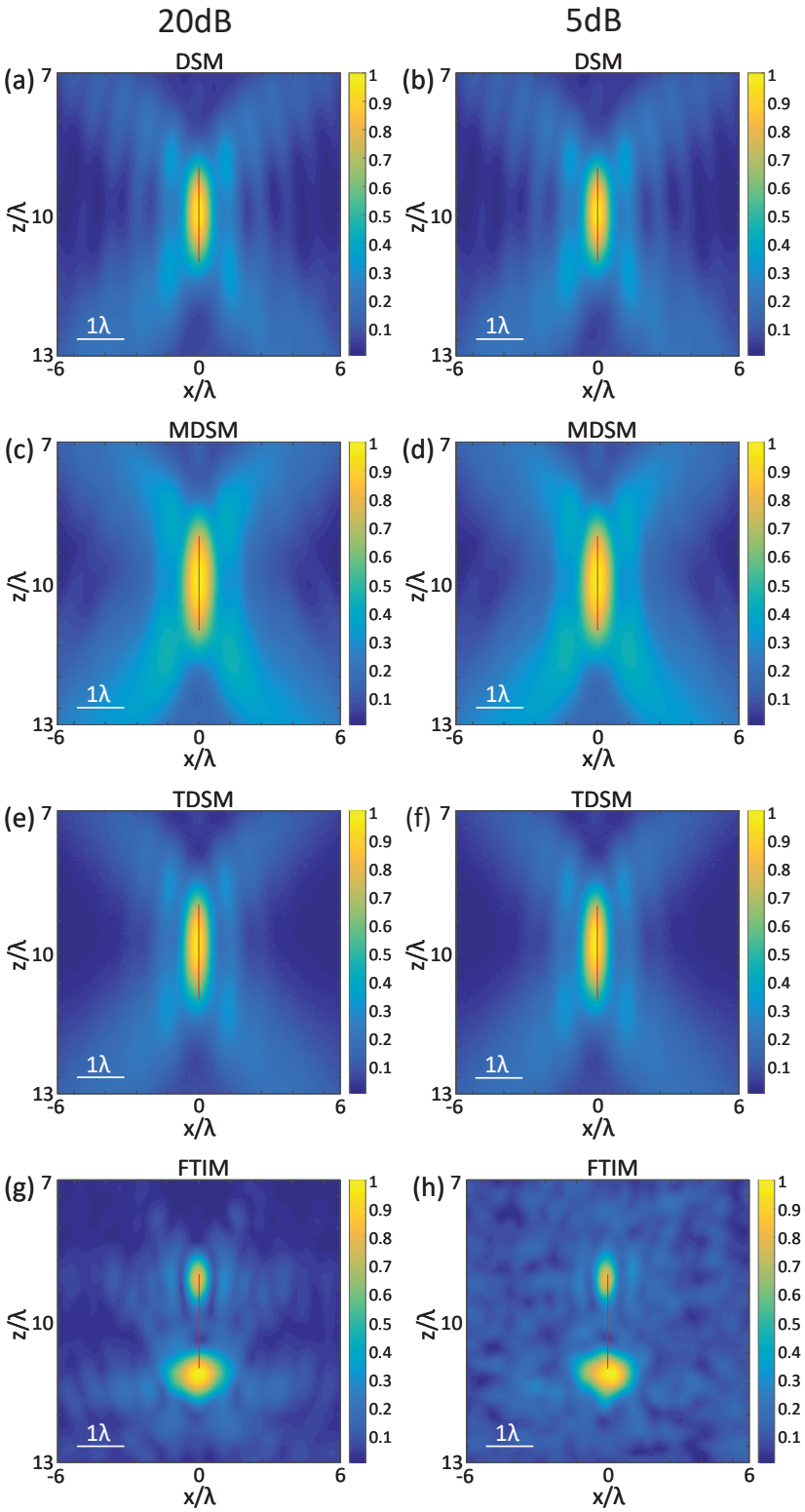


Figure 5.8: DSM images of an embedded notch under different noise levels: (a) $SNR = 20dB$; (b) $SNR = 5dB$. MDSM images of an embedded notch under different noise levels: (c) $SNR = 20dB$; (d) $SNR = 5dB$. TDSM images of an embedded notch under different noise levels: (e) $SNR = 20dB$; (f) $SNR = 5dB$. FTIM images of an embedded notch under different noise levels: (g) $SNR = 20dB$; (h) $SNR = 5dB$. Note that the red line in the images is used to represent the true location and shape of the notch. The imaging results here are from simulated data.

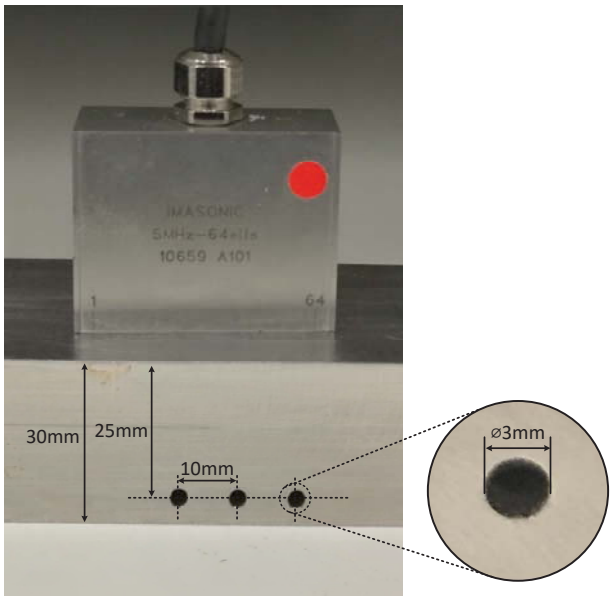


Figure 5.9: Picture of the experiment sample that contains three side-drilled holes.

Table 5.1: Specifications of the ultrasonic array used in experiments.

Element number	Central frequency (MHz)	Bandwidth (-6dB; MHz)	Element width (mm)	Element pitch (mm)	Aperture size (mm)
48	2.5	1.66 to 3.22	1.0	1.2	57.4

the holes and the FMC data was captured. In order to achieve the pure defect signal, the FMC subtraction was used to remove structural reflections. After that, all of the proposed imaging algorithms were applied to the same processed data to reconstruct the side-drilled holes, and the imaging results are shown in Fig. 5.10.

From Fig. 5.10, one can immediately see that all of the proposed imaging algorithms have successfully detected the existence of the side-drilled holes and accurately reconstructed the locations of these holes. The images generated by the DSM, the MDSM and the TDSM are quite close to each other, however, the indications reconstructed by these algorithms are larger than the real shape of the holes (see Fig. 5.10 (a), (b) and (c)), which is because ultrasonic array imaging is essentially a limited aperture problem; the loss of information leads to degradation of the reconstructions, particularly the vertical elongation. From Fig. 5.10(d), it is clear that the FTIM accurately reconstructed the upper surfaces of the three holes, as the upper surfaces are the surfaces interacted with the incident field in this limited aperture case. The FTIM, which also has the best performance in reconstructing

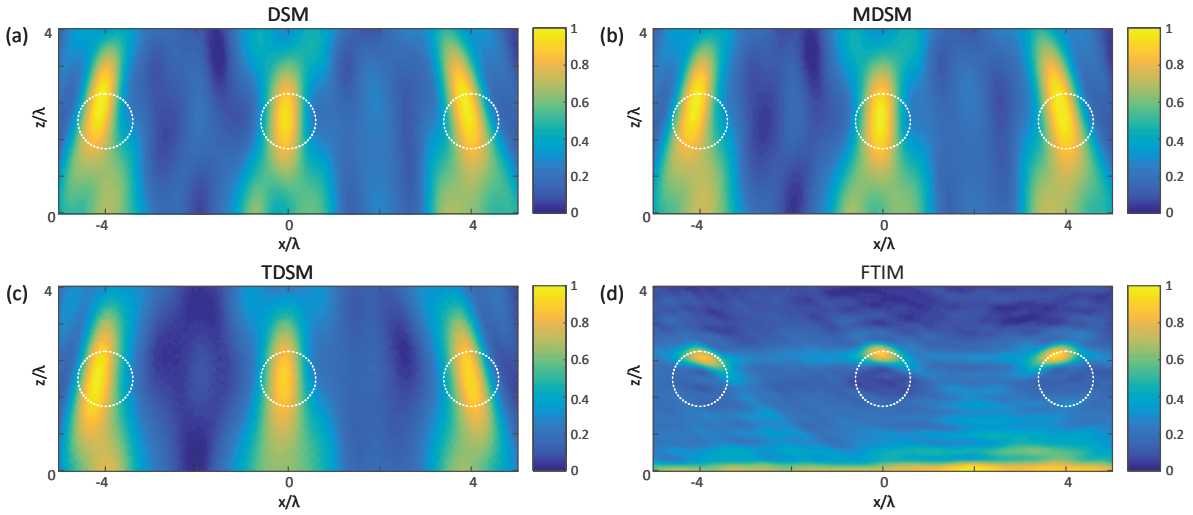


Figure 5.10: The (a) DSM, (b) MDSM, (c) TDSM and (d) FTIM imaging results based on the experimental data. The DSM was calculated at 2.5MHz, the MDSM was calculated using 10 uniformly distributed frequencies between 2.0MHz and 3.0MHz, the TDSM was calculated using the time domain data and the FTIM was calculated using a 70kHz frequency step between 2.0MHz and 3.0MHz. Note that the side-drilled holes are labelled in the images and the images were normalized to the maximum value in each image.

point scatterers in our simulation work, has generated the best imaging result among all of the imaging results of the near backwall side-drilled holes. It should be noted that there are significant indications of backwall in Fig. 5.10(d), this is because that the FMC subtraction, which is used to eliminate backwall reflections here, will leave some residual backwall reflections after subtraction.

5.4.2 Surface-breaking notch

After applying the imaging algorithms to the near backwall side-drilled holes, the proposed imaging algorithms were then assessed experimentally on a 140×255×38mm 304L stainless steel block which contains a 2D surface-breaking notch, as shown in Fig. 5.11.

This 2D notch is an EDM (Electrical Discharge Machining) notch whose depth is 5mm and width is 0.4mm. The array probe used here is also the 2.5MHz probe whose parameters are shown in Table 5.1. The longitudinal wave speed in this steel block is about $5920m/s$, therefore, the depth of the notch is about 2λ for this 2.5MHz probe, which is consistent with the previous simulation work. Then, the array was placed directly above the 2D notch and the FMC data was captured. Again, FMC subtraction, outlined in Chapter

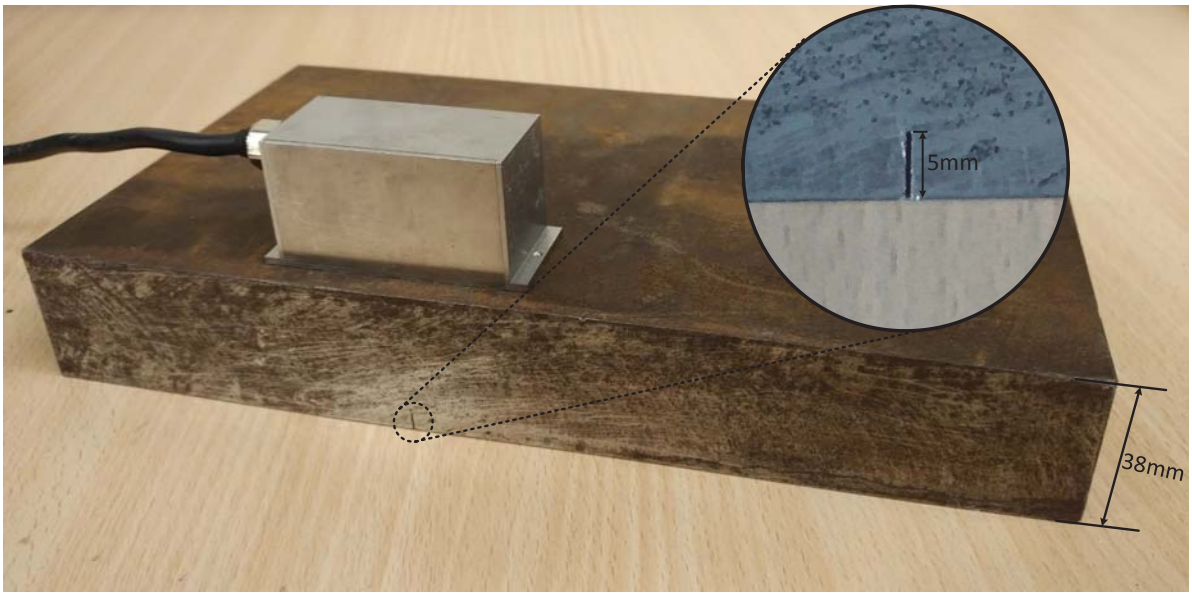


Figure 5.11: Picture of the experiment sample that contains a surface-breaking notch.

3, was used to remove the backwall reflection, in order to extract the defect signal. All of the proposed imaging algorithms were applied to the data after FMC subtraction to reconstruct the surface-breaking notch, and the imaging results are shown in Fig. 5.12.

From these imaging results, it is clear that all of the DSM algorithms (the DSM, the MDSM and the TDSM) have successfully detected the existence of the EDM notch and also generated strong indication to represent the location and shape of this EDM notch, which is in accordance with our simulation work. From Fig. 5.12(a), it is clear that the DSM provides a good reconstruction with a strong indication to represent the EDM notch and just a few artefacts, however, the depth is underestimated.

The images generated by the MDSM or the TDSM show an improvement in image quality when compared to the image generated by DSM as the notch is more accurately reconstructed and artefacts are reduced, as shown in Fig. 5.12(b) and (c). One possible explanation as to why the single frequency version DSM underestimates the notch depth is that the energy of tip diffraction in the experimental data is weak and also the experimental data contains complex series of signals, e.g. noise and mode conversions, thus the tip diffraction is easily masked by the other signals. By using the multiple-frequency information, the tip of the notch can be successfully reconstructed and the artefacts can be reduced, as shown in Fig. 5.12(b) and (c). The best result achieved here is the im-

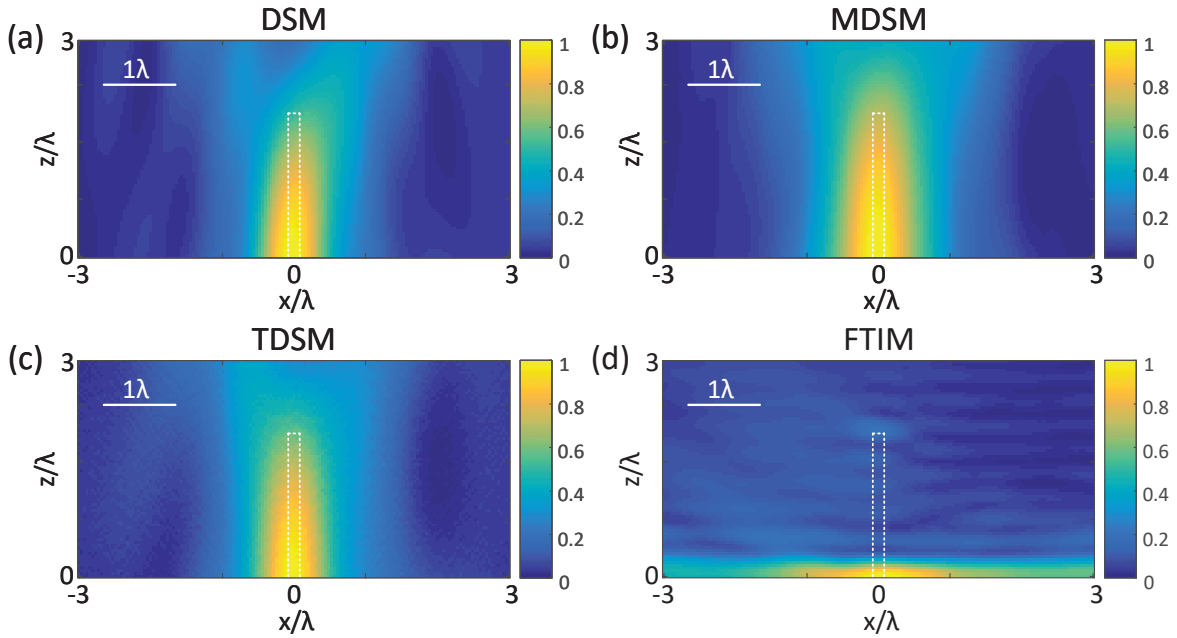


Figure 5.12: The (a) DSM, (b) MDSM, (c) TDSM and (d) FTIM imaging results based on the experimental data. The DSM was calculated at 2.5MHz, the MDSM was calculated using 10 uniformly distributed frequencies between 2.0MHz and 3.0MHz, the TDSM was calculated using the time domain data and the FTIM was calculated using a 70kHz frequency step between 2.0MHz and 3.0MHz. Note that the EDM notch is labelled in the images the images were normalized to the maximum value in each image.

age generated by multiple-frequency version DSM (MDSM or TDSM) because that these images contain very good reconstructions of the EDM notch and also have the fewest artefacts compared the other images, as shown in Fig. 5.12.

The FTIM reconstructed a strong indication to represent the backwall and a weak indication to represent the notch tip (see Fig. 5.12(d)). One can immediately see that the intensity of the background noise is comparable to the intensity of the notch tip, thus it is difficult to characterize this notch from image generated by the FTIM. TFM has also been applied to the experimental data based on the component that contains surface-breaking notch and the imaging result has been found to be quite similar to Fig. 5.12(d).

Here, the discussions of the imaging results are mainly focused on the image qualities. Thus, it will be helpful to quantitatively study the imaging results in the future, for example the sizing accuracy of the surface-breaking notch.

5.5 Conclusions

In this chapter, recent imaging algorithms, including the DSM, the MDSM, the TDSM and the FTIM, are investigated as potential imaging algorithms for ultrasonic array imaging using Full Matrix Capture data.

Firstly, some preliminary mathematical analysis of these imaging algorithms are carried out and the formulations of the proposed methods are provided. Then, the effectiveness of these imaging methods is illustrated via various simulations, including point scatterers and notches. The simulation work suggests that the proposed imaging algorithms work reasonably well and can tolerate strong noise for ultrasonic array imaging using Full Matrix Capture data. Also, through the numerical examples, it has been found that the FTIM has advantages in imaging point scatterers while the DSM, the MDSM and the TDSM are able to handle tilted notch cases (up to 15°).

For experimental validation, we firstly used the proposed imaging algorithms to reconstruct three near backwall side-drilled holes. The results show the locations of the side-drilled holes were correctly reconstructed by the proposed algorithms, however, in the case of limited aperture problem, the whole shapes of the side-drilled holes were not accurately reconstructed by the algorithms.

After that, we examine the performance of the proposed imaging algorithms for reconstructing an EDM notch with a depth of 2λ in a steel block through an experimental array system. The experimental results show that all the proposed imaging algorithms have successfully detected the existence of the notch and crack-like indications were reconstructed by the DSM algorithms (the DSM, the MDSM and the TDSM). Moreover, the multiple-frequency version algorithms (the MDSM and the TDSM) provide satisfying reconstructions of the EDM notch as the location, shape and depth of the EDM notch were all well estimated. However, FTIM failed to provide a image that contains clear indications of notch tip.

The discussions in this chapter are more focused on the the image qualities. Thus, a careful study about the notch depth sizing criteria of DSM and FTIM will need to be investigated to quantitatively study upon their abilities in imaging the crack-type defect.

Chapter 6

Array imaging of defects near a rough backwall

6.1 Introduction

This thesis has so far considered the inspection problem of components with smooth flat backwall, and the backwall eliminating methods developed in Chapter 3 also rely on the backwall reflection being from a smooth flat surface. However, real safety-critical components, especially in service pressure-containing components, commonly have rough surfaces [112]. However, the roughness of the surface will dramatically affect the scattering pattern (scattering amplitude and angular distribution) from this surface. Fig. 6.1 [113] demonstrates the effect of the roughness on the scattering pattern. From Fig. 6.1(a), it is clear that the scattering from the smooth surface is coherently in the specular direction and very little energy scatters to angles away from this specular direction [113]. An increase in roughness will lead to the attenuation of the main lobe while the energy out of the specular direction will be distributed in a more widely diffused field (Fig. 6.1(b)). For a very rough surface, there is no specular main lobe and all of the energy are redistributed into the diffuse field, as shown in Fig. 6.1(c). According to [114], an increase in roughness will also lead to a more complicated waveform.

As a perfectly smooth surface is rare in reality and the surface roughness has a significant effect on the scattering pattern [115], in order for the backwall eliminating methods to

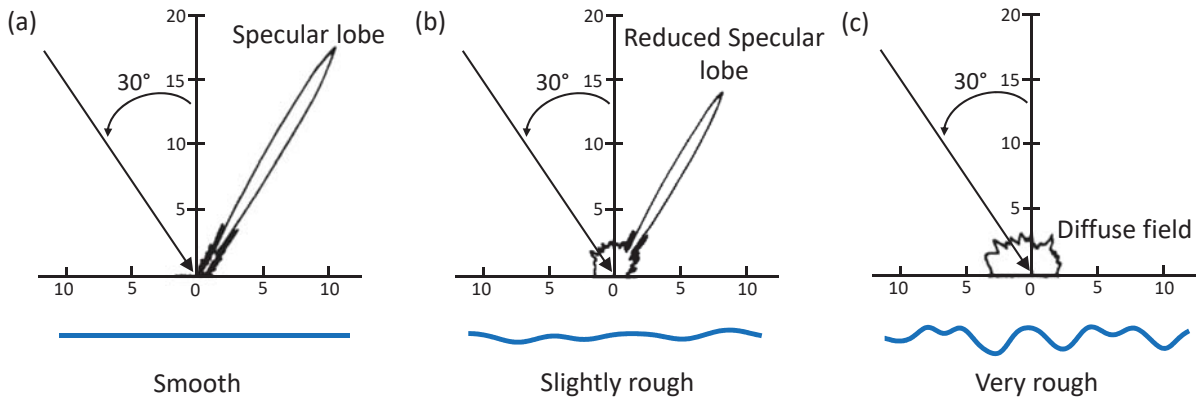


Figure 6.1: RMS intensities of scattering amplitude distribution averaged over 20 realizations for an incident angle of 30° from surfaces with different roughness: (a) a smooth surface, (b) a slightly rough surface and (c) a very rough surface.

be applied in real industrial situations, these methods need to show robustness to a certain degree of backwall roughness. Thus, it is of great importance to validate the performance of the backwall eliminating methods on different backwall roughness. To achieve an acceptable limit of roughness for a specific backwall eliminating method, the imaging experiment would require several iterations where the roughness of the backwall is adjusted. This would be time-consuming in physical trials. Therefore, in this chapter, the performance of the backwall eliminating methods on rough backwalls is tested by numerical simulations.

6.2 Numerical generation of rough surfaces

In order to assign any surface roughness to a statistical class, it is necessary to use several surface statistical parameters to characterize the surface roughness. The surface profiles of a rough surface have been found to obey a certain statistical distribution [116]. For example, in [117, 118], the variation of experimentally measured surface height data is close to Gaussian. Therefore, the Gaussian surface is used in this thesis to numerically generate rough surfaces. To start using the Gaussian random surface profile, the scattering problem of a plane wave from an infinite rough surface is defined in Fig. 6.2.

As shown in Fig. 6.2, the surface geometry considered in this chapter is two-dimensional for simplification. While the specific scattered field may not be exactly the same as the

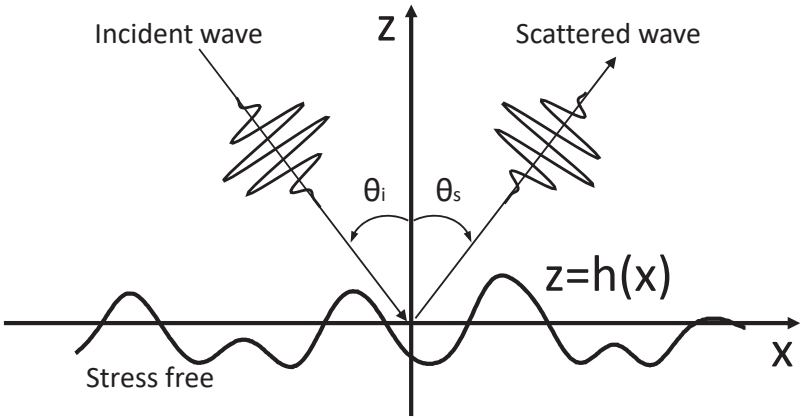


Figure 6.2: Sketch of the scattering on an infinitely long rough surface with stress free boundary condition

full 3D case, the general principles and behaviours will be captured by this approach. The variation in height (h) is defined to be in the z-axis while the rough surface profile is defined along the x-axis. Then, the rough surface is defined by the function

$$z = h(x), \tag{6.1}$$

where h represents the height variation from $z = 0$. The mean value of the height data h is defined as $< h >$ and is always set to zero for a Gaussian surface. Assuming a Gaussian surface, the probability density function $p(h)$, which is used to describe the statistical distribution of $h(x)$, is a Gaussian function, given by

$$p(h) = \frac{1}{\delta\sqrt{2\pi}} exp[-\frac{h^2(x)}{2\delta^2}], \tag{6.2}$$

where δ is the RMS (root-mean-square) of the height data. The rough surface can be represented by a set of numbers z_i which are the height variations from the plane $z = 0$ at the position x_i along the x-axis [113]:

$$z_i = h(x_i) = h(i\Delta x), \tag{6.3}$$

where the adjacent x_i are separated by the incremental change Δx, which is the element size of FE simulation [119]. Based on this, the discretized version of the estimation of δ

is as follows:

$$\delta = \sqrt{< h^2 >} = \sqrt{\frac{1}{N}\sum_{i=1}^{N} {z_i}^2}, \tag{6.4}$$

In order to generate a Gaussian surface in the FE model which will be spatially discretized, a discretized version of the probability density function is given by

$$p(h) = \frac{1}{\delta\sqrt{2\pi}} exp(-\frac{z_i^2}{2\delta^2}), \tag{6.5}$$

Generally, the height scale of the rough surface is determined by the RMS. In order to describe the lateral variation of the surface height of the rough surface, another parameter is required, which is the correlation length. Ref. [115] explains that for a Gaussian surface, the correlation function which is used to characterize the correlation length is

$$C(\boldsymbol{R}) = \frac{< h(\boldsymbol{r})h(\boldsymbol{R}+\boldsymbol{r}) >}{\delta^2} = exp(-\frac{x^2}{\lambda_x}), \tag{6.6}$$

where λ_x is the correlation length along the x-axis, as distance over which the correlation function $C(\boldsymbol{R})$ falls by $1/e$ [120]. In this thesis, the surface is generated by selecting the RMS value δ and the correlation length λ_x. It should be noted that an increase in the RMS value δ or a decrease in the correlation length λ_x will lead to an increase in the roughness. The rough surface is created through the commonly used moving average method [113]. In this method, a series of uncorrelated random numbers are generated, which are then convolved with a particular weighting function to generate the height data $h(x)$ of the required rough surface. Generally, the RMS value δ and the correlation length λ_x are defined relative to the longitudinal wavelength λ_0. The generated height data $h(x)$ of the rough surface can be imported into the commercial FE package (Abaqus), then, a model of a metal block with a rough backwall can be created. Three realizations of the Gaussian rough surface are shown in Fig. 6.3. If we compare Fig. 6.3(b) or (c) with Fig. 6.3(a), the effects of changing the parameters δ and λ_x on roughness can be clearly seen.

Here, in order to be consistent with Chapter 3, the thickness of the component was also set to be 20λ while the depth of the notch was 2λ. A 64-element 2MHz phased array with

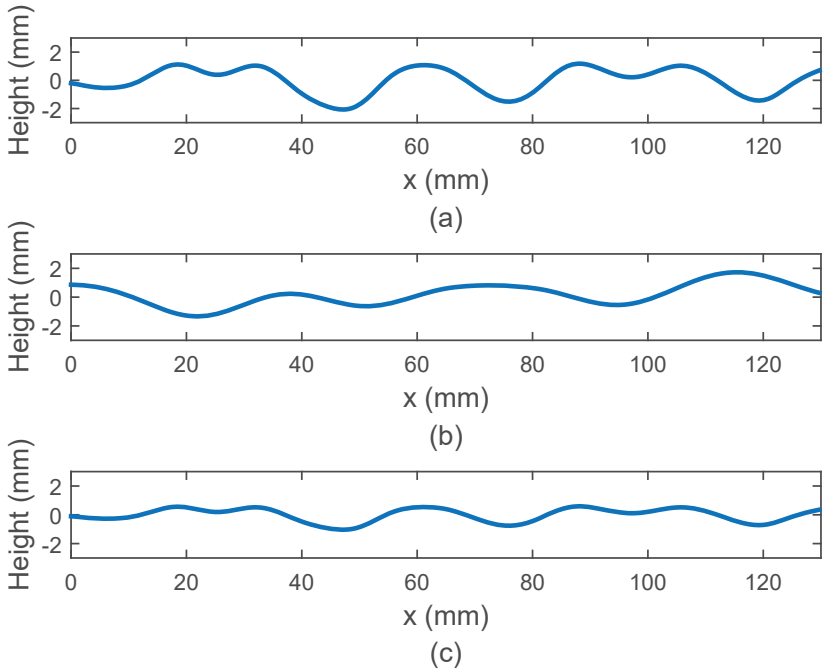


Figure 6.3: Realizations of 2D isotropic Gaussian rough surface profiles: (a) $\delta = 1mm$ and $\lambda_x = 9mm$; (b) $\delta = 1mm$ and $\lambda_x = 18mm$; (c) $\delta = 0.5mm$ and $\lambda_x = 9mm$.

an element spacing of 0.5λ was used to excite and record ultrasound fields. The array was placed on the flat frontwall while the notch was grown from the rough backwall. The material used for the model was isotropic steel with a density of $7700kg/m^3$, a Young's modulus of $195GPa$ and a Poisson ratio of 0.28. The excited ultrasound wave was a Hann windowed 5 cycle tone burst with a central frequency 2MHz, thus, the longitudinal wavelength λ_0 is about 3mm.

For simplicity, all the properties of the model were defined to be uniform out of the plane and only longitudinal waves were excited and recorded for simplicity [76]. Again, absorbing layers were attached to the boundary of the model. Based on the FE model, the FMC data, which contains the defect signal and reflections from rough backwall, can be captured and then used for imaging. The sketch of the FM model used in this chapter is shown in Fig. 6.4.

In this chapter, 9 different rough profiles were tested with the various combinations of RMS value $\delta = \lambda_0/12$, $\lambda_0/6$ and $\lambda_0/3$, and correlation length $\lambda_x = 12\lambda_0$, $6\lambda_0$ and $3\lambda_0$. In order to make the quantitative analysis in this chapter more convenient, the three rough

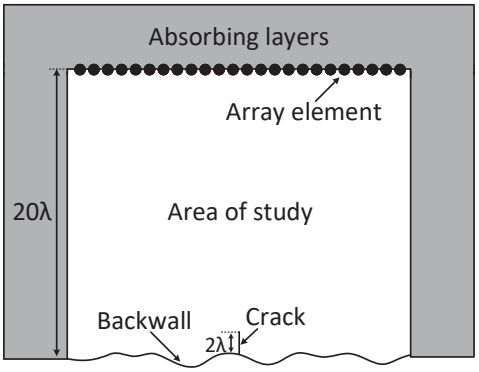


Figure 6.4: Sketch of FE model which contains a Gaussian rough backwall (not to scale).

profiles with $\delta = \lambda_0/12$ & $\lambda_x = 12\lambda_0$, $\delta = \lambda_0/12$ & $\lambda_x = 6\lambda_0$ and $\delta = \lambda_0/6$ & $\lambda_x = 12\lambda_0$ are classified as 'slight roughness', the three rough profiles with $\delta = \lambda_0/12$ & $\lambda_x = 3\lambda_0$, $\delta = \lambda_0/6$ & $\lambda_x = 6\lambda_0$ and $\delta = \lambda_0/3$ & $\lambda_x = 12\lambda_0$ are classified as 'moderate roughness' and the three rough profiles with $\delta = \lambda_0/6$ & $\lambda_x = 3\lambda_0$, $\delta = \lambda_0/3$ & $\lambda_x = 6\lambda_0$ and $\delta = \lambda_0/3$ & $\lambda_x = 3\lambda_0$ are classified as 'high roughness'.

6.3 Numerical results and discussions

6.3.1 Imaging results

Firstly, the proposed backwall eliminating methods, including FMC subtraction, the weighting function method and the truncation method, were applied to the same FMC data captured from a very slightly rough case ($\delta = \lambda_0/12$ and $\lambda_x = 12\lambda_0$), as shown in Fig. 6.5 (a). In order to ensure convenient comparisons, the amplitude of the following imaging results in this chapter are normalized to the maximum value in each image and the images are scaled to the range of [0,1] if not otherwise specified. The imaging results of the proposed methods, which have been introduced in detail in Chapter 3, are shown in Fig. 6.5 (b)-(e). To enable a direct comparison with the perfectly smooth case, the imaging results based on the perfectly smooth backwall case are shown in Fig. 6.6.

By comparing Fig. 6.5(b) and Fig. 6.6(b), it is clear that even a slight roughness of the backwall will have an obvious influence on the effectiveness of the FMC subtraction, as there is more background noise in Fig. 6.5(b), which indicates that more residual backwall reflections were left after FMC subtraction when the backwall is rough. As FM is more

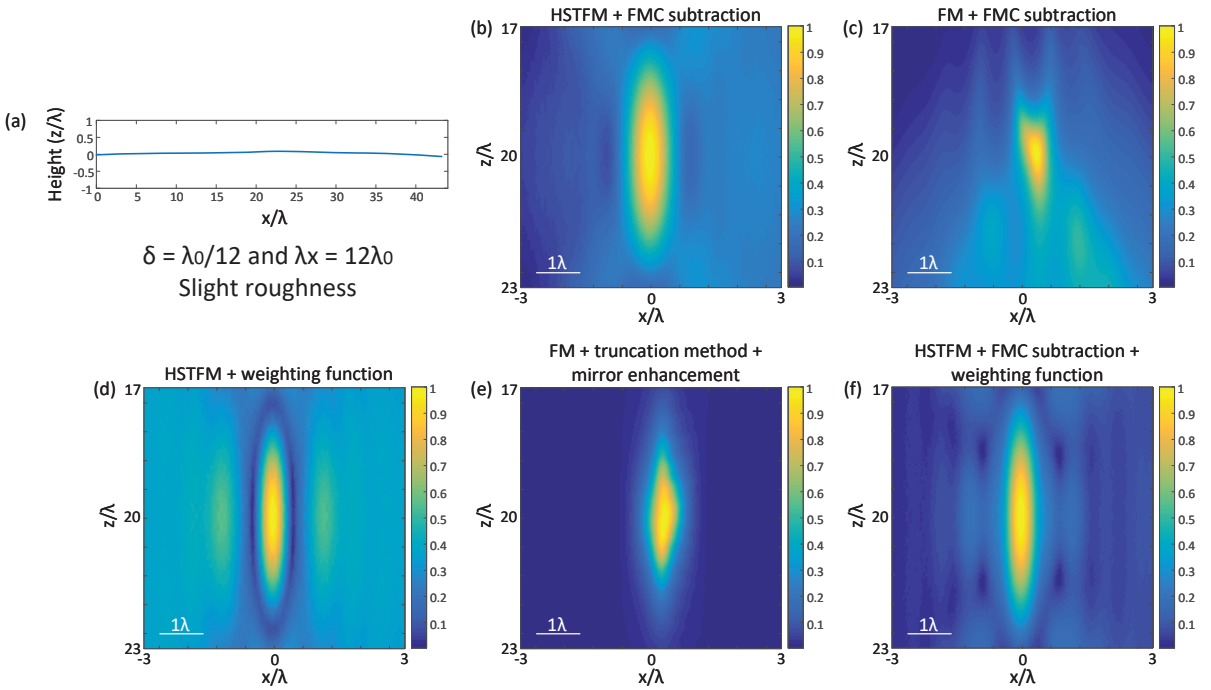


Figure 6.5: (a) The plot of the height data of the Gaussian rough backwall ($\delta = \lambda_0/12$ and $\lambda_x = 12\lambda_0$) used in the FE model that provided FMC data. (b) HSTFM and (c) FM images based on the FMC data after FMC subtraction; (d) HSTFM with the weighting function image based on the original FMC data; (e) FM with the truncation method and the mirror enhancement image based on the original FMC data; (f) HSTFM with the weighting function image based on the FMC data after FMC subtraction.

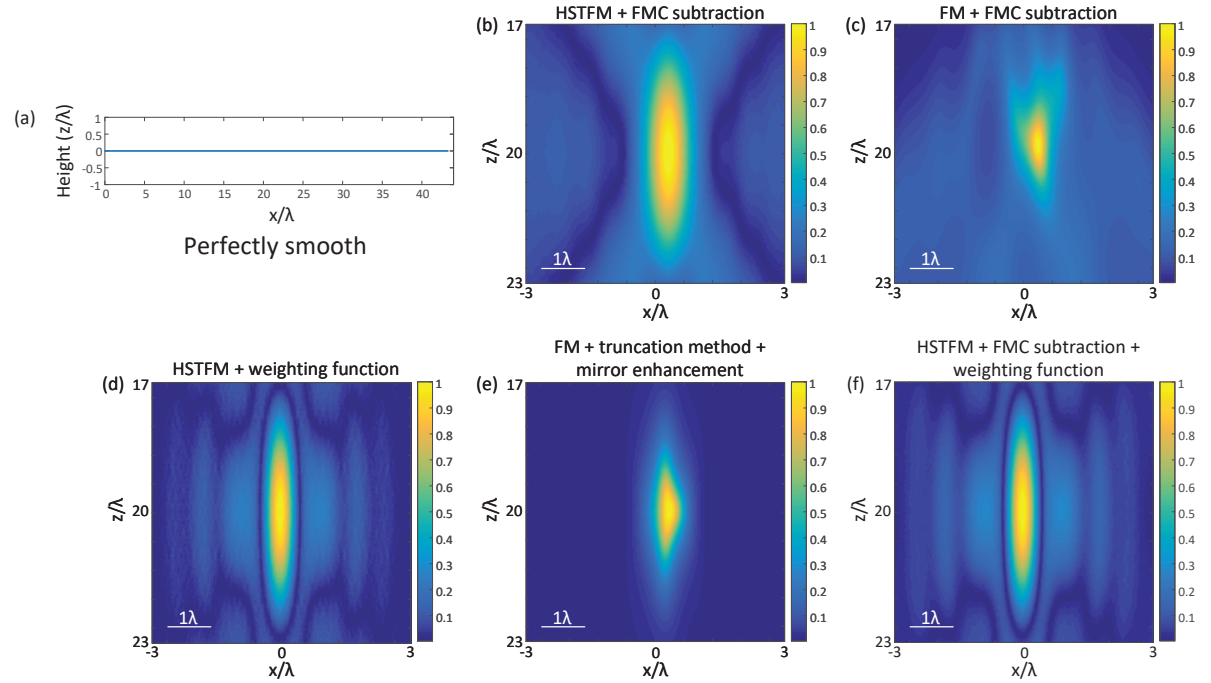


Figure 6.6: As Fig. 6.5, except with a perfectly smooth backwall.

sensitive to noise and other types of signals, the indication of the notch in Fig. 6.5(c) has been partially distorted, however, for the perfectly smooth backwall case, the shape of the notch has been accurately reconstructed though there are still some artefacts (see Fig. 6.6(c)). This is because for a slightly rough surface, the scattering pattern has obviously changed when compared to a perfectly smooth surface (see Fig. 6.1(a) and (b)). Although most of the scattering from a slightly rough surface is coherently in the specular direction, some of the scattering energy is distributed into the diffuse field. As FMC subtraction assumes that all the ultrasound waves from the backwall undergo specular reflection, the diffused ultrasound waves introduced by the backwall roughness will lead to a larger error in the FMC subtraction.

Also, the effectiveness of the weighting function method, which has been specifically developed for the HSTFM to eliminate the backwall effects, was influenced by the surface roughness, as this method left strong side bars near the main indication of the notch for the slightly rough case (see Fig. 6.5). This is because this method is based on the assumption that the ray paths of the backwall reflections considered in the HSTFM will always have the same angle between the incident direction and the reflected direction, which also implies that the ultrasound waves from the backwall should undergo the specular reflection.

Unlike the FMC subtraction and the weighting function method, the performance of the FM with the truncation method and the mirror enhancement on the slightly rough case is almost the same as the perfect smooth case (see Fig. 6.5(e) and Fig. 6.6(e)), which is because the truncation method tries to directly image the surface-breaking notch by controlling the singular values for calculation and the singular values related to the notch are always the largest ones (see Fig. 3.10). Therefore, this method would not be influenced by a slight roughness as the introduced weak diffuse field from backwall will not affect the largest singular values and all the small singular values will be truncated out.

In this chapter, a combined method (FMC subtraction + weighting function method) was also tested, as for the rough backwall cases, a single FMC subtraction or weighting function is not sufficient to clearly eliminate the backwall effects. From Fig. 6.5(f), it is obvious that by using the conventional HSTFM together with this combined method, the effects introduced by the backwall reflection vanished clearly for the slightly rough

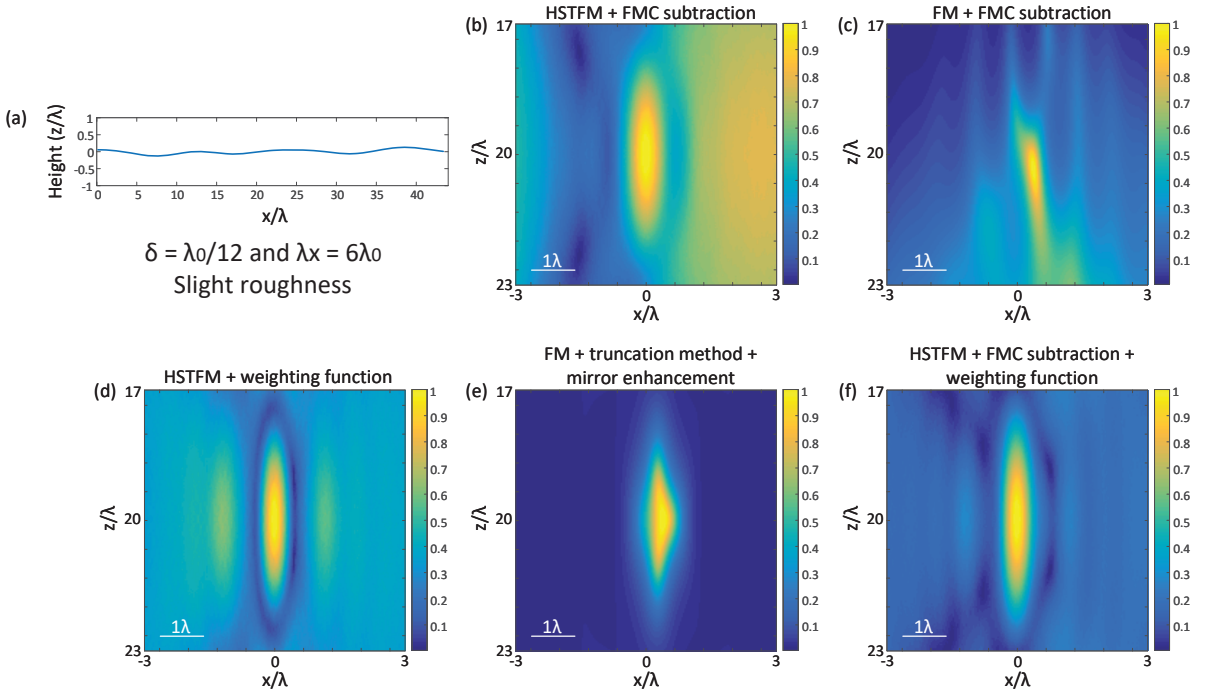


Figure 6.7: As Fig. 6.5, except with roughness parameters of $\delta = \lambda_0/12$ and $\lambda_x = 6\lambda_0$.

backwall case. Then, in order to find the limiting roughness for each of the proposed methods, various backwall roughnesses have been tested and results are shown in Fig. 6.7 to Fig. 6.14.

The various imaging results clearly demonstrate the limiting roughness of the proposed methods. Firstly, it is clear that FMC subtraction can only stand a slight roughness of the backwall. For example, for a moderate roughness ($\delta = \lambda_0/6$ and $\lambda_x = 6\lambda_0$), the HSTFM image based on the data after FMC subtraction failed to provide a clear and strong indication of the notch and contained very strong backwall effects (see Fig. 6.10(b)). This is because FMC subtraction is based on the fact that for element pairs of the same lateral separation, the length of ray paths of backwall reflections are identical for the case of two planar surfaces, which becomes invalid when the roughness of the backwall increases.

The HSTFM with the weighting function showed some robustness to the backwall with moderate roughness (e.g. Fig. 6.10(d)) but failed to provide a clear indication of the notch for the high roughness case (e.g. Fig. 6.14(d)), which is because the majority of the energy will still scatter into the specular direction from a moderately rough surface

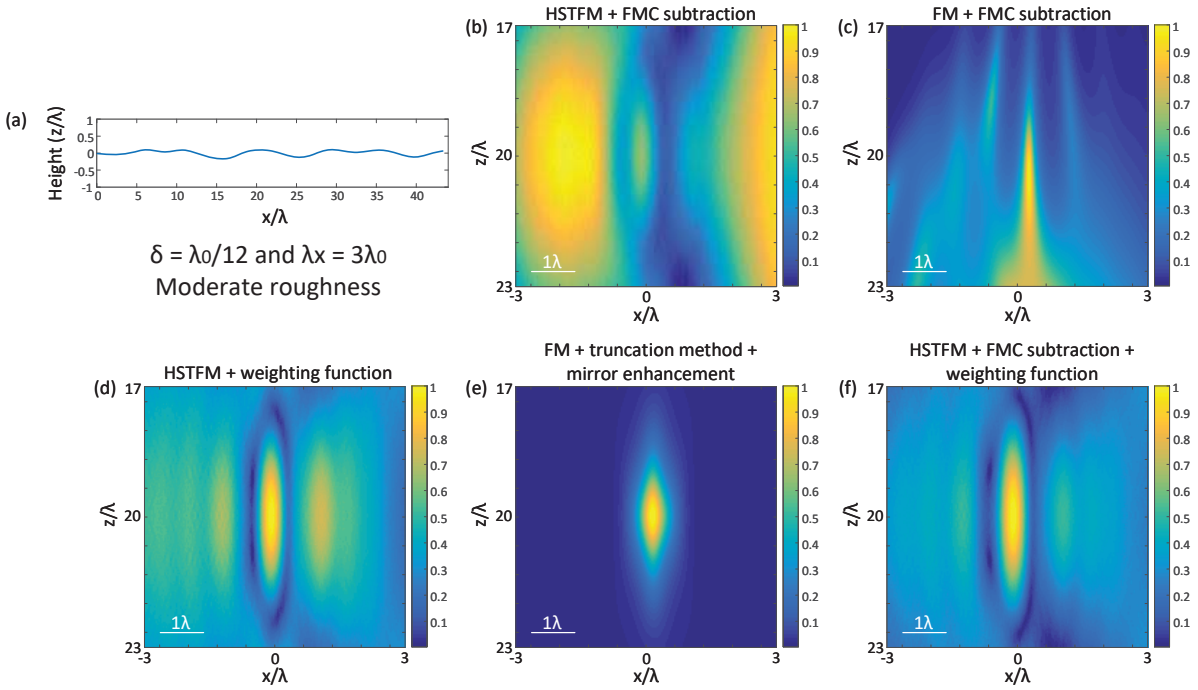


Figure 6.8: As Fig. 6.5, except with roughness parameters of $\delta = \lambda_0/12$ and $\lambda_x = 3\lambda_0$.

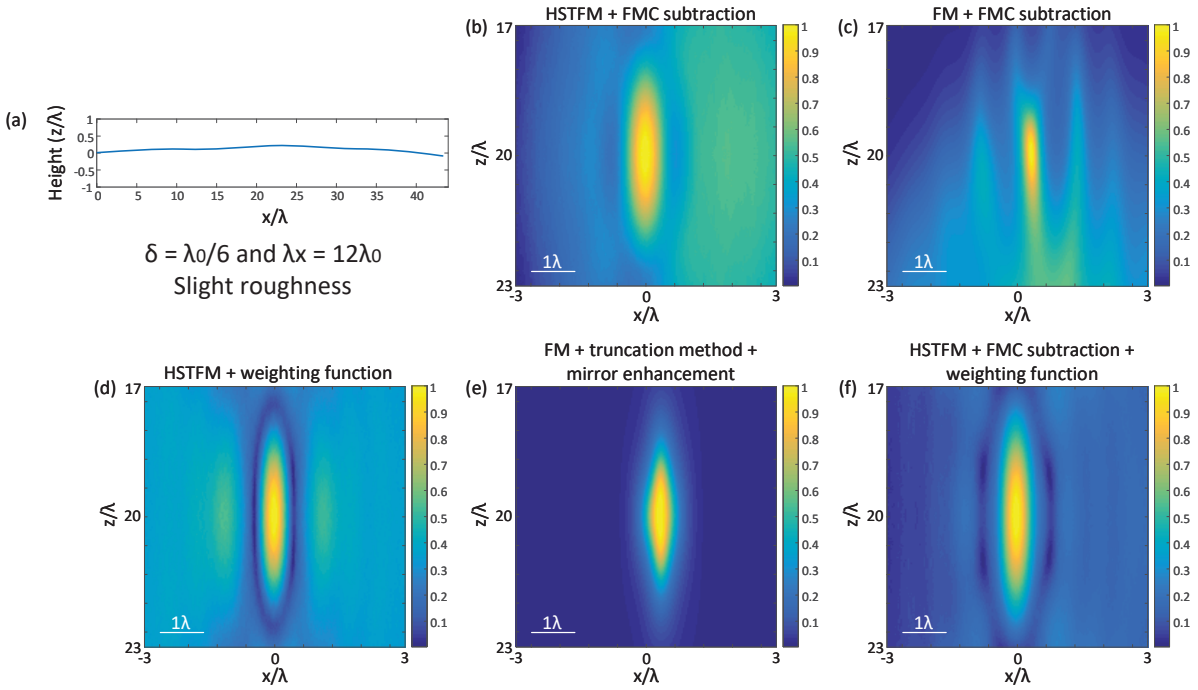


Figure 6.9: As Fig. 6.5, except with roughness parameters of $\delta = \lambda_0/6$ and $\lambda_x = 12\lambda_0$.

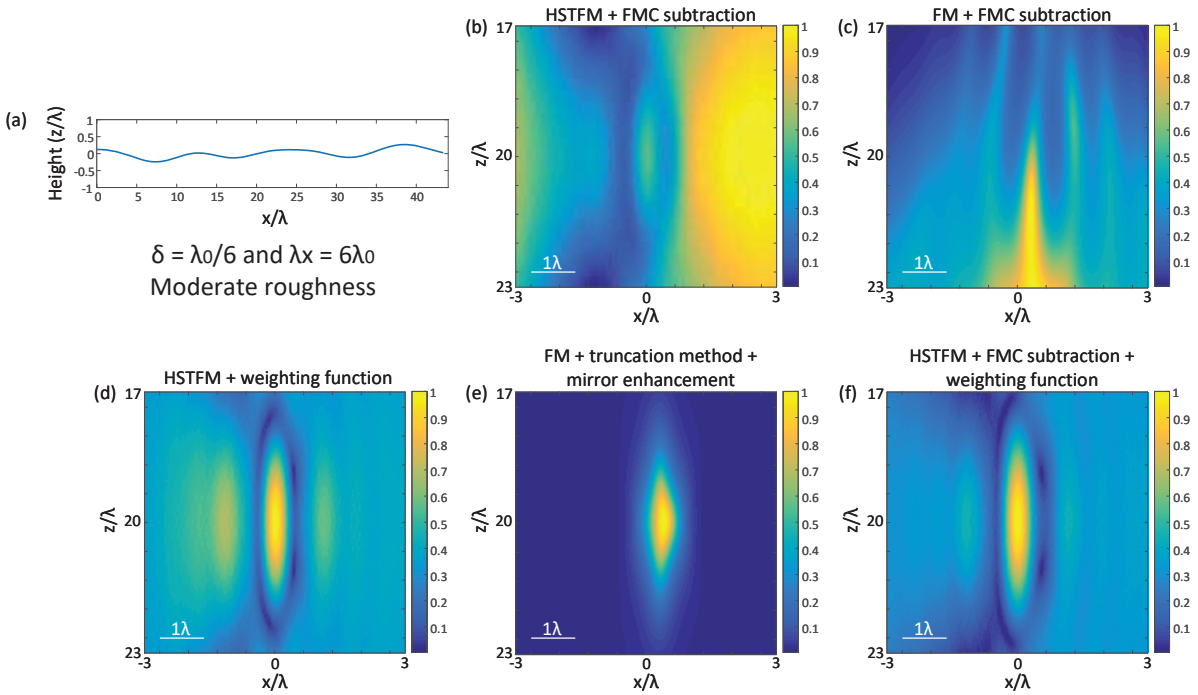


Figure 6.10: As Fig. 6.5, except with roughness parameters of $\delta = \lambda_0/6$ and $\lambda_x = 6\lambda_0$.

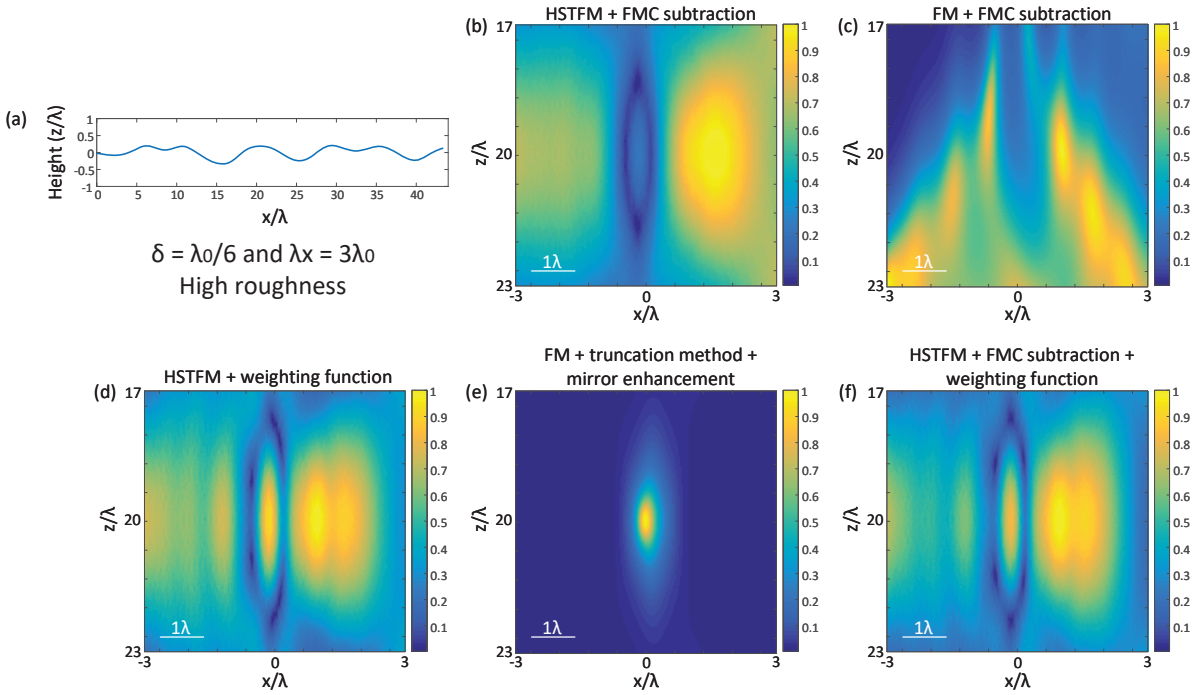


Figure 6.11: As Fig. 6.5, except with roughness parameters of $\delta = \lambda_0/6$ and $\lambda_x = 3\lambda_0$.

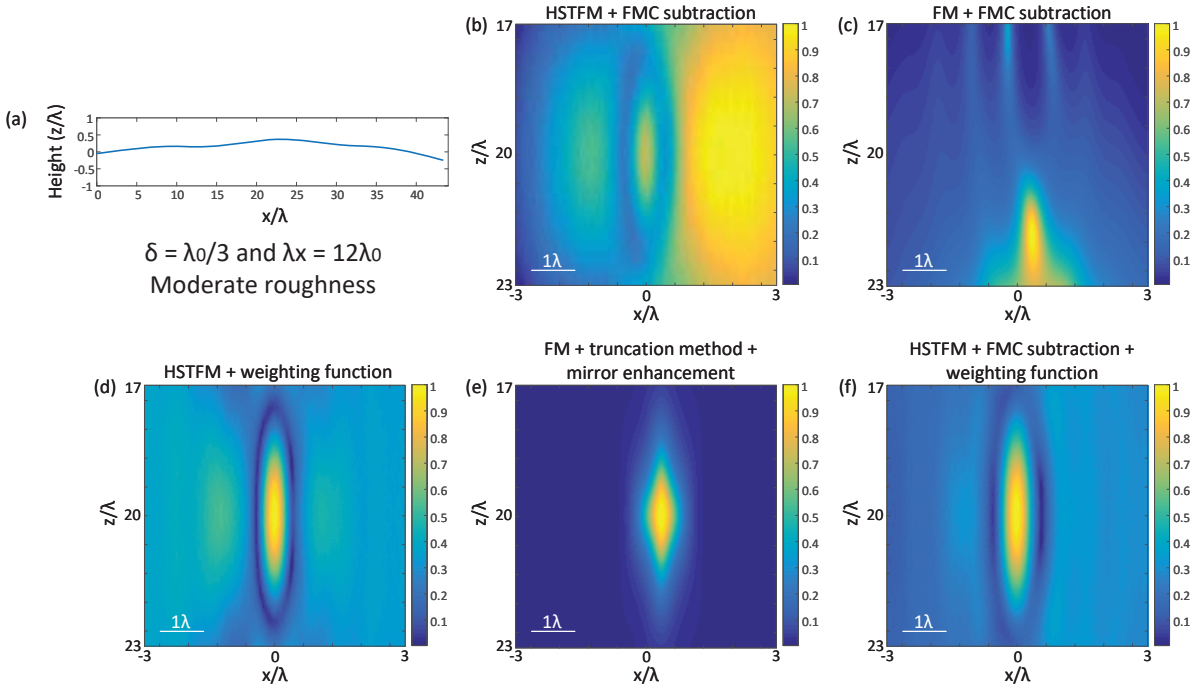


Figure 6.12: As Fig. 6.5, except with roughness parameters of $\delta = \lambda_0/3$ and $\lambda_x = 12\lambda_0$.

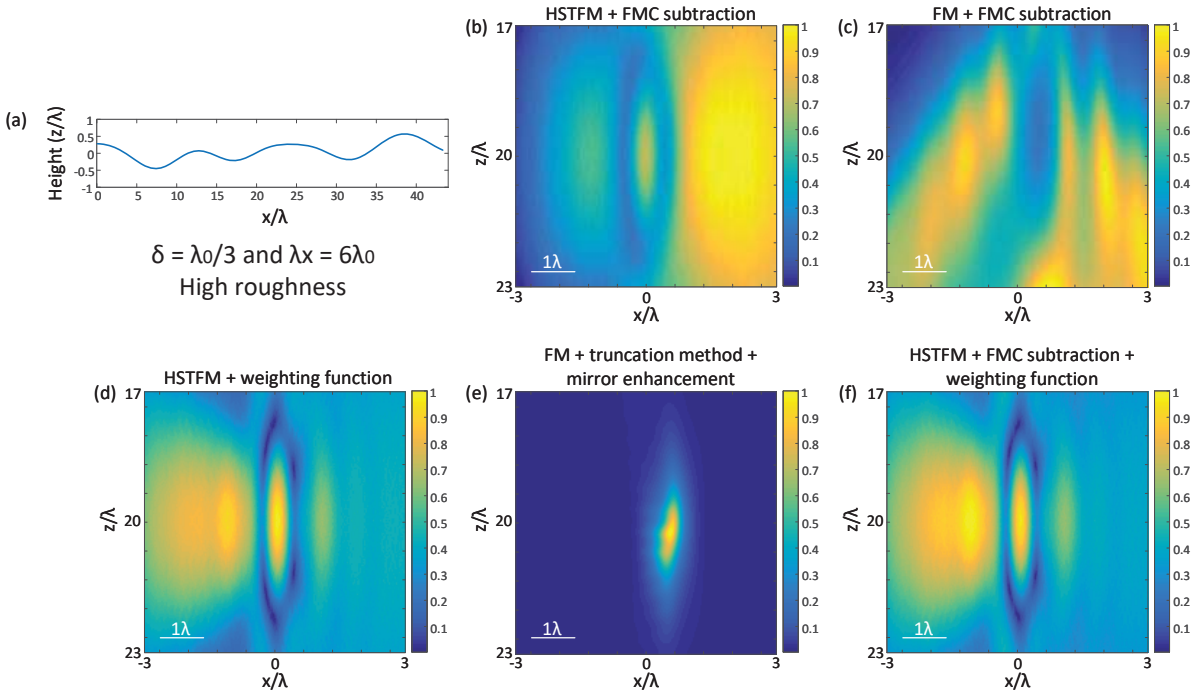


Figure 6.13: As Fig. 6.5, except with roughness parameters of $\delta = \lambda_0/3$ and $\lambda_x = 6\lambda_0$.

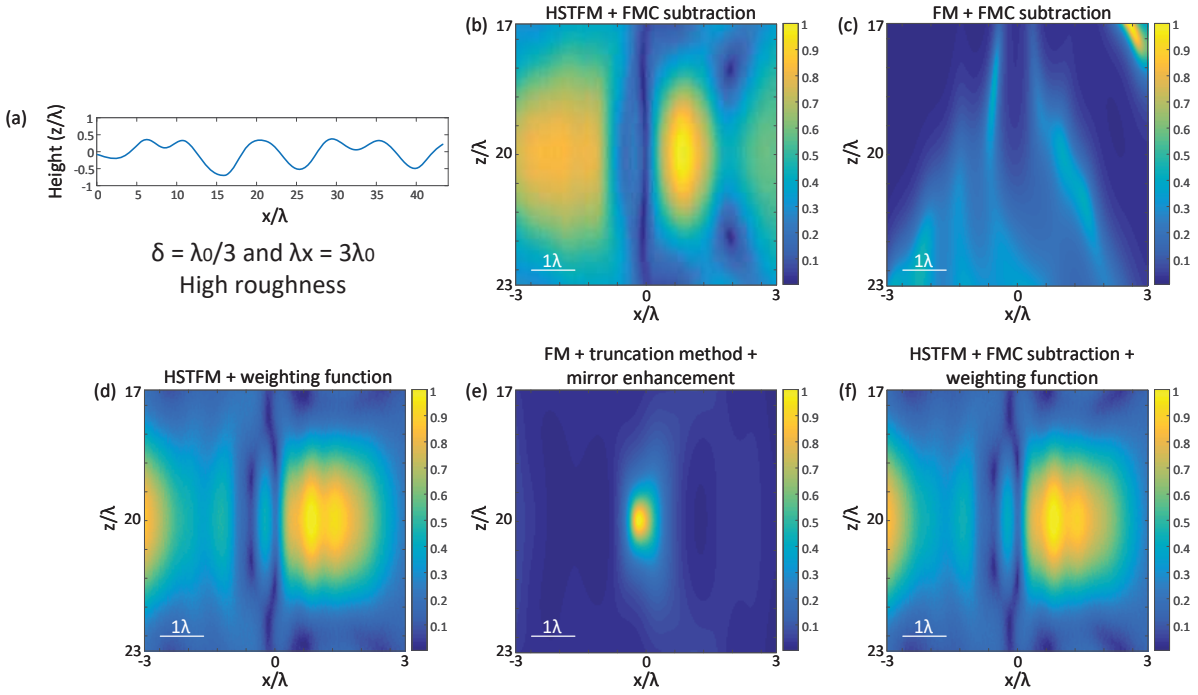


Figure 6.14: As Fig. 6.5, except with roughness parameters of $\delta = \lambda_0/3$ and $\lambda_x = 3\lambda_0$.

but ultrasound waves from a very rough surface can be scattered to any direction.

For HSTFM with FMC subtraction and the weighting function, excellent performance is shown for the slight roughness and moderate roughness cases as these imaging results contain a very strong notch indication without artefacts or with only a few weak artefacts (e.g. Fig. 6.7(f) and Fig. 6.10(f)). However, the notch indications are totally masked by the backwall effects in the images generated by HSTFM with FMC subtraction and the weighting function for the high roughness cases. It should be noted that for the high roughness cases, the image reconstructed by the HSTFM with the combined method is almost the same as the image reconstructed by the HSTFM with the weighting function (e.g. Fig. 6.13(b) and Fig. 6.13(f)), which implies that the FMC subtraction is not working for the high roughness cases.

FM with the truncation method and the mirror enhancement also showed a good robustness to the moderate roughness cases (e.g. Fig. 6.10(e)) but provided inaccurate estimation of the defect shape for the high roughness cases (e.g. Fig. 6.14(e)). This is because for a very rough surface, the energy of the ultrasound field from this surface will be scattered into a diffuse field, and the scattered field from the notch will become

easily lost in this diffuse field from the very rough backwall, thus, even by controlling the singular values used for calculation, it is difficult to locate the scatterers of interest (i.e. the notch).

Based on the above facts, for the rough backwall cases, two methods, the HSTFM with the FMC subtraction and the weighting function and the FM with the truncation method and the mirror enhancement, have shown the best roughness robustness and generated best imaging results among all of the proposed methods. As the main object of imaging is to ensure an accurate characterization of the defect, the sizing results of these two methods are compared in the next section.

6.3.2 Sizing results

According to Chapter 4, the sizing method based on the image generated by the FM with the truncation method and the mirror enhancement can be summarized as: firstly, the center of the notch, x_c, is determined at the position where the pixel in the generated image has the maximum amplitude; then, the image value at $x = x_c$ is plotted against vertical distance, z; after that, the z values of the two points on the plot whose amplitude are equal to -15dB are measured; finally, the notch depth is equal to half of the difference of the two measured z values. The sizing method for the HSTFM image is almost the same with the sizing method for the FM image and the only difference is that the sizing criterion used for the HSTFM image is -6dB [31]. Thus, the sizing results based on these methods were calculated and shown in Table 6.1. The sizing results of the high roughness cases are not listed, since, as for the high roughness cases, none of the proposed methods can generate satisfactory images from which sizing can be performed.

From the sizing results listed in Table 6.1, one can immediately find that for slight roughness cases, both methods can provide accurate sizing with errors smaller than 3.3% and 6.7%, respectively. Obviously, the roughness of the backwall will affect the sizing results of both methods, as the largest error will always occur in the moderate roughness cases. Additionally, the for the slight roughness cases, the HSTFM with the FMC subtraction and the weighting function can provide more accurate sizing while for the moderate roughness cases, the FM with the truncation method and the mirror enhancement can provide more

Table 6.1: Sizing results of a 6mm surface-breaking notch originated from a rough backwall

	slight roughness			moderate roughness		
	$\delta = 1/12\lambda_0$, $\lambda_x = 12\lambda_0$	$\delta = 1/12\lambda_0$, $\lambda_x = 6\lambda_0$	$\delta = 1/6\lambda_0$, $\lambda_x = 12\lambda_0$	$\delta = 1/12\lambda_0$, $\lambda_x = 3\lambda_0$	$\delta = 1/6\lambda_0$, $\lambda_x = 6\lambda_0$	$\delta = 1/3\lambda_0$, $\lambda_x = 12\lambda_0$
HSTFM with FMC subtraction and weighting function	5.9mm, error 1.7%	5.8mm, error 3.3%	5.8mm, error 3.3%	5.2mm, error 13.3%	5.2mm, error 13.3%	5.4mm, error 10.0%
FM with truncation method and mirror enhancement	6.4mm, error 6.7%	5.9mm, error 1.7%	6.3mm, error 5.0%	5.4mm, error 10.0%	5.6mm, error 6.7%	5.8mm, error 3.3%

accurate sizing. Thus, based on the sizing results listed in this section and the imaging results shown in the previous section, it can be concluded that the HSTFM with the FMC subtraction and the weighting function has the best performance among all the proposed methods for the slight roughness cases while the FM with the truncation method and the mirror enhancement has the best performance for the moderate roughness cases.

6.4 Conclusions

In this chapter, in order to test the applicability of the proposed backwall eliminating methods in practical situations, these methods were used to image surface-breaking notches originated from rough backwall through numerical simulations. Based on the imaging results, the conclusions can be summarized as:

* The FM with the FMC subtraction can only work for the component with perfectly smooth backwall

* The HSTFM with the FMC subtraction can tolerate slight roughness (e.g. $\delta = 1/12\lambda_0$, $\lambda_x = 12\lambda_0$) of the backwall

* The HSTFM with the weighting function can tolerate moderate roughness (e.g. $\delta = 1/6\lambda_0$, $\lambda_x = 6\lambda_0$) of the backwall, however, obvious artefacts start to occur in the generated images for the moderate roughness cases.

* The HSTFM with the FMC subtraction and the weighting function and the FM with the truncation method and the mirror enhancement are able to generate satisfactory images for the backwall with slight (e.g. $\delta = 1/12\lambda_0$, $\lambda_x = 12\lambda_0$) or moderate roughness (e.g. $\delta = 1/6\lambda_0$, $\lambda_x = 6\lambda_0$).

To ensure further analysis, the sizing results of HSTFM with the FMC subtraction and the weighting function and the FM with the truncation method and the mirror enhancement were listed and compared. By comparing the sizing results, it is clear that among these two methods, the HSTFM with the FMC subtraction and the weighting function has a better performance for slight roughness cases while the FM with the truncation method and the mirror enhancement has a better performance for moderate roughness cases. In addition, none of the proposed methods are valid for the backwall with a high roughness, which is because the ultrasound wave from a very rough backwall will undergo diffuse reflection rather than specular reflection, upon which all the proposed methods are based.

Chapter 7

Conclusions

7.1 Thesis review

In this thesis, a challenging problem in the field of non-destructive evaluation, to image near backwall defects in safety-critical components using ultrasonic arrays, has been explored. New post-processing methods, which need to be used together with specific imaging algorithms, have been developed to eliminate the strong indications or artefacts introduced by the presence of the backwall in order to ensure a clear image of the surface-breaking crack itself. The recently developed super resolution algorithm, the Factorization Method, has been explored for the application of subsurface imaging of the surface-breaking cracks. The performance of other recent imaging algorithms on imaging near backwall defects has also been tested. In order to examine the range of the applicability of the proposed post-processing methods which are developed to eliminate backwall effects in practice, these methods have also been applied to a component with a rough backwall to test their performance. All the studies conducted in this thesis are with the ultimate motivation to improve the detectability of the near backwall defects in safety-critical components.

Chapter 2 outlined the theories and formulations behind ultrasonic array imaging. It began by a brief derivation of the wave equation. Then, the forward scattering problem, which aims to calculate the scattered field with the knowledge of the incident field and the properties of the object, was outlined in this chapter. The imaging problem is an

inverse scattering problem, which aims to reconstruct the object function given the far field measurements of the scattered field and the knowledge of the incident field, thus, the inverse scattering problem was also introduced in Chapter 2. The Beamforming algorithms (e.g. Total Focusing Method and Half-Skip Total Focusing Method) which are based on the Born Approximation were introduced. It was demonstrated that although the Born Approximation can offer a linear solution to the inverse scattering problem, higher spatial information cannot be measured, which leads to the resolution limit ($\lambda/2$) of the Beamforming algorithms. The approach of the super resolution algorithms (Linear Sampling Method and Factorization Method), which are theoretically capable of achieving unlimited resolution, was discussed. This kind of algorithm is based on the factorization of the far-field operator and takes multiple scattering into account in the reconstruction of the object. The mathematical implementations of the Linear Sampling Method and the Factorization Method were also outlined in this chapter.

In Chapter 3, the challenge in imaging the near backwall defects was outlined in detail. Usually when inspecting near backwall defects, the array has to be placed on the frontwall to detect the near backwall defects. It was shown that the presence of the backwall brings a strongly reflecting planar interface which will introduce strong effects (indications or even artefacts) into the imaging results generated by the imaging algorithms. The strong effects can easily mask the indication of the defect itself, thus, it is necessary to eliminate the backwall effects to ensure a clear imaging of the near backwall defect. In this chapter, several post-processing methods were developed to eliminate the backwall effects and the mathematical basis and the implementation of each method was introduced in detail. These methods can be applied easily with few tuning parameters or little prior knowledge. The performance of the proposed imaging techniques was validated in both simulation and experiments.

With the application of the backwall eliminating methods, the Factorization Method, which is a recently developed super resolution imaging algorithm, successfully reconstructed the surface-breaking notch with high accuracy. The principal objective of imaging is to have an accurate sizing of the surface-breaking notch, thus, the accuracy of measuring of surface-breaking notches based on images generated by FM was assessed in Chapter 4. The FM with FMC subtraction and FM with the truncation method, which were the

methods developed in Chapter 3 to image near backwall defects, were tested with various levels of noise and various sizes of surface-breaking notch. The numerical simulations also led to the development of the specific sizing methods for the proposed methods. After all the simulation study, the proposed methods and the sizing methods were applied to the experimental data in order to validate their effectiveness.

Recently, with the developments in scattering theory, some innovative imaging algorithms have been developed, such as the Direct Sampling Method (DSM) and the Fast Topological Imaging (FTIM). To extend the current library of imaging algorithms, the DSM and the FTIM were applied to the ultrasonic array imaging of defects in solids in Chapter 5. Through the numerical simulations, the effectiveness of these imaging algorithms were examined in terms of the ability to reconstruct different types of defects and the robustness to noise. This chapter also verified the potential of these imaging algorithms for imaging near backwall defects through the experimental ultrasonic array system.

In Chapter 6, an important practical aspect of imaging the near backwall defects was discussed. The backwall eliminating methods developed in Chapter 3 implicitly assumed the backwall to be perfectly smooth; in reality, however, it is not the case. The effectiveness of these methods were tested when the backwall is not perfectly smooth as a significant step before these methods could be used in real industrial situations. A series of FE models that contained a surface-breaking notch originating from a rough backwall were created. For these models, the depth of the notch was kept the same but the roughness of the backwall varied. Then, the backwall eliminating methods were applied to the FMC data captured from the model with a rough backwall. Based on the imaging results, the limiting roughness for each method was obtained.

7.2 Main achievements

In this thesis, several advancements were made, innovative methods were developed and many experiments were performed relating to the practical implementation of ultrasonic arrays to image and characterize near backwall defects.

The subsurface imaging of the near backwall defects using ultrasonic arrays suffers from strong backwall reflections, especially when a zero incident angle is chosen for inspection

(i.e. the array placed directly above the defect), which is the inspection configuration chosen in this thesis. The reason why the zero incident angle is chosen in this thesis is because the ultrasonic array imaging is essentially a limited aperture problem and the zero incident angle can ensure the biggest angle of view for a chosen array. The strong backwall reflections will introduce strong artefacts into the image generated by the imaging algorithm (e.g. the Factorization Method or the Half-Skip Total Focusing Method), thus, in order to clearly image and accurately characterize the defect, it is necessary to eliminate the strong effects introduced by the backwall reflections in the imaging result.

Several post-processing methods have been developed in this thesis as a response to this challenge. FMC subtraction attempts to remove the backwall reflections contained in the captured FMC data by reconstructing the pure backwall reflections based on the FMC data and subtracting these. As the FMC subtraction directly removes the backwall reflections in the captured data, it theoretically works for any imaging algorithm. The weighting function method is a backwall eliminating method that is developed specifically for the HSTFM to image the near backwall crack or the surface-breaking crack. This method is based on the angle difference between the backwall reflection and the defect signal considered in the HSTFM and works as a weighting function in the imaging algorithm (i.e. the HSTFM). The truncation method is a method that attempts to remove the backwall effects in the FM image by controlling the singular values used in the calculation of the FM image. In addition, the mirror enhancement is developed to compensate the unavoidable loss of information when the truncation method is used, and is based on utilizing the existence of the backwall to increase the available aperture of the array. The above methods have been successfully applied in the imaging process to eliminate the backwall effects and helped the imaging algorithms to achieve satisfactory images of the near backwall defects in both simulations and experiments.

Although the development of the proposed backwall eliminating methods implicitly assumes that the backwall is perfectly smooth, all of the proposed methods have shown some robustness to the roughness of the backwall. According to the various imaging results and sizing results in Chapter 6, the HSTFM with the FMC subtraction and the weighting function is recommended for imaging near backwall defects when the backwall has a slight roughness while the FM with the truncation method and the mirror enhance-

ment is recommended when the backwall has a moderate roughness. However, none of the methods developed in this thesis can handle the case when the backwall has a very large roughness, as the dominant scattering pattern from a very rough backwall is no longer a specular reflection but a diffused reflection.

The ability of the Factorization Method to achieve unlimited resolution has attracted many researchers' attentions and is considered to have huge potential in the field of non-destructive evaluation [39, 40, 60]. In this thesis, the practical implementation of the FM for imaging and characterizing near backwall defects is explored. As FM is a sensitive imaging algorithm, signals other than those from the defect itself contained in the captured data will easily influence the imaging result generated by FM. Based on the simulations and experiments in Chapter 4, by applying the FM together with the related backwall eliminating method (i.e. the FMC subtraction or the truncation method), FM is able to clearly image the near backwall defects with a high resolution.

Also, in order to characterize the notch immediately from the generated FM image, a specific sizing method, including sizing procedure and sizing criterion, has been developed. It should be noted that the value of the sizing criterion depends on which backwall eliminating method is chosen, for example, when FMC subtraction is used to eliminate the backwall effects, -12dB should be chosen and when the truncation method with the mirror enhancement is used, -15dB should be used. Furthermore, by comprehensively considering the image quality and sizing accuracy, the best performance of FM with FMC subtraction can be achieved when the notch depth is between 1λ and 3λ and the smallest notch that can be imaged and sized by the FM with the truncation method and the mirror enhancement is 1λ. Based on the above findings, it is clear that the FM algorithm is able to correctly detect and accurately size a notch whose depth is not smaller than 1λ, which outperforms the commonly used TFM (smallest depth of 2λ) and the HSTFM (smallest depth of 1.5λ). Based on the various simulation and experimental results in Chapter 4, the best results of FM for setup in this thesis is achieved by using FM with the FMC subtraction and -12dB sizing criterion. The attenuation of the material and the number of elements might also affect the imaging results of FM and their effects need to be investigated in the future.

Although FM has achieved a resolution better than the Rayleigh limit (0.5λ) in the

experiment of imaging point scatterers in [64], the minimum surface-breaking notch that can be imaged and sized in this thesis has a depth of 1λ. This is because FM is sensitive to noise and other uncertainties and the presence of backwall has introduced extra complexity to the measured data.

The expansion in the library of imaging algorithms can make the applicability of ultrasonic array imaging in defect detection more possible. In order to extend the current library of imaging algorithms in imaging the near backwall defects, the Direct Sampling Method and the Fast topological Imaging were studied in this thesis.

The Direct Sampling Method is an effective alternative sampling-type algorithm to the Linear Sampling Methods or the Factorization Method. Similar to the FM, the DSM uses an indicator function whose value will change dramatically from inside the scatterer to the outside to directly reconstruct the shape of the scatterer. The resolution limit of the Direct Sampling Method is 0.5λ, which is the same as for the Beamforming algorithms. The DSM outperforms the LSM or the FM in the robustness to noise and the DSM is able to accurately reconstruct the shape of a notch with a small tilt angle (up to $15°$) in the case of limited aperture.

Also, the convenient utilization of the multiple-frequency information in the DSM has led to the establishments of the Multiple-frequency Direct Sampling Method and the Time Domain Sampling Method. As the multiple-frequency information is able to compensate for some of the information missing in the limited aperture data, the MDSM or the TDSM will generally provide a better reconstruction of the defect than the DSM, which was demonstrated for both simulated and experimental data in Chapter 5. The resolution limit of the MDSM is also 0.5λ, however, the TDSM is able to resolve two point scatterers which are separated by 0.4λ, as shown in Chapter 5. This is because the time domain data used in the TDSM actually contains all the possible multi-frequency information in the measurements while the multiple-frequency data used in the MDSM contains only part of the multi-frequency information in the measurements. According to the above findings, the DSM has a wide range of applicability and huge potential to improve crack detection in solids using ultrasonic arrays.

Applying the Fast Topological Imaging to the inspection of solids with an ultrasonic array also allows fast and accurate inspection of defects. This is different from the Beamforming

algorithms which are based on focusing the waves through the potential position of the object, or the sampling-type algorithms which are based on the prior knowledge of the wave propagation behaviour in the medium. The FTIM is based on the mathematical shape optimization tools, i.e. topological sensitivity methods [108, 109]. The highest lateral resolution that the FTIM achieved in this thesis is 0.5λ and the FTIM has a good robustness to noise. Compared to the sampling-type algorithms, the FTIM has advantages in imaging point-scatterers or side-drilled holes, however, because of the impenetrable nature of the defects in solid, the FTIM can only reconstruct the top surfaces of the side-drilled holes in the case of limited aperture. The image generated by the FTIM only contains tip indications when inspecting a crack-like defect in the case of limited aperture, which is quite similar to the image generated by the Total Focusing Method when inspecting a crack-like defect.

7.3 Potential future work

Although many advances have been made in this thesis, there are still many potential future research ideas which can be pursued in the field of ultrasonic array imaging.

Firstly, as has been mentioned in Chapter 2, ultrasonic array imaging is a limited aperture problem and an ill-posed problem. Thus, an increase or a decrease in the aperture will obviously affect the quality of the imaging result [75]. As the physical aperture of a chosen array is difficult to extend in practice, one possible way to increase the available aperture is to take account of the indirect propagation modes of the wave. One example of utilizing the indirect propagation is the HSTFM, which takes the half-skip propagation into account [31]. In addition to the direct and half-skip propagation modes, the full-skip propagation is an alternative propagation mode which could be used. The schemes of the direct, half-skip and full-skip propagation modes are shown in Fig. 7.1.

Also, throughout this thesis, only the longitudinal wave is used for imaging. The recorded signal by the ultrasonic array will contain the longitudinal waves, the shear waves and the mode conversions between the longitudinal waves and the shear waves. According to [74], TFM can be performed using several propagation modes (direct or indirect) and several types of waves (longitudinal or shear). Based on this characterization, the multi-mode

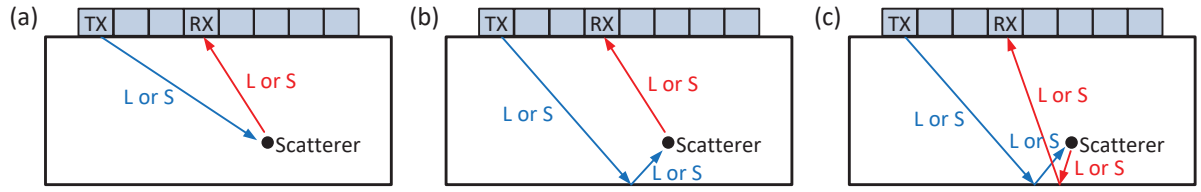


Figure 7.1: Schemes of the different wave propagation modes: a) direct, b) half-skip, c) full-skip

TFM developed by J. Zhang et.al in [121] allows a more accurate reconstruction of the defect. Although the utilization of the half-skip propagation in the FM to allow more accurate reconstruction has been investigated in [75] and in Chapter 3 of this thesis, the utilization of the information contained in the FMC data is not maximized in FM.

Thus, the approach that combines the multi-frequency, the multi-mode (longitudinal, shear and mode conversions) and the multi-propagation (direct, half-skip and full-skip) in a sampling-type algorithm (e.g. the FM or the DSM) should be investigated in the future.

An innovative sampling-type algorithm, the DSM, has been investigated in Chapter 5. The multi-frequency version of the DSM, i.e. the MDSM and the TDSM, has shown an excellent ability to image the crack-type defect in the solid. Thus, a careful study about the crack depth sizing criterion of the DSM will need to be done to capitalize upon its ability in imaging the crack-type defect.

In Chapter 6, we tested the performance of the backwall eliminating methods on the rough backwall. To complete this study, the performance of these methods needs to be evaluated on a series of different rough backwalls, which would be really time consuming through physical trials, thus, a number of numerical simulations were used to create components with rough backwalls and provide array data. Further experimental validations on several specific rough backwall cases will be of great importance to the practical application of these backwall eliminating methods. Through the simulation work done in Chapter 6, we also found that when the backwall is just slightly rough, HSTFM with FMC subtraction and the weighting function can provide the best imaging, and when the backwall is moderately rough, FM with the truncation method and the mirror enhancement will have the best performance. However, in practice, it is almost impossible to have the prior knowledge about the backwall roughness. Recently, a methodology which

uses the ultrasonic array to recover the correlation function of internal rough surfaces has been developed in [122]. This methodology can therefore be embedded into the backwall eliminating process to provide some prior knowledge about the roughness of the backwall to help us select a proper method to image the near backwall defect. In addition, the statistical evaluation of the backwall roughness need to be carried out in the future.

Throughout this thesis, several different imaging algorithms were investigated, e.g. the TFM, the FM, the DSM and the FTIM. In the case of the limited aperture problem which is common in ultrasonic array imaging, the imaging algorithm is not able to reconstruct the whole shape of the defect and each imaging algorithm tends to reconstruct the partial feature of the defect shape. For example, FM will provide a rough reconstruction of the crack shape when imaging an embedded crack while TFM will provide strong indications of the crack tip. As a result, it may be possible to combine the different features of the defect reconstructed by different imaging algorithms to provide a more detailed reconstruction. It still needs much research effort to investigate whether this approach could work.

For the imaging experiments in Chapter 4, two different array probes (1MHz and 5MHz) with different aperture sizes have been used to measure FMC data from the experimental sample. However, the effect of the aperture size has not been considered. Thus, the effect of aperture size on the effectiveness of using FM to image and size near backwall defects is worth studying in the future with the motivation to achieve an optimal aperture size for each inspection task.

All of the simulations and experiments in this thesis are based on the assumption of homogeneous material. The variation in grain orientation and material stiffness between individual grains in an inhomogeneous material will introduce noise into the measured array data, which will introduce extra complexities to the imaging problem. Also, the variation in grain orientation and material property will also cause the refractions of the ultrasound wave that may result in beam bending [123]. Thus, the effectiveness of the developed backwall eliminating methods, the imaging algorithms and the developed sizing methods in heterogeneous material need to be investigated in the future.

References

[1] C. Hellier, Handbook of Nondestructive Evaluation, Second Edition, Mechanical Engineering, McGraw-Hill Education, 2012.

[2] J. Blitz, G. Simpson, Ultrasonic methods of non-destructive testing, Vol. 2, Springer Science and Business Media, 1996.

[3] J. E. Aldrich, Basic physics of ultrasound imaging, Crit Care Med 35 (5 Suppl) (2007) S131–7. doi:10.1097/01.CCM.0000260624.99430.22.

[4] M. Fatemi, A. Kak, Ultrasonic b-scan imaging: Theory of image formation and a technique for restoration, Ultrasonic Imaging 2 (1) (1980) 1 – 47. doi:10.1016/0161-7346(80)90201-1.

[5] T. Hasiotis, E. Badogiannis, N. Tsouvalis, Application of ultrasonic c-scan techniques for tracing defects in laminated composite materials, StrojniÅ¡ki vestnik - Journal of Mechanical Engineering 57 (3) (2011) 192–203. doi:10.5545/sv-jme.2010.170.

[6] W. S. Yeo, J. Berger, Application of raster scanning method to image sonification, sound visualization, sound analysis and synthesis.

[7] B. W. Drinkwater, P. D. Wilcox, Ultrasonic arrays: A comparison between medical and nde requirements, AIP Conference Proceedings 975 (1) (2008) 770–777. doi:10.1063/1.2902740.

[8] B. W. Drinkwater, P. D. Wilcox, Ultrasonic arrays for non-destructive evaluation: A review, NDT & E International 39 (7) (2006) 525–541. doi:10.1016/j.ndteint.2006.03.006.

[9] C. Morgan, W. Trought, G. Sheldon, T. Barton, B-scan and real-time ultrasound in the antepartum diagnosis of conjoined twins and pericardial effusion., American Journal of Roentgenology 130 (3) (1978) 578–580.

[10] K. A. Herzog, The detection of fetal meningocele and meningoencephalocele by b-scan ultrasound: A case report, Journal of Clinical Ultrasound 3 (4) (1975) 307–308.

[11] J.-P. Ardouin, A. Venetsanopoulos, Modelling and restoration of ultrasonic phased-array b-scan images, Ultrasonic Imaging 7 (4) (1985) 321 – 344. doi:10.1016/S0161-7346(85)80004-3.

[12] R. Tech, Introduction to Phased Array Ultrasonic Technology Applications: R/D Tech Guideline, Advanced practical NDT series, R/D Tech, 2004.

[13] O. NDT., Advances in Phased Array Ultrasonic Technology Applications, Advanced practical NDT series, Olympus NDT, 2007.

[14] B. D. Van Veen, K. M. Buckley, Beamforming: A versatile approach to spatial filtering, IEEE assp magazine 5 (2) (1988) 4–24.

[15] C. Holmes, B. W. Drinkwater, P. D. Wilcox, Post-processing of the full matrix of ultasonic transmit-receive array data for non-destructive evaluation, NDT & E International 38 (8) (2005) 701–711. doi:10.1016/j.ndteint.2005.04.002.

[16] C. Fan, M. Pan, F. Luo, B. W. Drinkwater, Multi-frequency time-reversal-based imaging for ultrasonic nondestructive evaluation using full matrix capture, IEEE Transactions on Ultrasonics, Ferroelectrics, and Frequency Control 61 (12) (2014) 2067–2074. doi:10.1109/TUFFC.2014.006574.

[17] X. l. Han, W. t. Wu, P. Li, J. Lin, Application of ultrasonic phased array total focusing method in weld inspection using an inclined wedge, in: Proceedings of the 2014 Symposium on Piezoelectricity, Acoustic Waves, and Device Applications, 2014, pp. 114–117. doi:10.1109/SPAWDA.2014.6998539.

[18] M. Sutcliffe, M. Weston, B. Dutton, P. Charlton, K. Donne, Real-time full matrix capture for ultrasonic non-destructive testing with acceleration of post-processing

through graphic hardware, NDT & E International 51 (2012) 16 – 23. doi:10.1016/j.ndteint.2012.06.005.

[19] C. J. Martin-Arguedas, D. Romero-Laorden, O. Martinez-Graullera, M. Perez-Lopez, L. Gomez-Ullate, An ultrasonic imaging system based on a new saft approach and a gpu beamformer, IEEE Transactions on Ultrasonics, Ferroelectrics, and Frequency Control 59 (7) (2012) 1402–1412. doi:10.1109/TUFFC.2012.2341.

[20] A. J. Hunter, B. W. Drinkwater, P. D. Wilcox, The wavenumber algorithm for full-matrix imaging using an ultrasonic array, IEEE Transactions on Ultrasonics, Ferroelectrics, and Frequency Control 55 (11) (2008) 2450–2462. doi:10.1109/TUFFC.952.

[21] K. E. Thomenius, Evolution of ultrasound beamformers, in: 1996 IEEE Ultrasonics Symposium. Proceedings, Vol. 2, 1996, pp. 1615–1622 vol.2. doi:10.1109/ULTSYM.1996.584398.

[22] M. Jobst, G. D. Connolly, Demonstration of the application of the total focusing method to the inspection of steel welds, in: 10th European Conference on Non-Destructive Testing, 2010.

[23] R. Long, J. Russell, P. Cawley, Ultrasonic phased array inspection using full matrix capture, Insight - Non-Destructive Testing and Condition Monitoring 54 (7) (2012) 380–385. doi:10.1784/insi.2012.54.7.380.

[24] P. D. Wilcox, C. Holmes, B. W. Drinkwater, Advanced reflector characterization with ultrasonic phased arrays in nde applications, IEEE Transactions on Ultrasonics, Ferroelectrics, and Frequency Control 54 (8) (2007) 1541–1550. doi:10.1109/TUFFC.2007.424.

[25] P. D. Wilcox, C. Holmes, B. W. Drinkwater, et al., Enhanced defect detection and characterisation by signal processing of ultrasonic array data, Proc. 9th ECNDT.

[26] INTERNATIONAL ATOMIC ENERGY AGENCY, Improvement of In-service Inspection in Nuclear Power Plants, INTERNATIONAL ATOMIC ENERGY AGENCY, Vienna, 2004, iAEA-TECDOC-1400.

[27] P. J. Shull, Nondestructive evaluation: theory, techniques, and applications, Vol. 1, Marcel Dekker, 2002.

[28] J. Zhang, P. Yu, T. Gang, Measurement of the ultrasonic scattering matrices of near-surface defects using ultrasonic arrays, Nondestructive Testing and Evaluation 31 (4) (2016) 303–318. doi:10.1080/10589759.2015.1093626.

[29] J. Goodman, Introduction to Fourier Optics, McGraw-Hill physical and quantum electronics series, W. H. Freeman, 2005.

[30] S. Rodriguez, P. Sahuguet, V. Gibiat, X. Jacob, Fast topological imaging, Ultrasonics 52 (8) (2012) 1010 – 1018. doi:10.1016/j.ultras.2012.08.002.

[31] M. V. Felice, A. Velichko, P. D. Wilcox, Accurate depth measurement of small surface-breaking cracks using an ultrasonic array post-processing technique, NDT & E International 68 (2014) 105–112. doi:10.1016/j.ndteint.2014.08.004.

[32] J. Temple, Time-of-flight inspection: theory, Nucl. Energy 22 (5) (1983) 335–348.

[33] S. Baby, T. Balasubramanian, R. J. Pardikar, M. Palaniappan, R. Subbaratnam, Time-of-flight diffraction (tofd) technique for accurate sizing of cracks embedded in sub-cladding, Insight - Non-Destructive Testing and Condition Monitoring 45 (9) (2003) 600–604. doi:10.1784/insi.45.9.600.52932.

[34] M. Moles, L. Robertson, T. Sinclair, Developments in time-of-flight diffraction (tofd), in: 18th World Conference on Nondestructive Testing, Vol. 1620, 2012.

[35] N. DING, S. Jin, D. Zhang, D. Kang, S. Zhang, M. Lei, L. Liu, L. Lin, Research on near surface dead zone reduction of tofd based on mode-converted theory 53 (2017) 120–124.

[36] D. Colton, R. Kress, Inverse Acoustic and Electromagnetic Scattering Theory, Applied Mathematical Sciences, Springer Berlin Heidelberg, 1997.

[37] A. Kirsch, N. Grinberg, The Factorization Method for Inverse Problems, Oxford Lecture Series in Mathe, OUP Oxford, 2008.

[38] A. Kirsch, An Introduction to the Mathematical Theory of Inverse Problems, Applied Mathematical Sciences, Springer New York, 1996.

[39] F. Simonetti, Multiple scattering: The key to unravel the subwavelength world from the far-field pattern of a scattered wave, Phys. Rev. E 73 (2006) 036619. doi:10.1103/PhysRevE.73.036619.

[40] F. Simonetti, Localization of pointlike scatterers in solids with subwavelength resolution, Applied Physics Letters 89 (9) (2006) 094105. doi:10.1063/1.2338888.

[41] A. Zinn, On an optimisation method for the full- and the limited-aperture problem in inverse acoustic scattering for a sound-soft obstacle, Inverse Problems 5 (2) (1989) 239.

[42] I. Graham, U. Langer, J. Melenk, M. Sini, Direct and Inverse Problems in Wave Propagation and Applications, Radon series on computational and applied mathematics, Walter de Gruyter GmbH, 2013.

[43] G. Kutyniok, V. Mehrmann, P. C. Petersen, Regularization and numerical solution of the inverse scattering problem using shearlet frames, Journal of Inverse and Ill-posed Problems 25 (3) (2017) 287–309.

[44] A. Lechleiter, K. S. Kazimierski, M. Karamehmedović, Tikhonov regularization in l_p applied to inverse medium scattering, Inverse Problems 29 (7) (2013) 075003.

[45] L. E. Kinsler, A. R. Frey, A. B. Coppens, J. V. Sanders, Fundamentals of acoustics, Vol. 1, Wiley, 2000.

[46] F. Cakoni, D. Colton, The linear sampling method for cracks, Inverse problems 19 (2) (2003) 279.

[47] J. Lohwater, O. Ladyzhenskaya, The Boundary Value Problems of Mathematical Physics, Applied Mathematical Sciences, Springer New York, 2013.

[48] B. Chen, F. Ma, Y. Guo, Time domain scattering and inverse scattering problems in a locally perturbed half-plane, Applicable Analysis 96 (8) (2017) 1303–1325. doi:10.1080/00036811.2016.1188288.

[49] A. Kirsch, The music-algorithm and the factorization method in inverse scattering theory for inhomogeneous media, Inverse Problems 18 (4) (2002) 1025.

[50] P. Huthwaite, F. Simonetti, M. J. S. Lowe, Ultrasonic quantitative imaging with limited view arrays, AIP Conference Proceedings 1511 (1) (2013) 714–721. doi:10.1063/1.4789116.

[51] N. Portzgen, D. Gisolf, G. Blacquiere, Inverse wave field extrapolation: a different ndi approach to imaging defects, IEEE Transactions on Ultrasonics, Ferroelectrics, and Frequency Control 54 (1) (2007) 118–127. doi:10.1109/TUFFC.2007.217.

[52] P. Huthwaite, F. Simonetti, High-resolution imaging without iteration: a fast and robust method for breast ultrasound tomography, The Journal of the Acoustical Society of America 130 (3) (2011) 1721–1734. doi:10.1121/1.3613936.

[53] F. Simonetti, M. Fleming, E. A. Marengo, Illustration of the role of multiple scattering in subwavelength imaging from far-field measurements, J. Opt. Soc. Am. A 25 (2) (2008) 292–303. doi:10.1364/JOSAA.25.000292.

[54] J. Lambert, A. Pédron, G. Gens, F. Bimbard, L. Lacassagne, E. Iakovleva, Analysis of multicore cpu and gpu toward parallelization of total focusing method ultrasound reconstruction, in: DASIP 2012 - Conference on Design and Architectures for Signal and Image Processing, Design and Architectures for Signal and Image Processing (DASIP), 2012 Conference on, Electronic Chips & Systems design Initiative, IEEE, Karlsruhe, Germany, 2012.

[55] M. V. Felice, A. Velichko, P. D. Wilcox, C. J. L. Lane, Depth measurement of small surface-breaking cracks using the half-skip total focusing method, AIP Conference Proceedings 1650 (1) (2015) 994–1000. doi:10.1063/1.4914706.

[56] M. LORENZ, L. V. D. WAL, A. BERKHOUT, Ultrasonic imaging with multisaft; nondestructive characterization of defects in steel components, Nondestructive Testing and Evaluation 6 (3) (1991) 149–177. doi:10.1080/10589759108953136.

[57] D. Colton, A. Kirsch, A simple method for solving inverse scattering problems in the resonance region, Inverse Problems 12 (4) (1996) 383.

[58] O. Bondarenko, A. Kirsch, The factorization method for inverse scattering by a penetrable anisotropic obstacle with conductive boundary condition, Inverse Problems 32 (10) (2016) 105011.

[59] J. Guo, G. Yan, J. Jin, J. Hu, The factorization method for cracks in inhomogeneous media, Applications of Mathematics 62 (5) (2017) 509–533. doi:10.21136/AM.2017.0194-16.

[60] K. M. M. Tant, A. J. Mulholland, A. Gachagan, Application of the factorisation method to limited aperture ultrasonic phased array data, Acta Acustica united with Acustica 103 (6) (2017) 954–966. doi:10.3813/AAA.919125.

[61] B. Gebauer, M. Hanke, C. Schneider, Sampling methods for low-frequency electromagnetic imaging, Inverse Problems 24 (1) (2008) 015007.

[62] A. Kirsch, Factorization of the far-field operator for the inhomogeneous medium case and an application in inverse scattering theory, Inverse Problems 15 (2) (1999) 413.

[63] T. Arens, N. Grinberg, A complete factorization method for scattering by periodic surfaces, Computing 75 (2) (2005) 111–132. doi:10.1007/s00607-004-0092-0.

[64] T. Hutt, F. Simonetti, Experimental observation of super-resolution imaging in highly attenuative materials, in: Proc. SPIE, Vol. 7968, 2011, pp. 79680X–79680X–8. doi:10.1117/12.878683.

[65] C. Fan, M. Caleap, M. Pan, B. W. Drinkwater, A comparison between ultrasonic array beamforming and super resolution imaging algorithms for non-destructive evaluation, Ultrasonics 54 (7) (2014) 1842 – 1850. doi:10.1016/j.ultras.2013.12.012.

[66] A. Kirsch, Characterization of the shape of a scattering obstacle using the spectral data of the far field operator, Inverse problems 14 (6) (1998) 1489.

[67] M. Fares, S. Gratton, P. L. Toint, Svd-tail: a new linear-sampling reconstruction method for inverse scattering problems, Inverse Problems 25 (9) (2009) 095013.

[68] C. Fioralba, C. David, On the mathematical basis of the linear sampling method, Georgian Mathematical Journal 10 (3) (2003) 411–425. doi:10.1515/GMJ.2003.411.

[69] Q. Chen, H. Haddar, A. Lechleiter, P. Monk, A sampling method for inverse scattering in the time domain, Inverse Problems 26 (8) (2010) 085001.

[70] V. Baronian, L. Bourgeois, A. Recoquillay, Imaging an acoustic waveguide from surface data in the time domain, Wave Motion 66 (2016) 68 – 87. doi:10.1016/j.wavemoti.2016.05.006.

[71] N. Khaji, S. D. Manshadi, Time domain linear sampling method for qualitative identification of buried cavities from elastodynamic over-determined boundary data, Computers & Structures 153 (Supplement C) (2015) 36 – 48. doi:10.1016/j.compstruc.2015.02.011.

[72] J. Collins, Failure of Materials in Mechanical Design: Analysis, Prediction, Prevention, Wiley-Interscience publication, Wiley, 1993.

[73] T. Cicero, P. Cawley, F. Simonetti, S. Rokhlin, Potential and limitations of a deconvolution approach for guided wave structural health monitoring, Structural Health Monitoring 8 (5) (2009) 381–395. doi:10.1177/1475921709102086.

[74] E. Iakovleva, S. Chatillon, P. Bredif, S. Mahaut, Multi-mode tfm imaging with artifacts filtering using civa ut forwards models, AIP Conference Proceedings 1581 (1) (2014) 72–79. doi:10.1063/1.4864804.

[75] T. Hutt, F. Simonetti, Reconstructing the shape of an object from its mirror image, Journal of Applied Physics 108 (6) (2010) 064909. doi:10.1063/1.3468669.

[76] M. Drozdz, Efficient Finite Element Modelling of Ultrasound Waves in Elastic Media, University of London, UK, 2008.

[77] P. Rajagopal, M. Drozdz, E. A. Skelton, M. J. Lowe, R. V. Craster, On the use of absorbing layers to simulate the propagation of elastic waves in unbounded isotropic media using commercially available finite element packages, NDT & E International 51 (2012) 30–40. doi:10.1016/j.ndteint.2012.04.001.

[78] P. Huthwaite, Eliminating incident subtraction in diffraction tomography, Proceedings of the Royal Society of London A: Mathematical, Physical and Engineering Sciences 472 (2195). doi:10.1098/rspa.2016.0707.

[79] F. Simonetti, L. Huang, From beamforming to diffraction tomography, Journal of Applied Physics 103 (10) (2008) 103110. doi:10.1063/1.2927433.

[80] C. Prada, M. Fink, Eigenmodes of the time reversal operator: A solution to selective focusing in multiple-target media, Wave Motion 20 (2) (1994) 151 – 163. doi:10.1016/0165-2125(94)90039-6.

[81] T. D. Hutt, F. Simonetti, Reconstructing the back of a defect from its mirror image, AIP Conference Proceedings 1211 (1) (2010) 742–749. doi:10.1063/1.3362469.

[82] M. Kemppainen, I. Virkkunen, J. Pitkänen, R. Paussu, H. Hänninen, Advanced flaw production method for in-service inspection qualification mock-ups, Nuclear Engineering and Design 224 (1) (2003) 105 – 117. doi:10.1016/S0029-5493(03)00078-5.

[83] I. Virkkunen, M. Kempainen, H. Ostermeyer, R. Paussu, T. Dunhill, Grown cracks for ndt development and qualification, Insight - Non-Destructive Testing and Condition Monitoring 51 (5) (2009) 271–278. doi:10.1784/insi.2009.51.5.271.

[84] S. Wilkinson, S. M. Duke, Comparative testing of radiographic testing, ultrasonic testing and phased array advanced ultrasonic testing non destructive testing techniques in accordance with the aws d1. 5 bridge welding code, Tech. Rep. BDK84-977-26, Department of Mechanical Engineering, University of South Florida (February 2014).

[85] V. Panchal, Pumps and valves: Ndt flaw detection, World Pumps 2014 (5) (2014) 34–40.

[86] N. Jain, Replacement of radiography by phased array ultrasonic testing drives global ultrasonic ndt equipment market: evolution of portable phased array ultrasonic testing equipment leads to large-scale uptake, Quality 53 (2) (2014) 10–12.

[87] J. Krautkrämer, Determination of the size of defects by the ultrasonic impulse echo method, British Journal of Applied Physics 10 (6) (1959) 240.

[88] J. Temple, Engineering applications of ultrasonic time-of-flight diffraction, no. 2, Research Studies PressLtd, 2001.

[89] S. C. Her, S. T. Lin, Non-destructive evaluation of depth of surface cracks using ultrasonic frequency analysis, Sensors (Basel) 14 (9) (2014) 17146–58. doi:10.3390/s140917146.

[90] S. C. Her, S. T. Lin, Sizing detection of a surface-breaking crack by ultrasonic technique, in: Advances in Mechanical Engineering, Vol. 52 of Applied Mechanics and Materials, Trans Tech Publications, 2011, pp. 865–868. doi:10.4028/www.scientific.net/AMM.52-54.865.

[91] M. Smith, ABAQUS/Standard User's Manual, Version 6.9, Simulia, Providence, RI, USA, 2009.

[92] F. Simonetti, L. Huang, N. Duric, O. Rama, Imaging beyond the born approximation: An experimental investigation with an ultrasonic ring array, Phys. Rev. E 76 (2007) 036601. doi:10.1103/PhysRevE.76.036601.

[93] Y. Humeida, P. D. Wilcox, M. D. Todd, B. W. Drinkwater, A probabilistic approach for the optimisation of ultrasonic array inspection techniques, NDT & E International 68 (2014) 43 – 52. doi:10.1016/j.ndteint.2014.07.007.

[94] J. Li, J. Zou, A direct sampling method for inverse scattering using far-field data, Inverse Problems and Imaging 7 (3) (2013) 757–775. doi:10.3934/ipi.2013.7.757.

[95] F. K. Gruber, E. A. Marengo, A. J. Devaney, Time-reversal imaging with multiple signal classification considering multiple scattering between the targets, The Journal of the Acoustical Society of America 115 (6) (2004) 3042–3047. doi:10.1121/1.1738451.

[96] S. Rodriguez, M. Deschamps, M. Castaings, E. Ducasse, Guided wave topological imaging of isotropic plates, Ultrasonics 54 (7) (2014) 1880 – 1890. doi:10.1016/j.ultras.2013.10.001.

[97] G. Bao, P. Li, Inverse medium scattering for the helmholtz equation at fixed frequency, Inverse Problems 21 (5) (2005) 1621.

[98] X. Chen, Y. Zhong, Music electromagnetic imaging with enhanced resolution for small inclusions, Inverse Problems 25 (1) (2009) 015008.

[99] K. Ito, B. Jin, J. Zou, A direct sampling method to an inverse medium scattering problem, Inverse Problems 28 (2) (2012) 025003.

[100] R. Griesmaier, Multi-frequency orthogonality sampling for inverse obstacle scattering problems, Inverse Problems 27 (8) (2011) 085005.

[101] R. Potthast, A study on orthogonality sampling, Inverse Problems 26 (7) (2010) 074015.

[102] Y. Guo, D. Hömberg, G. Hu, J. Li, H. Liu, A time domain sampling method for inverse acoustic scattering problems, Journal of Computational Physics 314 (2016) 647 – 660. doi:10.1016/j.jcp.2016.03.046.

[103] N. Dominguez, V. Gibiat, Non-destructive imaging using the time domain topological energy method, Ultrasonics 50 (3) (2010) 367 – 372. doi:10.1016/j.ultras.2009.08.014.

[104] N. Dominguez, V. Gibiat, Y. Esquerre, Time domain topological gradient and time reversal analogy: an inverse method for ultrasonic target detection, Wave Motion 42 (1) (2005) 31 – 52. doi:10.1016/j.wavemoti.2004.09.005.

[105] P. Sahuguet, A. Chouippe, V. Gibiat, Biological tissues imaging with time domain topological energy, Physics Procedia 3 (1) (2010) 677 – 683, international Congress on Ultrasonics, Santiago de Chile, January 2009. doi:10.1016/j.phpro.2010.01.085.

[106] J. Pommier, B. Samet, The topological asymptotic for the helmholtz equation with dirichlet condition on the boundary of an arbitrarily shaped hole, SIAM Journal on Control and Optimization 43 (3) (2004) 899–921. doi:10.1137/S036301290241616X.

[107] M. Bonnet, Topological sensitivity of energy cost functional for wave-based defect identification, Comptes Rendus MÃ©canique 338 (7) (2010) 377 – 389, inverse problems. doi:10.1016/j.crme.2010.07.016.

[108] M. Bonnet, Topological sensitivity for 3d elastodynamic and acoustic inverse scattering in the time domain, Computer Methods in Applied Mechanics and Engineering 195 (37) (2006) 5239 – 5254, john H. Argyris Memorial Issue. Part I. doi:10.1016/j.cma.2005.10.026.

[109] A. Malcolm, B. Guzina, On the topological sensitivity of transient acoustic fields, Wave Motion 45 (6) (2008) 821 – 834. doi:10.1016/j.wavemoti.2008.03.003.

[110] C. Y. Ahn, K. Jeon, Y.-K. Ma, W.-K. Park, A study on the topological derivative-based imaging of thin electromagnetic inhomogeneities in limited-aperture problems, Inverse Problems 30 (10) (2014) 105004.

[111] Y. Guo, P. Monk, D. Colton, The linear sampling method for sparse small aperture data, Applicable Analysis 95 (8) (2016) 1599–1615. doi:10.1080/00036811.2015.1065317.

[112] W. Choi, E. A. Skelton, F. Shi, M. J. S. Lowe, R. V. Craster, Rough surface reconstruction for ultrasonic nde simulation, AIP Conference Proceedings 1581 (1) (2014) 587–594. doi:10.1063/1.4864873.

[113] J. A. Ogilvy, Computer simulation of acoustic wave scattering from rough surfaces, Journal of Physics D: Applied Physics 21 (2) (1988) 260.

[114] J. Ogilvy, I. Culverwell, Elastic model for simulating ultrasonic inspection of smooth and rough defects, Ultrasonics 29 (6) (1991) 490 – 496. doi:10.1016/0041-624X(91)90080-R.

[115] J. A. Ogilvy, H. M. Merklinger, Theory of wave scattering from random rough surfaces, The Journal of the Acoustical Society of America 90 (6) (1991) 3382–3382. doi:10.1121/1.401410.

[116] F. Shi, W. Choi, M. J. S. Lowe, E. A. Skelton, R. V. Craster, The validity of kirchhoff theory for scattering of elastic waves from rough surfaces, Proceedings of the Royal Society of London A: Mathematical, Physical and Engineering Sciences 471 (2178). doi:10.1098/rspa.2014.0977.

[117] J. A. Greenwood, A unified theory of surface roughness, Proceedings of the Royal Society of London A: Mathematical, Physical and Engineering Sciences 393 (1804) (1984) 133–157. doi:10.1098/rspa.1984.0050.

[118] M. S. Longuet-Higgins, Statistical properties of an isotropic random surface, Philosophical Transactions of the Royal Society of London A: Mathematical, Physical and Engineering Sciences 250 (975) (1957) 157–174. doi:10.1098/rsta.1957.0018.

[119] J. Ogilvy, Model for the ultrasonic inspection of rough defects, Ultrasonics 27 (2) (1989) 69 – 79. doi:10.1016/0041-624X(89)90016-4.

[120] F. Shi, M. Lowe, X. Xi, R. Craster, Diffuse scattered field of elastic waves from randomly rough surfaces using an analytical kirchhoff theory, Journal of the Mechanics and Physics of Solids 92 (2016) 260 – 277. doi:10.1016/j.jmps.2016.04.003.

[121] J. Zhang, B. W. Drinkwater, P. D. Wilcox, A. J. Hunter, Defect detection using ultrasonic arrays: The multi-mode total focusing method, NDT & E International 43 (2) (2010) 123 – 133. doi:10.1016/j.ndteint.2009.10.001.

[122] F. Shi, M. Lowe, R. Craster, Recovery of correlation function of internal random rough surfaces from diffusely scattered elastic waves, Journal of the Mechanics and Physics of Solids 99 (2017) 483 – 494. doi:10.1016/j.jmps.2016.11.003.

[123] M. Bièth, J. Monjaret, NDE in Relation to Structural Integrity for Nuclear and Pressurised Components: Proceedings of the First International Conference, First international conference on NDE in relation to structural integrity for nuclear and

pressurised components [20-22 October 1998, Amsterdam, The Netherlands], Elsevier Science, 1999.

List of Publications

[P1] C. Zhang, P. Huthwaite and M. Lowe. The application of the Factorization Method to the subsurface imaging of surface-breaking cracks, in *IEEE Transactions on Ultrasonics, Ferroelectrics, and Frequency Control* 65(3) (2018) 497-512.

[P2] C. Zhang, P. Huthwaite and M. Lowe. Eliminating backwall effects in the phased array imaging of near backwall defects, in *The Journal of the Acoustical Society of America* 144(2) (2018) 1075-1088.

[P3] C. Zhang, P. Huthwaite and M. Lowe. Novel imaging algorithms for non-destructive evaluation using FMC data, ready for submission.